NANOSECOND PULSED INFRARED LASER INDUCED CRYSTALLIZATION OF AMORPHOUS SILICON FILMS FOR POTENTIAL PHOTOVOLTAIC APPLICATIONS

A THESIS SUBMITTED TO
THE GRADUATE SCHOOL OF NATURAL AND APPLIED SCIENCES
OF
MIDDLE EAST TECHNICAL UNIVERSITY

BY

KAMIL ÇINAR

IN PARTIAL FULFILLMENT OF THE REQUIREMENTS
FOR
THE DEGREE OF DOCTOR OF PHILOSOPHY
IN
PHYSICS

SEPTEMBER 2018

Approval of the thesis:

NANOSECOND PULSED INFRARED LASER INDUCED CRYSTALLIZATION OF AMORPHOUS SILICON FILMS FOR POTENTIAL PHOTOVOLTAIC APPLICATIONS

submitted by **KAMIL ÇINAR** in partial fulfillment of the requirements for the degree of **Doctor of Philosophy in Physics Department, Middle East Technical University** by,

Prof. Dr. Halil Kalıpçılar _____
Dean, Graduate School of **Natural and Applied Sciences**

Prof. Dr. Altuğ Özpineci _____
Head of Department, **Physics**

Assoc. Prof. Dr. Alpan Bek _____
Supervisor, **Physics Dept., METU**

Examining Committee Members:

Assoc. Prof. Dr. Akın Bacıoğlu
Physics Engineering Dept., Hacettepe University _____

Assoc. Prof. Dr. Alpan Bek
Physics Dept., METU _____

Prof. Dr. Barış Akaoğlu
Physics Engineering Dept., Ankara University _____

Prof. Dr. Raşit Turan
Physics Dept., METU _____

Assist. Prof. Dr. Ihor Pavlov
Physics Dept., METU _____

Date: _____

I hereby declare that all information in this document has been obtained and presented in accordance with academic rules and ethical conduct. I also declare that, as required by these rules and conduct, I have fully cited and referenced all material and results that are not original to this work.

Name, Last Name: KAMIL ÇINAR

Signature :

ABSTRACT

NANOSECOND PULSED INFRARED LASER INDUCED CRYSTALLIZATION OF AMORPHOUS SILICON FILMS FOR POTENTIAL PHOTOVOLTAIC APPLICATIONS

Çınar, Kamil
Ph.D., Department of Physics
Supervisor : Assoc. Prof. Dr. Alpan Bek

September 2018, 129 pages

Laser processing applied to thin film silicon is a practical tool for fabrication of thin film transistors and solar cells. Application of laser processing technologies to silicon based photovoltaics has been on the rise. Two examples out of plenty are: crystallization of amorphous Si (a-Si) thin films to produce polycrystalline Si (poly-Si) thin films; and quality improvement of poly-Si structures on the silicon wafer surface by laser annealing. Parameters for optimal crystalline silicon fabrication depend on fluence of the laser irradiation and physical conditions of the substrate where the silicon crystallization occurs. These various parameters can change the physical features of the grown poly-Si domains such as size, shape, thickness, orientation, etc. The determination and optimization of these parameters are of importance in fabrication of efficient silicon thin film solar cells. Previous works show that efficiency of the laser crystallized poly-Si solar cells exhibit enhancement of their material qualities. In this thesis, characterization of the laser induced crystallization and optimization of the nanosecond pulsed infrared laser parameters are investigated. Besides, a laser crystallization system is developed for processing a-Si thin films into poly-Si thin films for the purpose of fabrication of crystalline thin film silicon solar cells. Crystalline silicon layers with thicknesses ranging between several hundred nanometers and a micrometer are fabricated by means of the nanosecond pulsed infrared laser. The laser crystallization is performed in air at room temperature and no heating is applied

to substrates. Grain sizes of up to several millimeters are found on the surface of the crystallized silicon layers. The produced crystalline silicon films are employed in fabrication of heterojunction p-n diodes and solar cells.

Keywords: Laser Crystallization, Liquid-Phase Crystallization, Amorphous Silicon, Thin Film, Intermediate Dielectric Layer, Raman Spectroscopy, Electron Back Scatter Diffraction

ÖZ

POTANSİYEL FOTOVOLTAİK UYGULAMALAR İÇİN AMORF SİLİSYUM FİLMLERİN NANOSANİYE KIZILÖTESİ ATIMLI LAZER YARDIMIYLA KRİSTALİZASYONU

Çınar, Kamil
Doktora, Fizik Bölümü
Tez Yöneticisi : Doç. Dr. Alpan Bek

Eylül 2018 , 129 sayfa

İnce film silisyuma laser işlemi uygulanması ince film transistörler ve güneş gözeleri için kullanışlı bir araçtır. Silisyum esaslı fotovoltaik hüçreleri lazer teknolojileri ile işleme yükseliştedir. Polikristal silisyum (poly-Si) ince filmleri üretmek için amorf silisyum (a-Si) ince filmlerin kristalizasyonu; ve silisyum yongaların yüzelerindeki poly-Si yapıların kalitelerini lazerle tavlama ile artırılması iki yaygın örnektir. Optimal krital silisyum üretimi parametreleri, lazerle aydınlatma akışına ve üzerinde silisyum kristallenmesinin olduğu alttaşın fiziksel koşullarına bağlıdır. Bu çeşitli parametreler büyütülen poly-Si alanlarının büyüklük, şekil, kalınlıklarını ve yönelimleri gibi, fiziksel özelliklerini değiştirebilirler. Bu parametrelerin belirlenmesi ve optimizasyonu, verimli silisyum ince film güneş gözeleri üretiminde önem arz eder. Önceki çalışmalarda lazer kristalize poly-Si güneş gözelerinin verimliliklerinde artış, malzeme kalitesinde iyileşme gösterilmiştir. Bu tez çalışmada nanosaniye atımlı kızılötesi lazer yardımıyla kristalizasyonun karakterizasyonu ve lazer ışımasının parametrelerinin optimizasyonu araştırılmıştır. Bunun yanında, ince film kristal silisyum güneş gözesi üretimi amacıyla a-Si ince filmleri poly-Si ince filmlere işlemekte kullanılacak laser kristalizasyon sistemi geliştirilmiştir. Kalınlıkları birkaç yüz nanometre ve mikrometre mertebelerinde olan kristallenmiş silisyum tabakalar, nanosaniye darbeli kızılötesi lazer yardımıyla geliştirilmiştir. Lazer kristalizasyonu, oda sıcaklığında havada gerçekleştirilmiştir ve hiçbir alttaş ısıtması uygulanmamıştır. Tanecik boyutları,

kristalize silisyum tabakaların yüzeyinde birkaç milimetreye kadar büyüdüğü bulunmuştur. Üretilen kristallendirilmiş ince film silisyum filmler, heteroeklemli p-n diyotlar ve güneş gözeleri geliştirmekte kullanılmıştır.

Anahtar Kelimeler: Lazer Kristalizasyon, Sıvı-Faz Kristalizasyonu, Amorf Silisyum, İnce Film, Ara Dielektrik Katman, Raman Spektroskopisi, Elektron Geri Saçılım Kırınımı

İnsan-ı Kâmil olan babam Cemil Çınar'a bu tezi adıyorum. Onun anısıyla ve gösterdiği bilgelikle yoluma devam ediyorum.

I dedicate this thesis to my father, Cemil Çınar, who is a perfect human being. I keep on my journey by his memory and great wisdom.

ACKNOWLEDGMENTS

This work was a long running and hard study for a single person. There were a lot of names contributing to this study.

Firstly, I want to thank to my mother, Naime Çınar and my wife, Katif Çınar for their great support while I was working on this research. Whenever I lost my enthusiasm and motivation, they provided precious psychological support for me. I present my deep love and loyalty to them.

Beside of my mother and wife, Cemre Kuşoğlu , Merve Demirtaş and Gökhan Alkaç helped me and gave precious advices while I was writing this dissertation. They showed me their sincere friendship.

During this research several colleagues of mine helped me with their knowledge and talent. In the production of the thin silicon films and fabrication of the solar cells they performed great effort. So I want to thank to these friends, namely Mehmet Karaman, Salar H. Sedani, Ergi Dönerçark, Nardin Avishan, A. Ege Aytaç and İ. Murat Öztürk. For the characterization of the samples by electron back scatter diffraction method Sedat Canlı spent lots of his time and gave instructive tips. The improvements on the pulsed laser system and the sample stage were done by the help of Emre M. Yağcı. Emre did give his urgent support to me whenever I needed. So I want to thank these guys separately.

I want to thank the Center for Solar Energy Research and Applications (GÜNAM) and FiberLAST Inc. for letting me use their facilities and equipment. And also I thank to Raşit Turan and Barış Akaoğlu for their contributions during the thesis monitoring meetings at end of the every semester.

Finally, I am deeply thankful to Alpan Bek. He accepted me as a PhD student and guide me on this subject. Whenever I came to a dead end, he motivated and encouraged me and shared his knowledge on the way of this study. Up to now, he showed me the way and from now on I hope to become his close colleague on this field of interest.

This thesis work is supported by TÜBİTAK grant nr. 115M061.

TABLE OF CONTENTS

ABSTRACT v

ÖZ vii

ACKNOWLEDGMENTS x

TABLE OF CONTENTS xi

LIST OF TABLES xiv

LIST OF FIGURES xv

CHAPTERS

1 INTRODUCTION 1

2 THEORETICAL BACKGROUND 7

2.1 Theory of laser crystallization of amorphous silicon 7

2.1.1 Interface dynamics of crystal growth 9

2.1.2 Laser induced phase transformation 12

2.2 Line focus scanning optics 18

2.3 Analysis of crystallinity 20

3 EFFECTS OF INTERMEDIATE DIELECTRIC LAYERS ON LASER CRYSTALLIZATION OF AMORPHOUS SILICON FILMS 23

3.1 Overview of laser marking systems 23

3.2 Preliminary studies over laser crystallization 24

3.2.1 Determination of crystallization and damage thresholds with spot focus scan 24

3.2.2 Raman spectroscopy and EBSD analyses 28

3.2.3 Macro structural trials 31

3.3 Laser crystallization of amorphous silicon films on various intermediate dielectric layers over glass substrate 35

3.3.1 Preparation of thin films 35

3.3.2 Laser crystallization of specimens 37

3.3.3 Raman analyses of laser crystallized a-Si films . . 38

3.3.4 SEM images of laser crystallized a-Si films 41

3.3.5 EBSD analyses of laser crystallized a-Si films . . . 42

3.3.6 Secondary ion mass spectroscopy analyses of laser crystallized a-Si films 44

3.3.7 Transmission and reflection analyses of laser crystallized a-Si films 47

4 INFLUENCES OF SI FILM THICKNESS AND OVERLAP OF LASER PULSES ON LASER CRYSTALLIZATION 51

4.1 Improvements of line focus scan 51

4.2 Effects of Si film thickness on laser crystallization and fluence correlation 64

4.3 Influence of overlapping laser pulses on laser crystallized Si surface 68

5 DEFECT ANALYSES 89

6 DEVICE DESIGNS ON LASER CRYSTALLIZED THIN SILICON FILMS 95

6.1 Homojunction device trials 95

6.2 Heterojunction device trials 98

7 CONCLUSIONS AND DISCUSSIONS 109

REFERENCES 115

CURRICULUM VITAE 123

LIST OF TABLES

TABLES

Table 1.1 Types of laser typically used to crystallize and anneal thin Si films . 2

Table 3.1 EO Technics SuperMarker GF311 24

Table 3.2 Flast-NanoMARK 50W 24

Table 3.3 Scan parameters of the laser marking system 25

Table 3.4 Optical parameters of the laser marking system 25

Table 3.5 Laser scan parameters for Figure 3.13 32

Table 3.6 Thermal conductivities of IDLs 39

Table 4.1 Laser parameters of the line focus scan 54

Table 4.2 Laser average power and effective fluence values for laser crystallized lines of 950 nm a-Si Film 57

Table 4.3 Laser scan parameters of overlapping and non-overlapping pulses in Figure 4.23 69

Table 4.4 Laser scan parameters of Sample 2 in Figure 4.31 75

Table 4.5 Optimized parameters of LC for $\sim 1\mu$m i-a-Si Films 88

Table 6.1 Measurements values of the device properties 99

LIST OF FIGURES

FIGURES

Figure 2.1 Energy relations 11

Figure 2.2 Line focus optics 19

Figure 2.3 Raman Spectra of Silicon 21

Figure 3.1 Laser marking systems 23

Figure 3.2 Laser crystallized lines over i-a-Si thin films of 650 nm 25

Figure 3.3 Microscope image of Line 1 26

Figure 3.4 Microscope image of Line 4 27

Figure 3.5 Damages appeared at the center of the laser crystallized region, micro crystalline silicon (μc-Si). 27

Figure 3.6 Damaged regions started to melt down and the uniform crystalline regions circumscribed them with increasing radii. 28

Figure 3.7 The damaged structures on Si films without pulse overlap 28

Figure 3.8 Si Raman spectra of Line 1 and Line 4 29

Figure 3.9 Colored SEM image of Line 1 30

Figure 3.10 Colored SEM image of Line 4 30

Figure 3.11 EBSD images of a) Line 1 and b) Line 4 31

Figure 3.12 a) Demonstration of pulse overlap and b) Overlap of successive circular patterns. c) Produced macro structure with a diameter of 3 mm. 32

Figure 3.13 Macroscopic structures processed by spot focus 32

Figure 3.14 Microscope views of crystallized circles C1, C2, C3 and C4. . . . 33

Figure 3.15 Si Raman spectra acquired from crystallized circular patterns . . . 34

Figure 3.16 Damaged crystallized circular patterns via polishing 34

Figure 3.17 Designed structures in order to investigate the effects of intermediate layer types on laser crystallization of a-Si thin films 35

Figure 3.18 LC processed samples with different IDLs; a) No Buffer Layer, b) IDL: SiN_x , c) IDL: SiO_2 , d) IDL: TiO_2, e) IDL: ZnO. The LC processed regions have a diameter of 12 mm. 37

Figure 3.19 Si Raman spectra of the IDL samples 39

Figure 3.20 Quantitative comparison of Raman spectra 40

Figure 3.21 SEM images of laser crystallized samples with a) no buffer layer; b) the thickness of 30 nm SiN_x ; c) the thickness of 30 nm SiO_2 ; d) the thickness of 30 nm TiO_2 ; e) the thickness of 35 nm ZnO. 41

Figure 3.22 EBSD images of LC specimens with a) no buffer layer; b) the thickness of 30 nm SiN_x ; c) the thickness of 30 nm SiO_2 ; d) the thickness of 30 nm TiO_2 ; e) the thickness of 35 nm ZnO; f) color code of crystal orientations 42

Figure 3.23 SIMS analysis of 650 nm LC Si layer without an IDL 44

Figure 3.24 SIMS analysis of 650 nm LC Si layer with 30 nm of SiN_x 45

Figure 3.25 SIMS analysis of 650 nm LC Si layer with 30 nm of SiO_2 45

Figure 3.26 SIMS analysis of 650 nm LC Si layer with 30 nm of TiO_2 46

Figure 3.27 SIMS analysis of 550 nm LC Si layer with 35 nm of ZnO 46

Figure 3.28 Scheme of transmission-reflection spectrum measurement 47

Figure 3.29 Total transmission spectra 48

Figure 3.30 Total reflection spectra 48

Figure 3.31 Diffuse transmission spectra 49

Figure 3.32 Diffuse reflection spectra 49

Figure 3.33 Absorption spectra 50

Figure 4.1 Line focus system design 51

Figure 4.2 Photograph image of the line focus scanning system 52

Figure 4.3 Virtualization of a line focus scan 53

Figure 4.4 Line focus scans on a-Si films with a thickness of 1 μm 53

Figure 4.5 Raman spectra of i-a-Si, L1 and Ref. c-Si 54

Figure 4.6 Raman spectra of the line focus Scan trails 55

Figure 4.7 Si Raman peak analysis of the line focus scans 55

Figure 4.8 Optical image of the line scans 56

Figure 4.9 Diagram of line shifting; W: Line width and LO: Overlapped region of the lines 56

Figure 4.10 Laser crystallized lines of 950 nm a-Si Film. The numerated lines are scanned via the line focus optics. 57

Figure 4.11 Analyses of Raman spectra 57

Figure 4.12 Optical microscope images of Line 1 - 6 58

Figure 4.13 a) SEM and b) EBSD images of Line 1 59

Figure 4.14 a) SEM and b) EBSD images of Line 2 59

Figure 4.15 a) SEM and b) EBSD images of Line 3 60

Figure 4.16 a) SEM and b) EBSD images of Line 4 61

Figure 4.17 a) SEM and b) EBSD images of Line 5 62

Figure 4.18 a) SEM and b) EBSD images of Line 6 63

Figure 4.19 Temperature dependent specific heat capacity of Silicon [72]. . . . 64

Figure 4.20 Extinct energy percent through the a-Si layer 66

Figure 4.21 Minimum and maximum fluences needed to rise the temperature of a-Si layers for melting and boiling respectively and the experimentally determined fluence needed in order to crystalline the layers of a-Si with various thicknesses. 67

Figure 4.22 Raman signal analysis for various thicknesses of LC a-Si layer . . 67

Figure 4.23 Consecutive pulses at the damage fluence of threshold a) without overlap and b) with overlap. 68

Figure 4.24 Analyses of Raman spectra of 800 nm, 950 nm and 1050 nm laser processed i-a-Si layers. 70

Figure 4.25 Sample 1, which has 950 nm i-a-Si film, is scanned by laser with the different overlap ratios of pulses. 71

Figure 4.26 AFM image of LC processed 950 nm i-a-Si of Line 0 (Q-Factor: 0%) 71

Figure 4.27 AFM images of LC processed 950 nm i-a-Si of Line 1-10 of Sample 1 72

Figure 4.28 Boundary is formed by two consecutive overlapping pulses (Q-factor: 30%). 73

Figure 4.29 S_q parameters, with respect to Q-Factor for the LC processed i-a-Si of 950 nm. 74

Figure 4.30 Raman analysis of Sample 1, LC i-a-Si of 950 nm. 75

Figure 4.31 Sample 2 of LC processed 1050 nm i-a-Si 75

Figure 4.32 Optical microscope image of Line 1 (Q-Factor: 99.9%) with phase contrast 76

Figure 4.33 Optical microscope image of Line 2 (Q-Factor: 99.8%) with phase contrast 76

Figure 4.34 Optical microscope image of Line 3 (Q-Factor: 99.7%) with phase contrast 77

Figure 4.35 Optical microscope image of Line 4 (Q-Factor: 99.6%) with phase contrast 78

Figure 4.36 Optical microscope image of Line 5 (Q-Factor: 99.4%) with phase contrast 79

Figure 4.37 Optical microscope image of Line 6 (Q-Factor: 99.3%) with phase contrast 80

Figure 4.38 Optical microscope image of Line 7 (Q-Factor: 99.2%) with phase contrast 81

Figure 4.39 Optical microscope image of Line 8 (Q-Factor: 99.9%) with phase contrast 82

Figure 4.40 Raman analysis of Sample 2 with respect to the scan speeds, which correspond to the numbers of lines. 82

Figure 4.41 Sample 2 of LC 1050 nm i-a-Si Film: a) EBSD image of Line 1, b) EBSD image of Line 2. 83

Figure 4.42 Sample 2 of LC 1050 nm i-a-Si Film: a) EBSD image of Line 3, b) EBSD image of Line 4. 83

Figure 4.43 Sample 2 of LC 1050 nm i-a-Si Film: a) EBSD image of Line 5, b) EBSD image of Line 6, c) EBSD image of Line 7, and d) Color map of c-Si in order to define the orientations of crystalline domains. 84

Figure 4.44 EBSD image analysis of Line 8 (Q-Factor: 99.9%), as an example of measuring the lengths of crystalline domains. 85

Figure 4.45 Histograms of Line 1, 2, 3, and 4: Counts vs. Length of Domain. . 85

Figure 4.46 AFM images of Line 1-6 86

Figure 4.47 S_q values of Line 1-7 with their corresponding scan speeds. 86

Figure 4.48 3D view of AFM image of Line 7 with its corresponding the inset microscopy image 87

Figure 4.49 Semi-log graph of sheet resistance [$\Omega/\square$] for Line 1 - 7 of Sample 2 88

Figure 5.1 Microscope image of LC process 950 nm i-a-Si films after a crater is formed during the measurement of the TOF-SIMS 90

Figure 5.2 3D view of the AFM image over the cracked region and the inset microscope image 91

Figure 5.3 Removed/damaged Si layers over the cracked glass surface 91

Figure 5.4 Line focus scan of 800 nm i-a-Si layer with various parameters . . 92

Figure 5.5 Laser crystallization of PECVD deposited samples before/during/after the laser annealing 92

Figure 5.6 Microscope images of the sample after the annealing by furnace . 93

Figure 5.7 Color of LC processed PECVD deposited a-Si layer 94

Figure 6.1 Homojunction Device Design 96

Figure 6.2 SEM images of LC processed 950 nm thick films (the inset images are actual photos) 96

Figure 6.3 Raman spectra of the laser processed samples of 950 nm i-a-Si coated with spin-on dopants 97

Figure 6.4 SEM images of the laser processed samples of 1250 nm i-a-Si and 80 nm SiN_x (the inset images are actual photos) 98

Figure 6.5 6 different heterojunction device structures 100

Figure 6.6 Damaged structures after LC process; a) Sample V and b) Sample VI 101

Figure 6.7 Raman spectra of the constructed devices 101

Figure 6.8 Heterojunction device images a) e-Beam deposited without SiN_x , b) e-Beam deposited with SiN_x , c) PECVD deposited without SiN_x , d) PECVD deposited with N-c-Si Wafer 101

Figure 6.9 I-V curve of the sample, deposited by e-Beam method without SiN_x 102

Figure 6.10 I-V curve of the sample, prepared by PECVD method on N-c-Si wafer without/with illuminating (labelled as Dark/Light) the sample . . . 102

Figure 6.11 Solar simulator measurement of the sample, deposited by e-Beam method without SiN_x 103

Figure 6.12 Heterojunction device design with 1 μm of P^+- P layer 103

Figure 6.13 Heterojunction device design with 30 nm, 100 nm and 300 nm of Al layers 104

Figure 6.14 The constructed devices: a) Device with 1 μm of P^+- P layer; b) Device with 30 nm Al layer; c) Device with 100 nm Al layer; d) Device with 300 nm Al layer; 104

Figure 6.15 The IV curves of the device, with 1 μm of P^+- P layer 105

Figure 6.16 The IV curves of the device, with 30 nm Al layer 106

Figure 6.17 The IV curves of the device, with 100 nm Al layer 106

Figure 6.18 The IV curves of the device, with 300 nm Al layer 107

Figure 7.1 Cylindrical Lens vs. Powell Lens [74] 112

CHAPTER 1

INTRODUCTION

Laser processing has been a practical tool in order to fabricate crystalline thin films in applications of solar cells and thin film transistors (TFTs). In order to explore which methods of applying laser crystallization and what kinds of lasers should be used for this sake is a great deal. There are a great variety of lasers which can be employed for this purpose. Which wavelength and how the irradiation should be utilized are the questions that should be answered. The use of lasers allows to fabricate device grade structures easily and cost effectively. In this thesis work nanosecond pulsed infrared (IR) lasers are employed and their ability of crystallization of amorphous silicon (a-Si) on glass substrates is studied. The irradiation parameters are optimized for improved crystallinity quality using specific intermediate dielectric layers (IDLs), line focusing and pulse overlap.

Studies on laser crystallization (LC) and laser annealing started to rise in late 1970s. Utilization of lasers enabled to direct energy over areas of interest by its ability to control delivery of heat and location on specimens in a unique way. In order to fabricate thin single crystal semiconductors such as silicon (Si), germanium (Ge) and their alloys on amorphous insulating substrates, controllable geometry of laser spots deliver the benefit of avoiding random nucleation [1].

Fabrication of poly-crystalline silicon (pc-Si) thin films via *in situ* annealing of a-Si films on various carrier substrates became popular for electronics industry, especially for Si based TFTs and solar cell applications [2, 3]. Particularly, cost effective glass substrates are the most prevalent substrate materials for crystallization of a-Si. The traditional way of producing pc-Si thin film is the solid phase crystallization (SPC) method which is performed by high temperature baking. However, SPC method has

Table 1.1: Types of laser typically used to crystallize and anneal thin Si films

Lasers	Type	Wavelengths (nm)
Nd: YAG	Solid	1064
Nd: TLF	Solid	1064
Diode Laser	Solid	808, 940
Ruby	Solid	694
Nd: YAG	Solid	532
Ar^+	Gas	330-522
XeCl	Gas	308
KrF	Gas	248
ArF	Gas	193

drawbacks of long annealing duration (~ 24 h) and small attained grain size ($\sim 1-3$ μm) which results in high defect concentrations [4,5]. Rapid thermal annealing (RTA) is also an SPC method in which typically a halogen lamp is used to heat and crystallize a-Si thin films over glass substrates [6]. The RTA process starts with a steep heating ramp (~ 200 °C/s) which is followed by a steady temperature phase of ~ 900 °C and finalizes with a cooling down (~ 80 °C/s) phase all maintained under an appropriate gas ambient [6]. These process stages causes deformations on the glass substrates and that limits the choice of substrate material [6].

Laser crystallization and annealing have advantage over these conventional annealing methods by its ability to control rapid heating and cooling of thin layers via controlling the laser pulse duration time and the overlap ratio of the successive laser pulses in addition to wide choices of operation wavelengths which can be selected with regards to the desired absorption depth of the particular film material [1]. By 2018, there exists a large selection of lasers which can be employed for this purpose (see Table 1.1).

Besides the wavelengths of the employed lasers, the state of a material subjected to laser irradiation is also important in coupling of light to the material. For example, a single-crystal silicon and hydrogenated amorphous silicons (a-Si:H) are compared with respect to their optical absorption lengths which are 3.3 μm and 0.4 μm at a wavelength of 632 nm respectively [1].

Aluminum-induced crystallization (AIC) of a-Si is another method that is processed

at relatively lower temperatures (< 500 °C) providing large grain size (> 10 μm) which makes AIC pc-Si films suitable as a seed layer for LC [7]. In addition, the use of different intermediate dielectric layers (IDLs; such as SiN_x, SiO_2, ZnO, TiO_2) can change the pc-Si film properties such as grain orientation and grain size [7, 8]. The subsequent epitaxial growth on AIC seed layers was studied extensively [9, 10]. However, although resulting in large grains, the high density of intra-grain defects makes this method inconvenient for solar cell applications [11, 12]. Liquid phase crystallization (LPC) is an alternative way of producing pc-Si films. A deposited thin a-Si layer on glass is locally molten by a focused energy source such that rapid off-switching of the energy inflow results in a quick solidification after which a-Si ends up as pc-Si. LPC by electron beam (e-beam) crystallization of a-Si is used to produce pc-Si layers up to 10 μm thickness on glass substrates [13–16]. Furthermore, LPC was improved by using line-shaped e-beam source [16]. In previous studies, it was shown that LPC method resulted in more efficient thin film pc-Si solar cells [14–18].

Crystalline domain size in the range of millimeters in width and up to centimeters in length on glass substrates was achieved especially by using a continuous wave (CW) laser (see Table 1.1) in LPC [14,19,20]. Moreover, the defects and deformations of the substrates could be avoided or lowered and the choice of substrates and IDLs (buffer layers) could be diversified [13, 17, 21–24]. Not only let the LC process method diversify the choice of the IDLs but also it has offered crystallization of amorphous materials on insulating substrates like sapphire, silicon nitrite, quartz, and glass [1].

The LC method for crystallization of a-Si thin films was studied with CW diode lasers with a line focus that was perpendicular to scan directions [24,25]. Most of past work was performed by using CW IR lasers. Moreover, a-Si films on glass substrates were kept at elevated temperatures during the laser annealing process, because the a-Si layers exhibit low absorption of the infrared irradiation in comparison to the visible in room temperature (RT) [6, 24]. The samples were kept at temperatures in the range of 400 °C-700 °C in order to increase the light absorption [6, 13–15, 17, 26]. Besides the absorption enhancement, the thermal expansion coefficient of the glass substrates approaches to that of crystalline silicon (c-Si) at around 600 °C [20]. Additionally, the elevated substrate temperature can be used to avoid crack formation through crystalline domains during the LC process and it can reduce thermally induced stress on

the pc-Si layers [6, 17, 20, 24].

Importance of an IDL between the glass substrate and the pc-Si thin film is owing to its features such as blocking diffusion of contaminants from the substrate into the pc-Si film during thermal processes and preventing lattice or average inter-atomic distance mismatch between the substrate and the film [7, 16, 17, 21]. For LPC, c-Si/SiO_2 nano-crystalline interface with undefined stoichiometry was observed [27]. LPC process by e-beam with an IDL of SiO_2 was found to be suitable between the glass substrate and the silicon thin film which improved the homogeneity of the thickness of the crystallized absorber [27]. Additionally, SiN_x can be an alternative next to SiO_2 as an IDL. The amount of Si content in SiN_x layers can change the crystallization properties of the a-Si films. Moreover, the quality of pc-Si films can be improved by a SiN_x IDL. For example, such a layer can be deposited by decreasing the NH_4/SiH_4 ratio, i.e., increasing silicon in the content of the SiN_x IDL [7] in a plasma enhanced chemical vapor deposition (PECVD) system. It was also shown that SiN_x IDLs with higher Si content helped to improve the crystallinity of Si thin films more than that of the samples with IDLs of Al:ZnO (AZO) [7]. In the study of Dore et al. [14], SiC_x was shown to act as a better wetting layer than SiO_2 or SiN_x. Besides that, no correlation between laser fluence and crystallinity of the pc-Si layer was found [14]. It was shown that SiO_2 IDL provided larger crystal grains of Si induced by the laser irradiation than that of SiN_x since the thermal conductivity of SiO_2 is smaller than that of the glass substrate [28, 29]. Thus the rate of heat flow decreases through the Si film; on the contrary, the SiN_x layer has a larger thermal conductivity than SiO_2, which makes the Si film lose the heat during the laser induced LPC [28, 29].

In this thesis dissertation, the LC process of a-Si layers are examined. During the research, nanosecond pulsed lasers are used in order to crystallize a-Si layers with different ranges of thicknesses on glass substrates. The lasers are at the wavelength of 1064 nm with a pulse duration of 200 ns. The lasers are commercially available lasers, which are not especially designed for this LC process. On the contrary to the previous studies, the preheating of the substrates are not performed during the LC processes, and the entire process is performed at RT. One of the important goals of this research is to fabricate pc-Si thin films at as close temperatures as possible to the ambient for effective cost reduction. Herein, the main motivation is to achieve photo-

responsive crystalline thin Si films in order to fabricate ultra thin crystal silicon solar cells. The dissertation consists of 5 main chapters in addition to the introduction.

Chapter 2 provides a theoretical background of the LC process. In this chapter, physical properties of materials which are employed in LC are discussed. The physical mechanism behind the liquid phase transition and the heat transfer during the laser exposure are explained in detail in this chapter. How the overlap of successive laser pulses influence LC process and improve the crystallized regions are also studied theoretically. Since the LC processed structures are examined quantitatively in this dissertation, Raman spectroscopy and electron back scattered diffraction (EBSD) methods are used extensively throughout the research in order to quantify the crystallinity. Brief explanations of these analysis techniques are also included. Accumulated stress over the crystallized structures is analyzed because the Raman and EBSD methods play crucial role to find out the stress factors and orientations of the crystal domains after the LC processes.

Chapter 3 - 6 provide details on the experimental part of the dissertation which is performed in Nanooptics Research Laboratory of Middle East Technical University. The experiments are discussed chronologically in order to provide explanations for readers to perceive the improvements step by step. In these chapters, some background of optics and stress analysis methods are also discussed in order to clarify and ease the understanding of the results.

Chapter 3 includes effects of intermediate dielectric layers on LC of a-Si films on glass substrates. How crystal grain sizes are affected by various types of intermediate dielectric layers is the main question that is answered. How crystallinity of silicon films are done by considering thermal conductivity of those intermediate dielectric layers.

In Chapter 4 improvements of line focus scan are done. Optical system is optimized and employed in order to scan the silicon films. By this way, scanned regions of silicon films are examined by considering thicknesses of the silicon films over the glass substrates. Heat accumulation and its influence over the crystallization process are explored. Relations which are between pulse overlaps and crystallinity are unveiled. Moreover, how the pulse overlaps change surface morphology is investigated.

Chapter 5 discusses defects which are formed by the laser irradiation due to inadequate pulse parameters and the material contents of the silicon films.

Chapter 6 is dedicated to concepts of device designs. Two types of junctions are included in detail. Namely, homojunction and heterojunction device-like structures are designed and tested. Successes and failures of those devices are handled by comparing quantitative measurements.

Chapter 3 - 6 include detailed explanations about the achievements but also reports on failures encountered during the research for a comprehensive understanding of the physical mechanisms. This will hopefully provide the readers valuable hints to figure out problems without executing complicated analyses in their prospective research in this field.

In Chapter 7, the ultimate achievements are discussed. These achievements are not only related to the main goal of the research, which is fabrication of an ultra thin solar cell or a diode, they are also related with the explanation of dynamics that govern the crystallization of a-Si structures through a laser pulse. So the findings and experimental outcomes are discussed in context of how crystal structures form via laser irradiation and if and how their morphology can be controlled by the parameters of irradiation laser system.

CHAPTER 2

THEORETICAL BACKGROUND

The film melting and re-crystallization process cause minimal thermal damage to the supporting glass substrate by means of LC besides of faster processing time among the advantages over the other annealing methods. Hence, understanding the melting/solidification process induced via nanosecond duration pulsed laser irradiation becomes essential. For this purpose the dynamics of LC process is discussed in detail in this chapter.

2.1 Theory of laser crystallization of amorphous silicon

There are several techniques that can be employed for deposition of a-Si on glass substrates, such as e-beam, plasma enhanced vapor deposition (PECVD), physical vapor deposition (PVD). PECVD typically results in a-Si:H where e-beam and PVD result in pure a-Si.

An a-Si film of several 100 nanometers thickness is subjected to pulsed laser irradiation and the a-Si film is liquefied upon absorptive heating. A fraction of the irradiated light is absorbed by the film and creates electrons that thermalize with a time constant of about 10^{-11}s [1]. In this short time the electrons approach a thermal equilibrium with the lattice, and thus a part of the deposited energy is transferred to phonons. Ultimately, heat propagates through the sample by phonons and charge carrier diffusion [1].

An important factor is the laser fluence. Fluence is defined as the deposited energy per surface area. The laser crystallization can begin if the laser fluence is close to the crystallization threshold energy of the specimen. The laser fluence can be increased

up to an extend by considering the hydrogen content (in case of PECVD deposited a-Si) and sample thickness so that the pc-Si grains are formed [1]. Usually, for this purpose hydrogen depleted a-Si is preferred as a starting material for laser crystallization and also it is well suitable for a single-laser pulse. If a-Si:H is used as a starting material, it can be problematic. When a-Si:H is liquefied during the LC process, it decomposes in H_2 gas and H-poor Si causing ablation of the Si [1]. Before LC process, a pretreatment process of lowering H content is a good start. In order to combine the advantages of high mobility of pc-Si with the light sensitivity of a-Si:H, the method laser dehydrogenation and crystallization was introduced [30]. With the increasing laser fluence the temperature of the silicon film increases up to a temperature of 1510 K until the complete melting is reached and then the excess laser energy causes heating of the liquid silicon (l-Si) to temperatures of about 2400 K [1]. Values of the laser fluence needed for complete melting of Si result in pc-Si grains and this laser fluence range is known as super lateral growth (SLG) regime [1, 31]. However, this regime has very narrow laser fluence window where pc-Si can be obtained with average sizes of up to a few micrometers [31, 32]. After threshold laser fluence is exceeded by increasing laser fluence, the grains, which are induced by individual pulses, also increase in size to a point at which the average grain size radii are almost equal to the thickness of the Si film [31, 33]. However, a further slight increase in the laser fluence causes a dramatic reversal in grain sizes, causing them to decrease , such that the growth of the crystallites are reversed and the film ends up to be made of finely grained pc-Si microstructures [31]. The growth of the grain in the SLG regime corresponds to the liquid phase regrowth from the discontinuous and small solid seeds which are never fully molten and the enlargement of the grains can be provided by lower quenching rate, which in return provides more time for lateral growth to take place before undesired nucleation intervenes [31]. This issue can be managed by increasing the temperature of the substrate up to some extent. After the complete melting, slight increase in the laser fluence sustains the melting. l-Si cools with a rate of more than 10^{10} K/s until the nucleation temperature is reached [1]. This supercooling (undercooling) of l-Si is above the melting temperature, i.e., that exceeds 200 K more than the melting temperature and a temperature increase takes place due to the latent heat release upon spontaneous nucleation and recrystallization to fine-grained pc-Si structures [34]. It should be noted that pc-Si melts at about same melting tem-

perature of bulk c-Si where on the contrary, the measured melting temperature of a-Si is lower by approximately 140 K [34].

The increase in the Gibbs free energy difference is the driving force of crystallization at a temperature which is 230 K lower than the equilibrium melting temperature of c-Si, so that l-Si undercools and nucleation temperature is reached at that point [1].

Melting and solidification are sustained by heat and mass transport which can occur by heat conduction and/or diffusion in the liquid phase. In order to examine the phase transformation of silicon, the dynamics of phase changes should be studied by considering liquid, amorphous and polycrystalline phases. For this purpose, the phenomenon of explosive crystallization is investigated in the following section.

2.1.1 Interface dynamics of crystal growth

Measurements of the free energy revealed that the a-Si should melt at a temperature several hundred degrees below the c-Si [35]. When the laser irradiation impinges on the a-Si layer, the low laser fluence melts a thin a-Si layer. As this l-Si begins to solidify in the form of pc-Si, the latent heat becomes released and that raises the temperature of the solidified pc-Si to values above the melting temperature of a-Si (T_a), so that the peripheral a-Si regions start to melt. The l-Si region becomes undercooled with respect to the pc-Si region; hence, l-Si resolidifies as finely grained pc-Si again [35]. This thin liquid layer of Si is supposed to propagate due to the released latent heat through a-Si regions, i.e., this l-Si region mediates an explosive crystallization [35]. The self-sustaining feature of the explosive crystallization is quenched by a loss of energy that is required to increase the temperature of the solid a-Si in front of the l-Si region to T_a. Due to the thermal conductivity difference between the a-Si and c-Si, explosive crystallization can continue through the amorphous-crystal interface at low laser fluences before being affected by thermal conduction into the underlying substrate [35]. As the laser fluence is increased, large-grained pc-Si structures emerge at the surface and grow at the expense of fine-grained pc-Si and a-Si regions, until they both vanish [36]. It was suggested that explosive crystallization is triggered by the rapid pc-Si nucleation in highly supercooled l-Si at/near the highly supercooled l-Si/a-Si interface [37]. To understand the theory of the interface dynamics, the rate

equations for the velocity of interface must be considered [38]. The transition rate at which the atoms of silicon leave the liquid phase to the solid phase, K^{ls}, is so called the forward transition rate; conversely, the transition rate from the solid phase to the liquid phase, K^{sl}, is considered as the backward transition rate. In case of $K^{ls} = K^{sl}$, there is thermodynamic equilibrium in which no motion of the liquid-solid interface takes place. During the solidification process, the melt front turns into solid with a velocity of v [39, 40]. The phase transformation diagram is provided in Figure 2.1. It can be seen that, the velocity of the interface, v, can be written as follows: if the liquid to solid transformation takes place under the condition of $K^{ls} > K^{sl}$,

$$v = K^{ls} - K^{sl} \tag{2.1}$$

In the case of $K^{ls} < K^{sl}$, the velocity of transformation from solid to liquid phase is in backward direction.

The rates of transformations are usually given as follows [39],

$$K^{ls} = C^{ls} e^{\left(-\Delta H^{ls}/k_B T\right)} \tag{2.2}$$

$$K^{sl} = C^{sl} e^{\left(-\Delta H^{sl}/k_B T\right)} \tag{2.3}$$

where k_B is the Boltzmann constant; ΔH^{ls} and ΔH^{sl} are activation energies required to transform $l \rightarrow s$ (liquid to solid) and $s \rightarrow l$, respectively. The relation of these activation energies to L_c is given as $L_c = \Delta H^{ls} - \Delta H^{sl}$ which is the latent heat of the phase change (see Figure 2.1) [39]. The factors C^{ls} and C^{sl} are the constants that are related to the entropy of the phases [41].

By substituting Equations (2.2) and (2.3) into Equation (2.1) the interface velocity, v, is found as

$$v = K^{sl}\left[1 - \left(C^{sl}/C^{ls}\right) e^{\left(-L_c/k_B T\right)}\right] \quad , \tag{2.4}$$

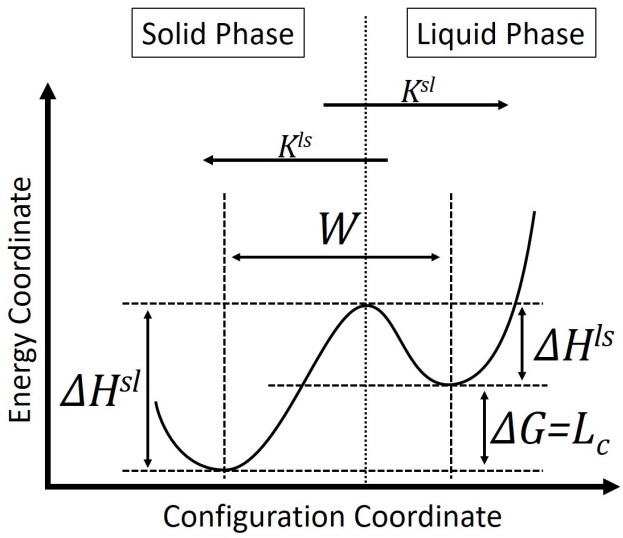

Figure 2.1: Energy relations

where the expression C^{sl}/C^{ls} can be written as

$$C^{sl}/C^{ls} = e^{\left(-L_c/k_B T_c\right)} \quad . \tag{2.5}$$

Here, T_c denotes the melting temperature of the crystalline phase since the complete crystallization is considered here (as opposed to amorphization). If the change in the Gibbs free energy ($\Delta G = \Delta H - T\Delta S$) upon crystallization is zero at T_c, the term L_c becomes equal to $\Delta S_c T_c$, so that Equation (2.1) becomes

$$v = K^{sl}\left[1 - e^{\left(-\Delta S_c (T_c - T)/k_B T\right)}\right] \quad . \tag{2.6}$$

If the temperature of the interface, T_i, is measured and the undercooling degree, $\Delta T_i = T_c - T_i$ is determined, then the velocity can be evaluated [39] as

$$v = K^{sl}\left[1 - e^{\left(-L_c \Delta T_i/(k_B T_c T_i)\right)}\right] \quad . \tag{2.7}$$

Here, it is worth to mention that the quantity $L_c/(k_B T_c)$ is determined to be a value of 3.62 for Si in Reference [39].

In order to simplify and convert Equation (2.7) to a more general expression, it can be

modified as in Reference [41] by replacing K^{sl} and T_c with $C_1 e^{\left(-Q/(k_B T_i)\right)}$ and T_{eq}, respectively such that it becomes

$$v = C_1 e^{\left(-Q/(k_B T_i)\right)} \left[1 - e^{\left(-L_c \Delta T_i/(k_B T_{eq} T_i)\right)}\right] \quad . \tag{2.8}$$

Equation (2.8) is the kinetic condition at the moving boundary (the interface response function) and can be considered as in the case of a nonequilibrium (nonisothermal) condition [42]. Here Q is the activation energy for self-diffusion in liquid, C_1 is a constant related to the material and T_{eq} is the temperature of the equilibrium phase transition.

This theory can be considered quite reasonable to describe the heterogeneous transformation of silicon qualitatively [43, 44]. Computer simulations and experimental results show that the velocity of the interface takes a value between 10-20 m/s mediated by a thin layer, which culminates in crystal growth by supercooling below the depressed melting point of c-Si [35, 37, 43, 44].

2.1.2 Laser induced phase transformation

The laser induced phase transformation begins with an optical process and light-mater interactions dominate this process vastly. There are two dominant processes in semiconductor-light interactions which can be so-called dielectric-like and metallic-like in accordance with the nature of absorption of the light energy [45]. The interaction mechanism can be given mainly under 4 interactions as follows [45, 46]:

- **Dielectric interaction:** $h\nu << E_g$
  In this interaction, only direct excitation of lattice vibration by absorption of light with photon energy $h\nu$ which is well below the band gap energy, E_g, takes place, while ignoring multi-photon processes and the absorption by impurities. This results in generation of coherent hypersonic phonons [45].

- **Metallic interaction:** $h\nu < E_g$
  In this interaction, excitation of free or nearly free carriers start to take over the

process, while ignoring multi-photon processes and the absorption by impurities again. The energy is transferred in the form of heat to the lattice.

- **Induced metallic interaction:** $h\nu > E_g$
  In this interaction, free carriers are generated by absorption of light by valance electrons where electron-hole pairs recombine through nonradiative transitions and transfer the energy in the form of heat [45, 46]. The time of nonradiative transition is longer than the case as in a semiconducting interaction.

- **Semiconducting interaction:** $h\nu > E_g$
  In this interaction, electron-hole excitation occurs by absorption of light, of which recombination lifetimes are sufficiently short; moreover, the nonradiative transition time is short. The absorbed energy by the free carriers (viz. equilibrium or nonequilibrium carrier densities are less than the absorption in semiconductors.) is transferred in the form of heat [45].

Besides of these aforementioned mechanisms, ion-implanted materials can be considered differently. The ions in the processed semiconductors can change the nature of the light absorption dramatically [46].

In order to discuss the previous mechanism, we proceed with the fundamental light-matter interaction and heating. There are two main optical processes taking place in heating of semiconductors. First, the reflection of light from the surface of the material, which determines how much energy can enter the specimen and second, the absorption of light energy, which decide where and how much of the light energy is transferred to the material [1]. For a homogeneous optical medium the Beer-Lambert Law states

$$I(d) = I_0 e^{(-\alpha d)} \qquad , \tag{2.9}$$

where I is the intensity of laser energy after the light propagates through a material of thickness d, which has an optical absorption coefficient, α, and the incident intensity of light just before entering the material is I_0. It should be noted that a dramatically steep increase in temperature and inhomogeneities in the material alter the refractive

index, n and the extinction coefficient, k. Therefore, α changes within small space intervals inside the semiconducting material [1]. In Equation (2.9), the reflection is not considered. However, a more general way of considering an optically inhomogeneous medium and absorbed light density can be expressed as

$$I(D) = (1 - R)I_0 e^{\left(-\int_0^D \alpha(x,T)dx\right)} \quad , \tag{2.10}$$

where R is the Fresnel reflectivity of the medium, and α depends on the position along the depth of the material, x and temperature T where D is the thickness of the irradiated layer [1, 47].

Now it can be discussed how the heating of the thin film occurs. The absorption of the light energy starts by means of electron excitations, e.i., the excess energy decays in time of the order of 10^{-12} s^{-1} by collisions with thermal vibrations and free electrons [48]. The absorbed light energy is converted into local heat, which can diffuse through a few hundred nanometers of material in a time interval of 10^{-10} s [48]. This absorbed light also causes interband and intraband transitions which result in formation of dense and hot electron-hole plasma [49]. The carriers diffuse, recombine and transfer their kinetic energy to the lattice where it is worth to mention that the electron-hole recombination time is between 10^{-11}s and 10^{-9}s [46, 49]. The laser light energy is transferred to the lattice within a depth determined by the carrier diffusion rather than the absorption coefficient of the semiconductor at the high excitation rate during the laser irradiation [46]. Under these circumstances the absorption process becomes non-linear due to the contribution of produced carriers and the temperature dependent light absorption of the material [49]. Besides, the reflection of Si which increases by a factor of 2 plays a crucial role when it melts [46].

A nonequilibrium (nonisothermal) model can be proposed in order to construct a more adequate physical point of view for the description of a dynamic process [42]. For simplicity, one-dimensional Stefan's model (Josef Stefan, 1889) can be used to constitute the basis of a differential equation to describe the heat conduction in both the solid and liquid phases. This differential equation includes a source term that

emerges due to the absorption of the light energy, i.e.,

$$\rho_i c_i \frac{\partial T_i}{\partial t} = \frac{\partial}{\partial x}\big(K_i \frac{\partial T_i}{\partial x}\big) + S_i(x,t) \quad , \quad i = l, pc, a, sb \qquad , \tag{2.11}$$

where, ρ is the mass density, c is the specific heat, T is the temperature, K is the thermal conductivity, S is the source term, and x and t are the space and time variables. The index i denotes the phases of the material such as liquid (l), polycrystalline (pc), amorphous (a) and substrate (sb). There is an interesting feature of metallic liquid silicon such that the density of l-Si, ρ_l, at melting temperature is $\sim 10\%$ higher than that of the solid Si, ρ_{pc} at room temperature [50].

The physical process begins with the absorption of the light energy and heating of the material. The solid material is heated without a phase transition until the surface reaches a temperature that is high enough to initiate the melting of the film [51, 52]. After a while the liquid layer begins to solidify as fine grain pc-Si forms and the latent heat releases during this re-solidification [52]. The latent heat of a-Si, L_a, can be almost 60% of the latent heat of the c-Si, L_c, i.e., $L_a \approx 0.6 L_c$ [46] that has an important impact in the laser crystallization. It should also be kept in mind that the a-Si melts at several hundreds degrees below (≈ 250 °C) the melting temperature of c-Si [35]. The a-Si regions begin to melt due to the latent heat release and the rapid cooling and severe supercooling of the liquefied a-Si with respect to c-Si regions results in nucleation of fine grained pc-Si [53]. The nucleation temperature can be deduced by

$$\int_{T_n}^{T_l} c_l(T) dT = \chi \Delta H_m \qquad , \tag{2.12}$$

where T_n and T_l are the temperature of nucleation and the temperature of l-Si during the normal solidification, c_l is the temperature dependent specific heat of l-Si, χ is the volume fraction of solid Silicon present after recalescence, and ΔH_m is the enthalpy of solidification [53].

Due to excessive latent heat, the rise in temperature makes the liquefied layer propagate through the amorphous regions and the phase transition spread rapidly through the amorphous material and hence, it is called the “explosive crystallization (EC)“

[52]. It should not be presumed that the evaporation does not occur in this phenomenon; on the contrary, the evaporation from the surface of the Si film can cause significant differences for higher energy densities whenever the surface temperature reaches the boiling point of Si [54].

The explosive crystallization has a nonequilibrium property. Eventually, the Stefan problem turns into a nonequilibrium process with four phases (i.e., l-Si, pc-Si, a-Si, and Si vapor) and three moving boundaries (i.e., liquid/vapor interface, pc-Si/l-Si and pc-Si/a-Si interfaces) [51].

Before defining the heat balance for the interfaces, let's define the volume source term [52] (see Equation (2.10) arising due to laser irradiation in Equation (2.11)):

$$S_i(x,t) = [1 - R(t)]\alpha(x) I_0(t) e^{\left(-\int_{Z_0(t)}^{x} \alpha(\eta) d\eta\right)} \quad , \tag{2.13}$$

where $I_0(t)$ is the power density (power per unit area) due to the laser pulse intensity profile at the surface of the layer, $\alpha(x)$ is the optical absorption coefficient at the position x, $R(t)$ is the reflectivity depending on time (as well, it can be written as temperature dependent.), $Z_0(t)$ is the time-dependent position of the surface of the Si layer (or the liquid/vapor interface). The heat balance condition at the liquid/vapor interface can be written as

$$\rho_l L_v \frac{dZ_0}{dt} = K_l \left(\frac{\partial T}{\partial x}\right)_{Z_0(t)_+} - \epsilon\sigma\left(T_{Z_0}^4 - T_e^4\right) \quad , \tag{2.14}$$

where L_v is the latent heat of evaporation for silicon, ϵ is the emissivity from the liquid surface, σ is the Stefan-Boltzmann constant, T_{Z_0} is the temperature of liquid/vapor interface, and T_e is the ambient temperature [51]. The dynamics of evaporation in vacuum can be expressed as

$$\frac{dZ_0}{dt} = \frac{1}{\rho_l}\sqrt{\frac{M}{2\pi R_g}} T_{Z_0}^C \times 10^{-(A/T_{Z_0})+B} \quad , \tag{2.15}$$

where R_g is the universal gas constant, M is the molar mass, and A, B, C are constants determined experimentally [52].

The heat balance condition on the pc-Si/l-Si interface and the kinetic condition can be expressed, respectively as

$$\rho_{pc} L_{pc} \frac{dZ_1}{dt} = K_{pc} \left(\frac{\partial T_{pc}}{\partial x} \right)_{Z_1(t)_+} - K_l \left(\frac{\partial T_l}{\partial x} \right)_{Z_1(t)_-} \quad , \tag{2.16}$$

$$\frac{dZ_1}{dt} = C_1 (T_{Z_1} - T_{pc}) \quad , \tag{2.17}$$

where L_{pc} is the latent heat of melting of pc-Si, $Z_1(t)$ is the position of the pc-Si/l-Si interface, T_{Z_1} is the temperature of pc-Si/l-Si interface, C_1 is a constant, and T_{pc} is the equilibrium melting temperature of pc-Si [51].

For the explosive crystallization front the heat balance condition and can be written , respectively as

$$\rho_a L_{EC} \frac{dZ_2}{dt} = K_{pc} \left(\frac{\partial T_{pc}}{\partial x} \right)_{Z_2(t)_-} - K_a \left(\frac{\partial T_a}{\partial x} \right)_{Z_2(t)_+} \quad , \tag{2.18}$$

$$\frac{dZ_2}{dt} = C_2 (T_{Z_2} - T_{EC}) \geq 0 \quad , \tag{2.19}$$

where L_{EC} is the latent heat released during the EC process, $Z_2(t)$ is the position of the EC front, T_{Z_2} is the EC front, C_2 is a constant, and T_{EC} is the equilibrium crystallization temperature [52]. The velocity term dZ_2/dt is taken in positive direction customarily since the transition occurs from a-Si to pc-Si. The latent heat released during the EC is also given as

$$L_{EC} = L_{pc} - L_a \quad . \tag{2.20}$$

The term L_{EC} is the difference between the latent heat of crystallization and the latent heat of melting of a-Si at the propagating interface of EC [52].

In order to compute the aforementioned equations, the boundary conditions and initial conditions can be defined as follows [51],

$$\frac{\partial T(D,t)}{\partial x} = 0 \qquad , \tag{2.21}$$

$$T(x,0) = T_0 \qquad , \tag{2.22}$$

$$Z_0(0) = Z_1(0) = Z_2(0) = 0 \qquad , \tag{2.23}$$

where D is the thickness of the sample, T_0 is a constant temperature of the sample and x is defined in $[0, D]$.

Simultaneous computation of these equations can lead to predict the evolution of the EC of Si layer over a specific substrate. In order to attain a more detailed perception, the heat accumulation due to successive pulses on the surface should be considered. In this respect, the overlap of the pulses is discussed in the next chapters.

2.2 Line focus scanning optics

The line focus optics are designed and mounted under the scanning optics of the laser marking system. This line focus system is constructed in order to form a line shaped focus on the surface of silicon films. This enables to scan larger areas with a single pulse of laser irradiation. Diagram of the line focus optics is shown in Figure 2.2.

In Figure 2.2 the laser beam impinges on the scanning (galvo) mirror and is reflected to the telecentric F-Theta (F_θ) lens set. The telecentric F_θ lens makes the beam focused perpendicularly on a surface which is intended to be processed. This beam always perpendicularly impinges on the surface during the movement of the galvo mirror. By scanning the cylindrical lens through its own symmetry axis the laser beam is always normal to the surface. The optical property of the cylindrical lens the beam is expanded in one direction and it is perpendicular to the symmetry axis of its own. The curved side of the cylindrical lens faces to the F_θ lens set in order to

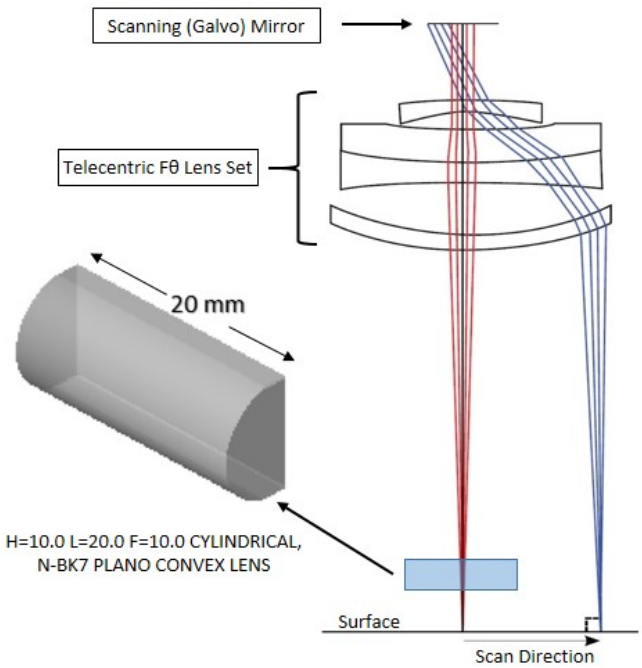

Figure 2.2: Line focus optics

diminish the aberrations caused by the cylindrical lens. The equivalent optics system can be calculated by matrix method [55] as follows,

$$\begin{bmatrix} h_f \\ \alpha_f \end{bmatrix} = T_c R_c T_\theta R_\theta \begin{bmatrix} h_i \\ \alpha_i \end{bmatrix} \quad . \tag{2.24}$$

Equation (2.24) is written as a matrix that constitutes of translational and refraction matrices of the cylindrical and the telecentric F_θ lenses and designated as T_c, T_α and R_c, R_α, respectively. Where h_i is the distance where the beam radius covers when the beam axis and the lens axis coincide and α_i is the convergence angle between the axes of the converging beam and the lens. Where h_f and α_f are the final distance of the beam edge from the optical axis and the divergence angle of the beam borders at the position where the beam impinges, respectively. The equation can be written explicitly as follows,

$$\begin{bmatrix} h_f \\ \alpha_f \end{bmatrix} = \begin{bmatrix} 1 & x \\ 0 & 1 \end{bmatrix} \begin{bmatrix} 1 & 0 \\ -1/f_c & 1 \end{bmatrix} \begin{bmatrix} 1 & f_\theta - x \\ 0 & 1 \end{bmatrix} \begin{bmatrix} 1 & 0 \\ -1/f_\theta & 1 \end{bmatrix} \begin{bmatrix} h_i \\ 0 \end{bmatrix} \quad . \tag{2.25}$$

Equation (2.25) shows that the laser beam converges to the F_θ lens from the galvo mirror parallel without any angle between the beam axis and the axis of the F_θ lens where f_c and f_θ are the focal distance of the cylindrical lens and the F_θ lens respectively. In Equation (2.25) the dependent variables are given as x and h_f where x determines the distance of the cylindrical lens from the surface where the focal point of the F_θ lens is fixed and the length of the line focus can only be changed by changing the position of the cylindrical lens and h_f determines the length of the line focus on the surface. If the above equation is calculated the matrix becomes,

$$\begin{bmatrix} h_f \\ \alpha_f \end{bmatrix} = \begin{bmatrix} -h_i x^2/(f_c f_\theta) \\ -h_i(f_c + x)/(f_c f_\theta) \end{bmatrix} \quad . \tag{2.26}$$

By using Equation (2.26) the length of the line focus, l, or the distance of the cylindrical lens from the surface, x, can be written in terms of each other as follows,

$$l = \frac{2h_i}{f_c f_\theta} x^2 \Longrightarrow x = \sqrt{\frac{f_c f_\theta}{2h_i} l} \quad . \tag{2.27}$$

Here l or x can be parameterized with respect to each other.

2.3 Analysis of crystallinity

Raman spectroscopy, electron backscatter diffraction (EBSD), X-ray diffraction (XRD) and scanning electron microscopy (SEM) methods are employed in order to determine the crystallinity of silicon in general [56–65]. Not only are the aforementioned methods able to define the crystallinity of Si but also they can provide crystallization degree of the material quantitatively. However, the Raman spectroscopy and EBSD analysis have superior features over XRD method. Raman spectroscopy has ability to focus on areas with sizes in the order of several hundred nanometers and this technique is capable of determining magnitudes of stresses over the crystalline grains with a great precision [58, 60–62]. The method of EBSD reveals orientations and sizes of the crystallized grains even for the crystallites of nanometer size [6, 7, 24, 26]. So as to be more precise, the crystallinity analyses are done by means of micro-Raman

spectroscopy and EBSD method in this study and the measurements are acquired not only with qualitative results but also with quantitative results.

The crystallinity of the LC processed regions are checked by Raman spectroscopy by which the tensile stresses over the crystal grains are found. The domain orientations of the crystallized regions are analyzed by EBSD and the bending/twisting effects over the elongated laser crystallized regions are shown in Chapter 4.

Here, a brief information is necessary to understand the Raman spectroscopy. When light impinges on a surface and gets scattered from that surface, almost all of the scattered light undergoes an Rayleigh scattering process, i.e., an elastic process. Nonetheless, a very small amount of scattered light is subjected to an inelastic process. Hence, this scattered light has different energy from the incident one. The measurement of Raman effect is utilized here. The Raman effect is an adequate phenomenon in order to identify the materials and their morphology (see Figure 2.3). Measuring Raman shift of a material gives an intrinsic signature of that material.

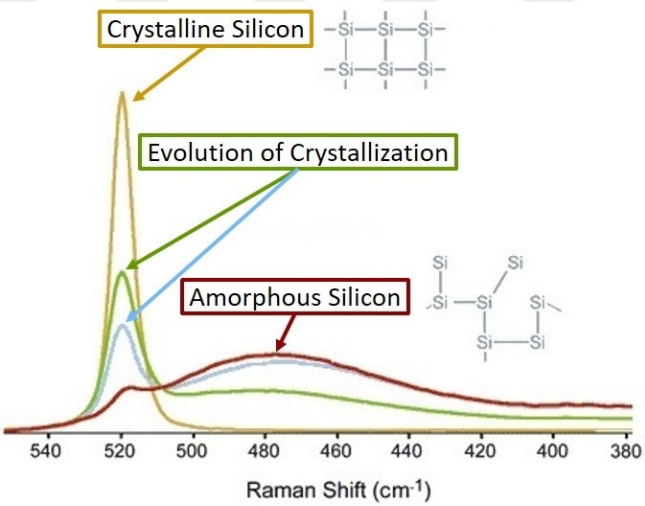

Figure 2.3: Raman Spectra of Silicon

The equation of the Raman shift can be written in terms of the wavelengths of the excitation and scattered lights as in Equation (2.28).

$$\nu = \frac{1}{\lambda_e} - \frac{1}{\lambda_s} \quad , \tag{2.28}$$

where ν is the Raman shift, λ_e is the excitation wavelength of the light, which is the

incident light and λ_s is the wavelength of the scattered light from the surface.

The reason of calculating the Raman shift as wavenumber is that there is a linear relation with energy and makes the form of the Raman spectrum independent of excitation wavelength [66]. For example, the Raman peak of crystalline silicon always appears at a wavenumber of 521 cm^{-1} whatever excitation wavelength is used. However, if the horizontal axis of the graph in Figure 2.3 is replaced as the wavelength, the Raman peak of silicon appears at 547.14 nm when 532 nm excitation is used and 818.41 nm with 785 nm excitation [66].

In addition to the analysis on Si crystallinity, the surface roughness of the LC processed Si regions are examined via atomic force microscopy (AFM). The AFM has ability to acquire topographical maps of surfaces with nanometer resolution spatially. Basic of the AFM is to measure forces between atoms or/and molecules with piconewton precision.

The secondary ion mass spectroscopy (SIMS) measurements are performed via TOF-SIMS 5 [67], which provides a full depth analysis via bombarding target regions by primary ions of keV energy and part of this energy is transferred to the surface allowing surface molecules or/and atoms to overcome the surface binding energy. The emerging secondary ions from the surface with different atomic masses arrive to the detector with different velocities which correspond to different times of flight required for traveling from the target region to the detector. The variations in time of flight (TOF) of the different weighted ions allow to determine the elemental analysis of the target. This technique is a destructive method which leaves a crater on the target surface. The target surface is scraped off layer by layer that allows depth profiling of the examined material. The scraping time and types of the removed materials are recorded on the device memory. Concentrations of the various ions are recorded with corresponding counts which are proportional to the concentrations of that different ions during the ongoing measurement. If a thin film on a specific known substrate is analyzed by the TOF-SIMS and the thickness of the film is known, the process time of the TOF-SIMS can be made to coincide with the thickness of the thin film.

CHAPTER 3

EFFECTS OF INTERMEDIATE DIELECTRIC LAYERS ON LASER CRYSTALLIZATION OF AMORPHOUS SILICON FILMS

3.1 Overview of laser marking systems

Two types of laser marking systems are used in this study; these are namely EO Technics SuperMarker GF311 and FiberLast Flast-NanoMARK 50W marking lasers (see Figure 3.1). These laser are diode pumped MOPA lasers with Ytterbium ion (Yb^{3+}) doped fiber amplifiers. The technical specifications of the laser marking systems are given in Table 3.1 and 3.2 respectively (The specifications are supplied by the manufacturers).

(a) EO Technics SuperMarker GF311 (b) Flast-NanoMARK 50W

Figure 3.1: Laser marking systems

Before employing the laser markers for crystallization of Si thin films, the specifications of these systems are tested and real laser and optical parameters are determined. These parameters are specified throughout the dissertation in detail. Some modifica-

Table 3.1: EO Technics SuperMarker GF311

EO Technics SuperMarker GF311	
Wavelength	1064 nm
Max. Average Power @ 1064 nm	30 Watt
Pulse Width	200 ns
Scan Optics	CVI FTL-1064-254

Table 3.2: Flast-NanoMARK 50W

Flast-NanoMARK 50W	
Wavelength	1064 nm
Max. Average Power @ 1064 nm	50 Watt
Pulse Width	40 ns - 500 ns
Scan Optics	SCANLAB 112847

tions are made on the laser marker, Flast-NanoMARK 50W, under the supervision of the manufacturer firm.

3.2 Preliminary studies over laser crystallization

Having determined the laser and optical parameters of the laser marking systems via several measurements, the crystallization of Si thin films are studied. For the consistency of experiments the parameters of both of the laser marking systems are measured meticulously. The power output levels and pulse widths of both lasers are measured via the thermopile detectors (viz. Newport 818-020-12, High Power Detector and Thorlabs S322C) and the fast silicon detector (viz. Thorlabs DET10A), respectively.

3.2.1 Determination of crystallization and damage thresholds with spot focus scan

Firstly, intrinsic amorphous silicon (i-a-Si) film is coated on a glass substrate, Schott AF 32 Eco, with a thickness of 1.1 mm via electron beam (e-beam) deposition technique. No buffer layer (intermediate dielectric layer, IDL) is used between i-a-Si thin film and the glass substrate. The crystallization is processed via the nanosecond

pulsed laser (EO Technics SuperMarker GF311) at the wavelength of 1064 nm (see Figure 3.2).

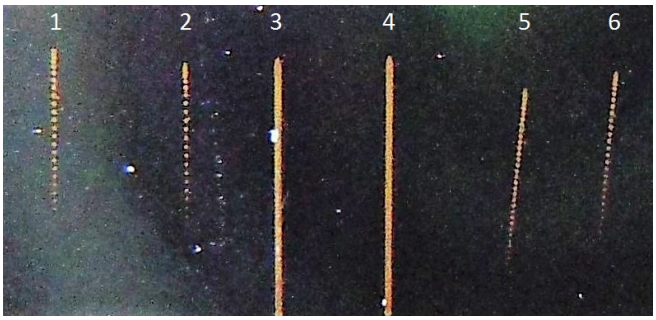

Figure 3.2: Laser crystallized lines over i-a-Si thin films of 650 nm

Black region is the i-a-Si film and the orange dotted and solid lines are the laser processed regions. The scan parameters are given in Table 3.3.

Table 3.3: Scan parameters of the laser marking system

Line Number (#)	Av. Power (W)	Rep. Rate (kHz)	v_s (mm/s)	Pulse Overlap (%)
1	0.44	30	1923	No Overlap
2	0.44	30	2060	No Overlap
3	1.67	70	2060	51
4	1.67	75	2060	54
5	0.44	30	1373	24
6	0.44	30	1648	8

The laser irradiated with a Gaussian beam on the surface of the film with a diameter of $\sim 45\mu$m. The laser optical parameters are given in Table 3.4.

Table 3.4: Optical parameters of the laser marking system

Line (#)	Av. Power (W)	Pulse Energy (μJ)	Peak Fluence (J/cm^2)	Av. Fluence (J/cm^2)
1	0.44	14.7	1.84	0.92
2	0.44	14.7	1.84	0.92
3	1.67	23.9	3.00	1.50
4	1.67	22.2	2.80	1.40
5	0.44	14.7	1.84	0.92
6	0.44	14.7	1.84	0.92

Note that in Figure 3.2, Table 3.3 and 3.4 include 6 lines which are laser processed

and some of the lines have the crystalline region illuminated with different overlap percentages. This is to show how the overlapping and non-overlapping pulses look macroscopically on the surface of the films. In the following, the structures which are illuminated with different optical powers are discussed. There are some information about the structures, not included previously in Figure 3.2, Tables 3.3 and 3.4. Their details are given separately.

The microscope images of the lines 1 and 4 are investigated and there is no damage observed (See Figure 3.3 and 3.4).

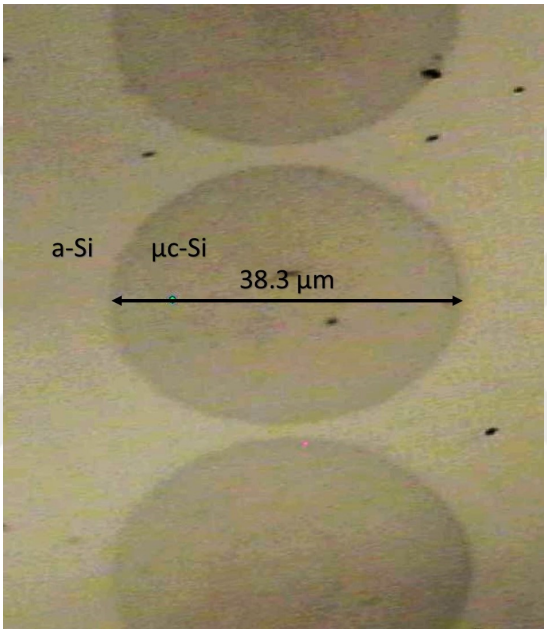

Figure 3.3: Microscope image of Line 1

The scan direction of the laser beam is vertical with respect to the figures orientation and the paper. The crystallization did not occur below the peak fluence of 1.84 J/cm^2. Here for the simplicity it seems to use the peak fluence values instead of the average fluence values. The peak fluence values can be converted into the average fluence by simply dividing by 2 and it customary to use peak fluence while considering the spot focus illumination with a Gaussian beam profile. In Figure 3.4, it is clearly seen that the spot focuses are overlapped up to some extent. The crystallized spots are stretched vertically in the direction of scan. While the laser beam is moving in some direction in the time pulse duration, the trace of the laser pulse continues and leave trace in that time interval. The individual laser pulses produce elliptical traces on surfaces and the

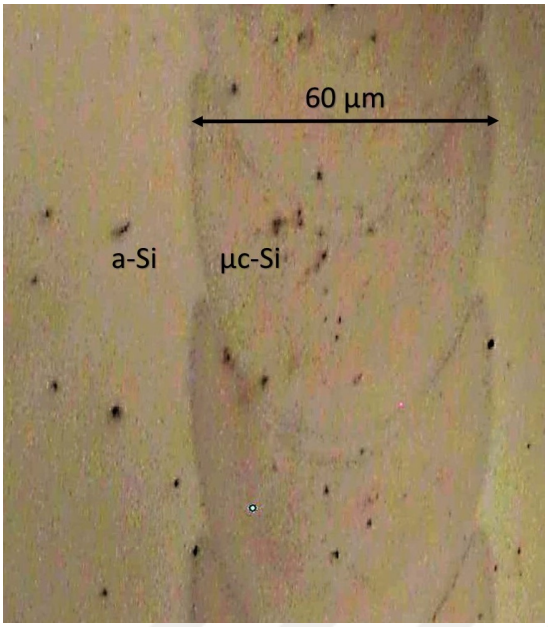

Figure 3.4: Microscope image of Line 4

eccentricity of those ellipse increases with increasing speed of the scan. Damages on the film surface appeared when the peak fluence exceeded the peak fluence of 2.8 J/cm^2. Figures 3.5, 3.6 and 3.7 show the damage occurrence on the film of 650 nm i-a-Si.

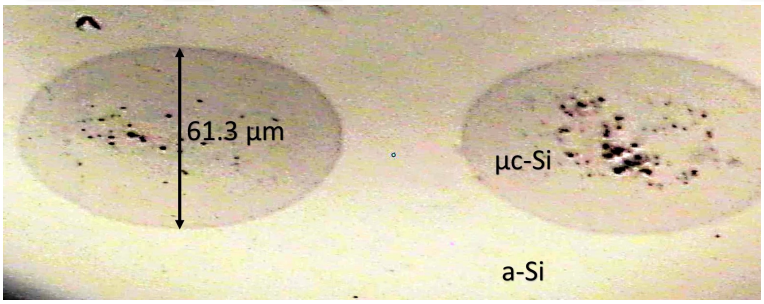

Figure 3.5: Damages appeared at the center of the laser crystallized region, micro crystalline silicon (μc-Si).

The damage emerged at the center of the crystalline silicon (μc-Si) films where the peak fluence can exceed the damage threshold energies at the very first. In Figure 3.7, the glass substrate can be clearly seen at the center of the laser mark. The Si film is totally removed by the excessive amount of energies. The peak fluences that applied to the surface of 650 nm i-a-Si film without any buffer layer between the glass substrate and a-Si layers. The thermal properties of various buffer layers and different

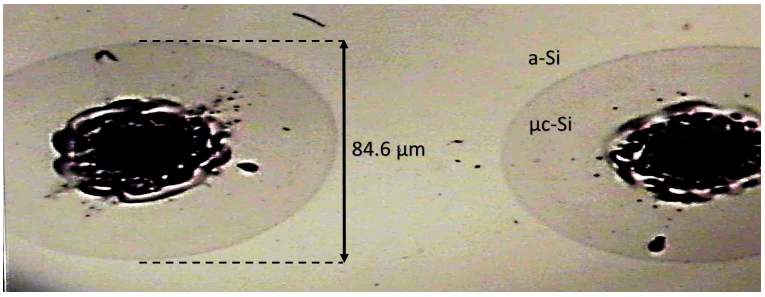

Figure 3.6: Damaged regions started to melt down and the uniform crystalline regions circumscribed them with increasing radii.

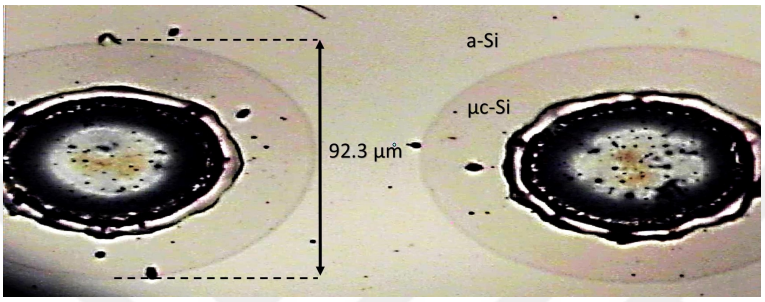

Figure 3.7: The damaged structures on Si films without pulse overlap

substrate materials exhibit different effects on the crystallization of a-Si films. The applied peak fluences differ with varying thicknesses of a-Si films. It is worth to mention that the achieved crystallized regions should be checked via micro-Raman spectroscopy before moving on. The Raman spectroscopic analyses of the observed regions mentioned previously are discussed in the following section in detail.

3.2.2 Raman spectroscopy and EBSD analyses

To be sure of that the crystallization occurs after laser process, the Raman spectroscopy should be done. The Raman spectroscopy system is Horiba-JobinYvon iHR550. During the Raman measurements a grating of 1800 grooves per millimeter is employed. In order to check the green laser illumination impinging on the pertinent crystallized regions, a microscope objective is employed. Before and after the Raman measurements, a bulk mono-crystalline silicon (c-Si) wafer is used in order to check for calibration of Raman spectroscopy system. The Raman peak signal of c-Si at room temperature (RT) is considered at the wavenumber of 521 cm^{-1} and the

wavenumber datum are shifted how much the measured Raman peak of c-Si shifted. The wave number 521 cm^{-1} is taken as a standard value so as to be consistent throughout the research. The full width at half maximum (FWHM) of the Raman peak of the c-Si wafer can vary through the research and at highly dependent on the ambient conditions so it is not set to a specific value in the thesis and the FWHM value of the c-Si is considered and compared with corresponding measurements whenever the Raman spectroscopy is done. To begin with the threshold trails, here the Raman Signal of Line 1 and 4 are given in Figure 3.8.

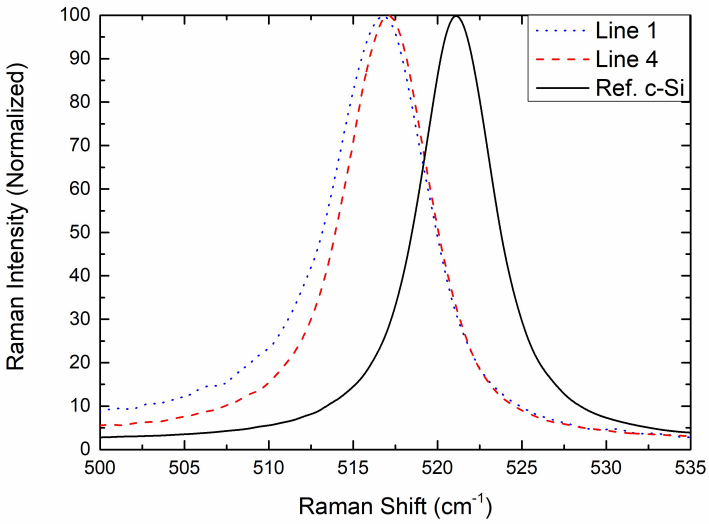

Figure 3.8: Si Raman spectra of Line 1 and Line 4

The analyses showed that the peak of the Raman signal of the reference c-Si is at 521 cm^{-1} and the FWHM of that is at $\sim$5 cm^{-1}. The calibration for the shift of the peak could have been done easily; however, the calibration or manipulation over the FWHM values, which are found, are left as they are. The FWHM values of the Raman signals throughout this work are discussed separately i.e. per experiment. The Raman signal peak of Line 1 is at 516.9 cm^{-1}; the FWHM is 6.9 cm^{-1} and the Raman signal peak of Line 4 is 516.9 cm^{-1}; the FWHM is 6.0 cm^{-1}. By looking the shift of the Raman peaks of Line 1 and 4, tensile stress occurs over the structures. The crystallinity of these structure can be deduced by considering the FWHM of the Raman signals. The FWHM values differ from each other that shows the crystal quality of Line 4 is better than that of Line 1. To compare the crystal qualities of Line 1 and 4 quantitatively, EBSD should be used. By means of EBSD method, the crystal

orientations and grain size of the crystals over the surface can be compared comprehensively. Figure 3.9 and Figure 3.10 show the SEM (ZEISS EVO HD15) images of Line 1 and 4; Figure 3.11a and 3.11b are the corresponding EBSD (AMETEK EDAX EBSD Device) images, respectively.

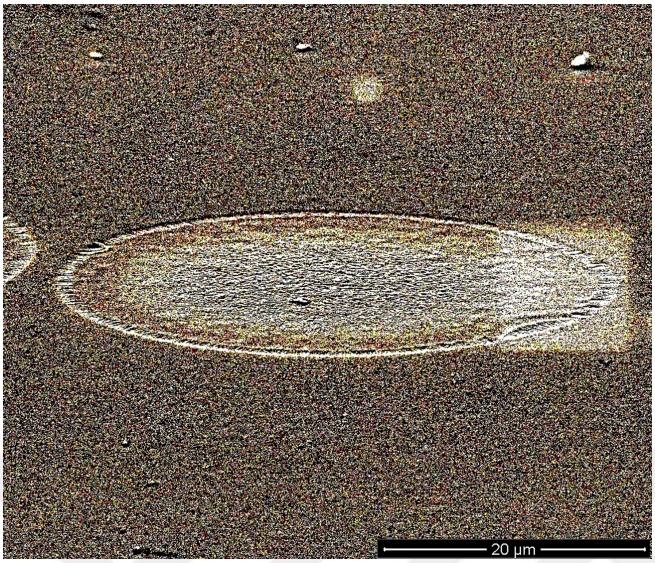

Figure 3.9: Colored SEM image of Line 1

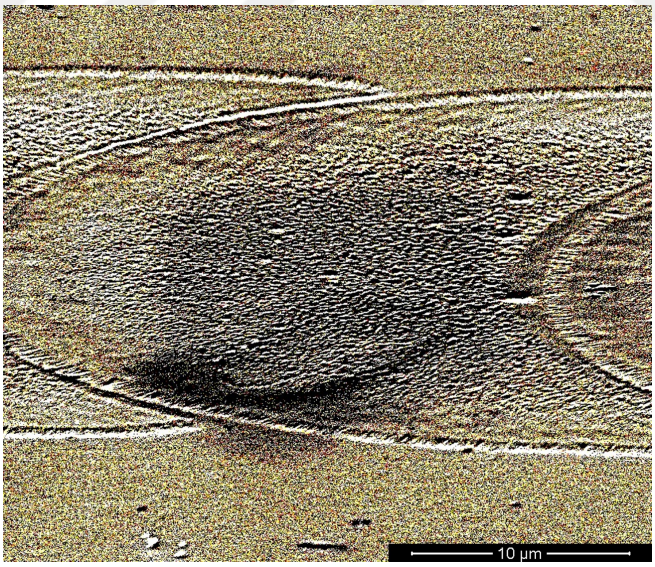

Figure 3.10: Colored SEM image of Line 4

SEM images of Line 1 and 4 are taken in order to observe detailed examination of the formed crystalline structures. In Figure 3.9 and Figure 3.10 the crystalline marks

of the laser pulses are seen clearly. Topography of the laser processed surfaces have more roughness than the non-processed regions. However, these analyses do not contain quantitative information. To provide quantitative information, an AFM (Nano-Magnetics Ambient) is used for roughness analyses.

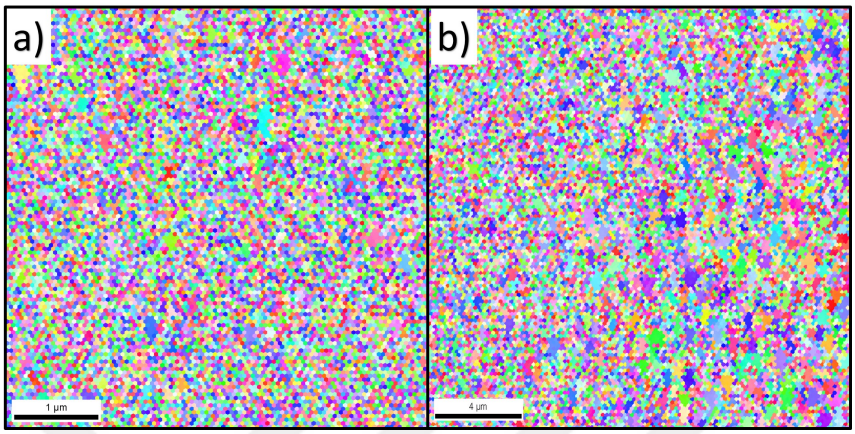

Figure 3.11: EBSD images of a) Line 1 and b) Line 4

As it is seen in Figure 3.11, there are nano-crystalline silicon (nc-Si) grains which are formed in both circumstances. In Figure 3.11a, nc-Si grains are smaller than in Figure 3.11b. As previously discussed, the Raman spectroscopy shows that Line 4 exhibits more crystallinity than the Line 1 does when the FWHM of the Raman signals are compared. Line 4 has larger grains accumulate at the right side of Figure 3.11b. As the grains increase in size, FWHM of Raman Signal of Si gets narrower. The observations above also proves this statement and shows the correlation between the grain size and FWHM of Raman signals.

3.2.3 Macro structural trials

In this section, it is tried to construct macro-sized structures with the spot focus scanning. In order to form macroscopic structure on the a-Si film, concentric circular patterns are drawn and the circular lines are separated by a distance of 40μm and the maximum diameter of the circle is 3.3 mm. The limitation stemming from the galvo scanning system of EO Technics SuperMarker GF311 a wicker basket base shaped patterns are formed at vicinity of centers and the patterns are not circular exactly, they are polygons (see Figure 3.12).

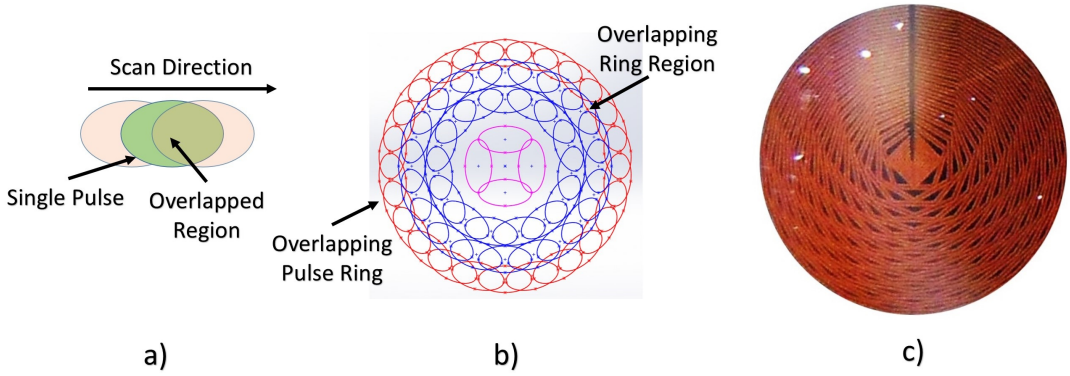

Figure 3.12: a) Demonstration of pulse overlap and b) Overlap of successive circular patterns. c) Produced macro structure with a diameter of 3 mm.

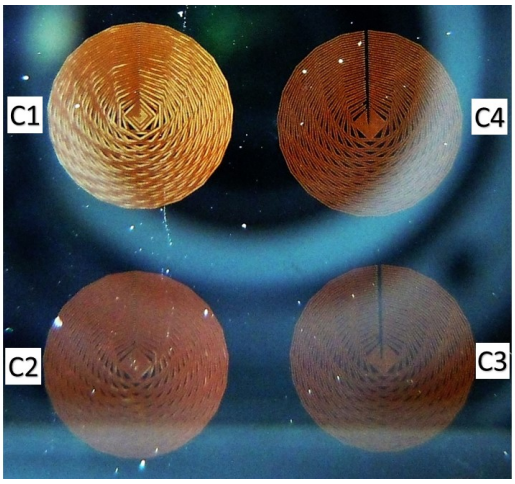

Figure 3.13: Macroscopic structures processed by spot focus

In Figure 3.13 four round shaped structure are formed and their scan parameters are given in Table 3.5.

Table 3.5: Laser scan parameters for Figure 3.13

Circle (#)	Av. Power (W)	Peak Fluence (J/cm^2)	Pulse Energy (μJ)	Pulse Overlap (%)
C1	1.36	2.14	17	97.6
C2	1.12	1.76	14	97.6
C3	0.65	1.02	8	97.6
C4	0.65	1.02	8	97.6

Even though the circles C3 and C4 have the same laser scan parameters, they are given separately because both the images of C3 and C4 in Figure 3.13. The only difference

is the color clarity between them because of the shooting angle of the camera. An also all the circles (C1-C4) are processed on the same specimen of a-Si thin film. The film thickness is also 650 nm i-a-Si film and this film is also prepared in the same condition with the previous specimens, discussed previously. In Figure 3.14 the microscope images of the crystallized circles are seen. The color of C3 and C4 are seen a bit different. The cause of the hue and color adjustments of the both images are done separately in order to highlight the crystalline structures.

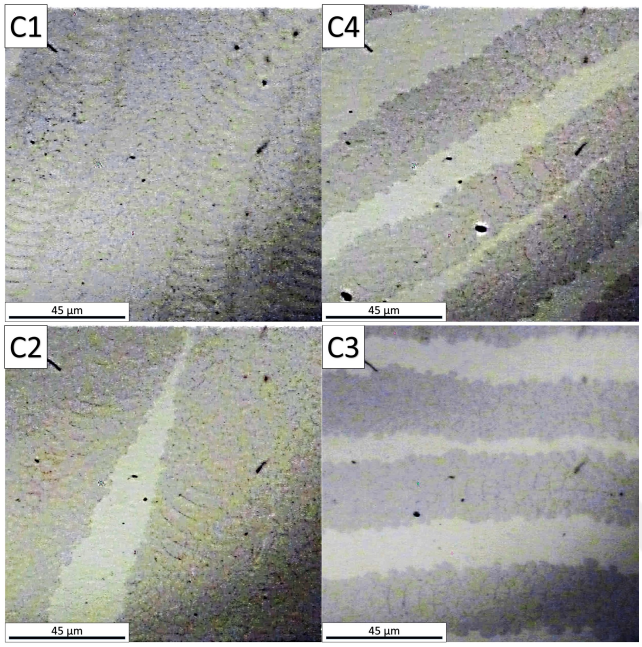

Figure 3.14: Microscope views of crystallized circles C1, C2, C3 and C4.

The scan parameters of the C3 and C4 are set the same with each other; therefore, the Raman analyses of them are done as a single plot which is given in Figure 3.15.

The Raman analyses of the circular patterns are compared with the reference c-Si again at the same conditions and time interval. The peak position of the Raman signal of the reference c-Si is at 521 cm^{-1} and the FWHM is about 5.1 cm^{-1}. The peak position of the Raman signals are measured as 518.3 cm^{-1}, 517.6 cm^{-1} and 517.6 cm^{-1} for C1, C2 and C3 (C4) respectively. The FWHM of the Raman signals are 5.6 cm^{-1}, 7.5 cm^{-1} and 8.4 cm^{-1} respectively. As it seen from the values, the stress over the structure are increased by the applied laser fluence directly; moreover, the crystallinity can be said to be improved also by looking the FWHMs. Having analyzed the crystallinity of the macroscopic circular patterns via Raman spectroscopy, the EBSD analyses are

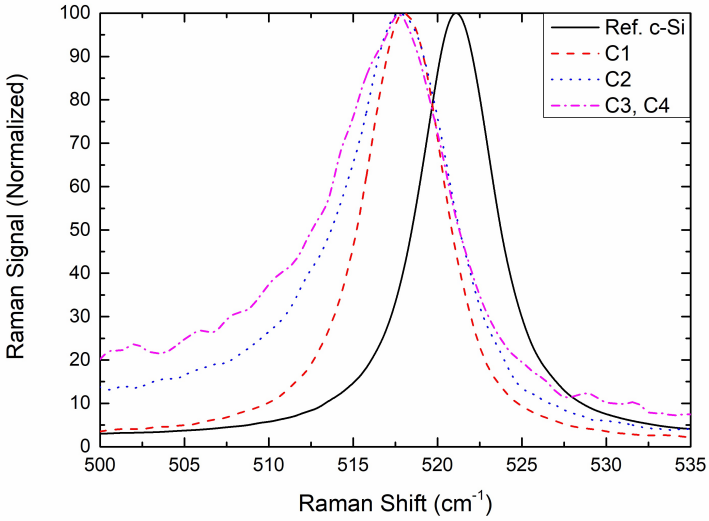

Figure 3.15: Si Raman spectra acquired from crystallized circular patterns

intended and the polishing should have been needed. When the prepared specimen is subject to polishing, it is observed that the surface of the patterns did not endure and they are wiped off partially (see Figure 3.16).

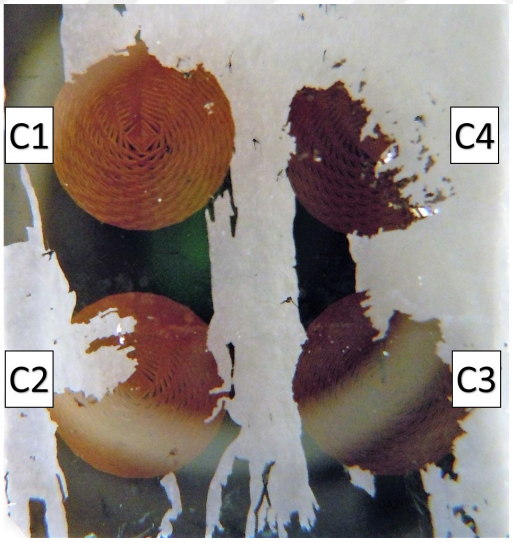

Figure 3.16: Damaged crystallized circular patterns via polishing

The mechanical stress caused by the polishing process wipes off the a-Si film and the crystallized patterns partially. However, the patterns (C1 and C2), formed by higher laser fluences abode the mechanical stress more than C3 and C4. Especially endurance of C1 is the highest. As a preliminary deduction can be considered that

the higher laser fluence which are close the value of damaging fluence forms robust crystalline structures over glass substrate. This deduction is discussed in the content of Section 3.3 and the reason of the stickiness of the crystalline structures forms with the laser fluences near the damage threshold values can be attributed to that bounding process between the μc-Si and the glass is needed more heat accumulation at the interface of the layers.

3.3 Laser crystallization of amorphous silicon films on various intermediate dielectric layers over glass substrate

In this section, different types of buffer layers or Intermediate Dielectric Layers (IDLs) and their effects on laser crystallization are discussed. Four types of IDLs, namely SiN_x, SiO_2, ZnO and TiO_2 are deposited between the amorphous silicon films and glass substrates. After deposition procedure, laser crystallization is applied and crystallization of Si films are examined via Raman and EBSD analyses. Diffusion and contamination through the crystalline layers are determined by SIMS method.

3.3.1 Preparation of thin films

The designed structure of the specimens are shown in Figure 3.17. The types of the intermediate layers and the film thicknesses are given in Figure 3.17, respectively. The process of the film deposition is given below in detail.

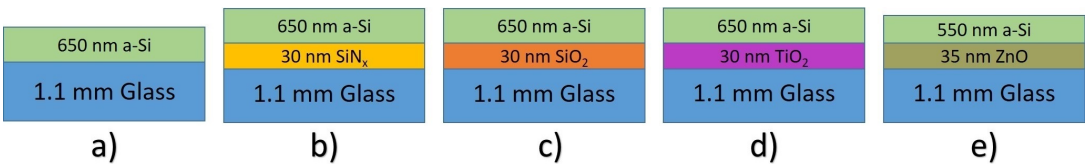

Figure 3.17: Designed structures in order to investigate the effects of intermediate layer types on laser crystallization of a-Si thin films

In all of the experiments, Schott AF 32 Eco glass with a thickness of 1.1 mm is used as substrate. The glasses are cleaned in ultrasonic bath with acetone, isopropanol and distilled water for 10 minutes in each step. Finally, the glasses are dipped into 10%

HF (Hydro fluoric acid) solution for 15 seconds and then cleaned with distilled water. Four different IDLs, SiN_x, SiO_2, ZnO and TiO_2, are deposited prior to a-Si deposition. SiN_x deposition is carried out by a PECVD system in which, decomposition of ammonia (NH_3) and silane (SiH_4) precursor gases with a ratio of 1:2 NH_3/SiH_4 is used. It is worth to mention that all of the used PECVD deposition gases (Linde and Air Liquide) are of 99.999% purity. The gas pressure is kept at $1.3x10^2$ Pa, and the substrate temperature (T_s) is kept at 200 °C. The final thickness of the SiN_x is 30 nm. SiO_2 is deposited by reactive sputtering technique (Vaksis NanoD) with a fused silica target (99.995% purity, Kurt-Lesker). The gas pressure is kept at 0.53 Pa and a ratio of Ar to O_2 is kept at 30. Substrate is not heated during the film deposition. The final thickness of the SiO_2 is 30 nm. TiO_2 layers are deposited by atomic layer deposition (ALD). At the system pressure of 30 Pa, the flow rate of the precursor N_2 is 20 sccm whereas the pressures of the precursors for O_2 and Ti are 50 Pa and 40 Pa, respectively. The substrate temperature is at the temperature of 130 °C; 550 ALD cycles are undergone. The cycles proceeded as follows: 15 ms for Ti precursor (Tetrakis(dimethylamido)titanium TDMAT, Sigma Aldrich 99.999% purty) injection, 15 s for purge; 15 ms for O_2 injection, 15 s for purge consecutively. The final thickness of the TiO_2 is 30 nm. After the buffer layer processes are accomplished, a-Si thin film is deposited onto each IDL. E-Beam evaporation is used for a-Si deposition. Before silicon evaporation, the base pressure of the chamber is $2.66x10^{-5}$ Pa and during the deposition the pressure is kept between $1x10^{-4}$ Pa and $6.6x10^{-5}$ Pa. The substrate temperature is kept constant at 250 °C during the evaporation process and e-beam current is varied between 100 mA and 115 mA in order to keep the deposition rate constant at 1 nm/s. Finally 650 nm of a-Si is deposited onto the each IDLs. Addition to previously prepared specimens, the sample of a-Si with ZnO layer is prepared as follows: ZnO layer is coated via ALD method once again. ADL is proceeded as 15 ms Zn precursor (Diethylzinc - DEZ, Sigma-Aldrich, deposition systems grade) injection pulse; 5 s purge with N_2; 15 ms pulse of H_2O during 15 s for purging consecutively 200 cycles are done at 200 °C in order to get a thickness of ∼35 nm ZnO layer. Over the layer of ZnO, a-Si layer of 550 nm is deposited by e-beam deposition.

3.3.2 Laser crystallization of specimens

In this work, a 1064 nm wavelength pulsed laser is employed. The duration of the pulses are measured as 200 ns via a fast Si photo detector. The value of the pulse duration is given as the full width at half maximum (FWHM) of the measured pulse in time. The average power of the irradiation at the surface of the samples, which had the IDLs of SiN_x, SiO_2, and TiO_2 with the a-Si film thickness of 650 nm, is 1.32 Watt and the scan speed (v_s) is set at a value of 114.4 mm/s so as to maintain the pulse overlap ratio at the maximum value of 97.6% (The corresponding pulse repetition frequency is 80 kHz). At this scan speed, LC processing of a 1 cm^2 area takes about 25 s. The effective laser focal spot diameter on the Si thin film is $\sim 40\mu$m so that the peak fluence of the laser on the thin films corresponded to a value of 2.63 J/cm^2 and the pulse energy is 16.5 μJ. For the sample with the IDL of ZnO layer is scanned with a different output power. The irradiated average power on this sample is 1.53 Watt. The other scan parameters are the same with the others. The corresponding peak fluence is 3.04 J/cm^2 and the pulse energy is 19.1 μJ. The reason of this fluence change is that the deposited (extinct) energy through the a-Si layer changes with the thickness of the layer. For the thickness of 650 nm a-Si, the extinct energy percentage is 33% of the irradiated power on the surface, whereas the extinct energy percentage for the thickness of 550 nm a-Si is about 29% of that irradiation. In order to fix the value of the transferred energy to the a-Si surface per pulse, the fluence is increased to the value of 3.04 J/cm^2 for the specimens of ZnO IDL. The laser focus is scanned on the samples in a pattern of concentric rings (Figure 3.18). In addition to the overlap of successive pulses, the concentric rings also overlap with increasing diameter.

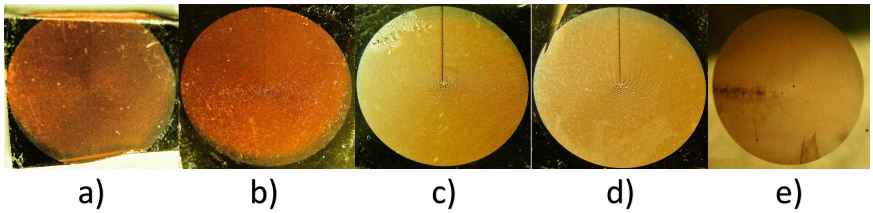

Figure 3.18: LC processed samples with different IDLs; a) No Buffer Layer, b) IDL: SiN_x , c) IDL: SiO_2 , d) IDL: TiO_2, e) IDL: ZnO. The LC processed regions have a diameter of 12 mm.

In order to make statistics with experimental data, four more samples are formed for

each type of IDLS in addition to the ones shown in Figure 3.18, since the fabrication is prone to variations due to uncertainties in the leveling of the sample substrates, the jitter in the laser system, etc... All samples are analyzed using Raman spectroscopy in order to check the consistency of the laser process. In Figure 3.18 the centers of the scanned regions exhibit some basket base shapes. Those stem from the limits of the galvo-mechanical scanning system of the laser marker. In order to ensure uniformity of the measurements, the Raman spectra are acquired from the outer regions of the formed disks in order to avoid parasitic contribution from the amorphous areas which could not be scanned continuously close to the disk center.

3.3.3 Raman analyses of laser crystallized a-Si films

In order to perform an analysis of the crystallinity, Raman spectroscopy is used with a CW solid state laser at a wavelength of 532 nm as the excitation source. For each sample, the bulk crystalline Si (c-Si) Raman shift frequency of the phonon peak center around 521 cm^{-1} and its Full Width at Half Maximum (FWHM) of each peak are measured via a 50 cm monochromator ICCD based fiber coupled Raman spectroscopy system (Horiba-JobinYvon iHR550) . For the sake of consistency, the Raman peak position of each sample is calibrated with respect to the peak position value of the reference c-Si which is measured at 521 cm^{-1} with a FWHM of $\sim$3.8 cm^{-1} (see Figure 3.19). The intensities of all Raman signals are normalized in order to make comparative deductions for specimens easily. In order to minimize instrumental errors, the spectra belonging to the reference c-Si sample are acquired before and after measurements of each sample set. Having determined the Raman peak frequencies and the FWHM values for the same type of specimens, the averages of corresponding values are calculated (see Figure 3.20).

The Raman peak position of the specimen without buffer layer exhibits a redshift more than other specimens. This can be attributed to the mismatch of the thermal conductivities and the thermal expansion coefficients of the glass substrate and laser induced μc-Si; furthermore, the crystalline grain sizes can also be compared by examining Figure 3.20 qualitatively. The narrowed Raman peaks for the ZnO and TiO_2 samples address a better crystallinity in the processed regions than that of the other

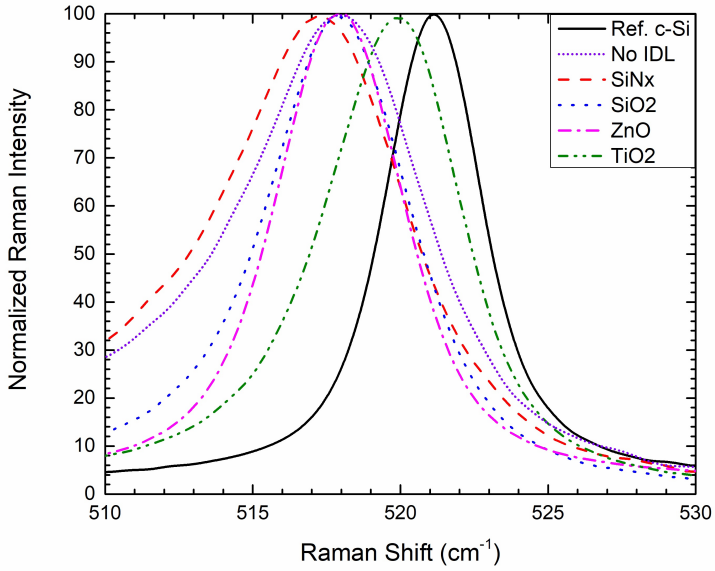

Figure 3.19: Si Raman spectra of the IDL samples

specimens. In Figure 3.20, it can be seen that the tensile stress decreases for the specimens with SiO_2, ZnO and TiO_2 buffer layers. The variation in the values of TiO_2 restrain us to compare it with the values of SiO_2 and ZnO. It can be deduced the specimens with SiO_2, ZnO and TiO_2 buffer layers are promising for achieving good crystallinity by laser induction.

Table 3.6: Thermal conductivities of IDLs

Material Type	Thermal Conductivity ($Wm^{-1}K^{-1}$)	Mean Grain Size (μm)	Raman Peak Position (cm^{-1})
Glass	1.16	0.24	517.8
SiN_x	20 - 70	0.27	517.5
SiO_2	1.14 - 1.31	0.55	518.0
ZnO	4 (at 1000 °C) - 37	1.01	518.6
TiO_2	6.5 - 8.5	0.41	519.6

The thermal conductivity of SiN_x, changes between the values of 20-70 $Wm^{-1}K^{-1}$ [68], is higher than that of SiO_2 and TiO_2. So, that lets the pulse energy to be transferred through the glass substrate without making up a significant amount of nucleation at the a-Si layer. Nevertheless, the layers of SiO_2 and TiO_2 maintain the nucleation at the a-Si layer since they have higher thermal conductivities changes between 1.14-1.31 $Wm^{-1}K^{-1}$ [69] and 6.5-8.5 $Wm^{-1}K^{-1}$ [70], respectively) compared to that of

SiN_x and ZnO. Thermal conductivity of ZnO is about 37 $Wm^{-1}K^{-1}$ layers; however, the thermal conductivity of ZnO layer is shown that it decreases below a value of 4 $Wm^{-1}K^{-1}$ at a temperature of 1000 °C with increasing temperature of ZnO nano-scale structures, and the thermal conductivity depends on temperature strongly [71]. In these regards, an increase in thermal conductivity does not maintain the heat accumulation on the films and the nucleation of crystallization does not occur efficiently (see Table 3.6).

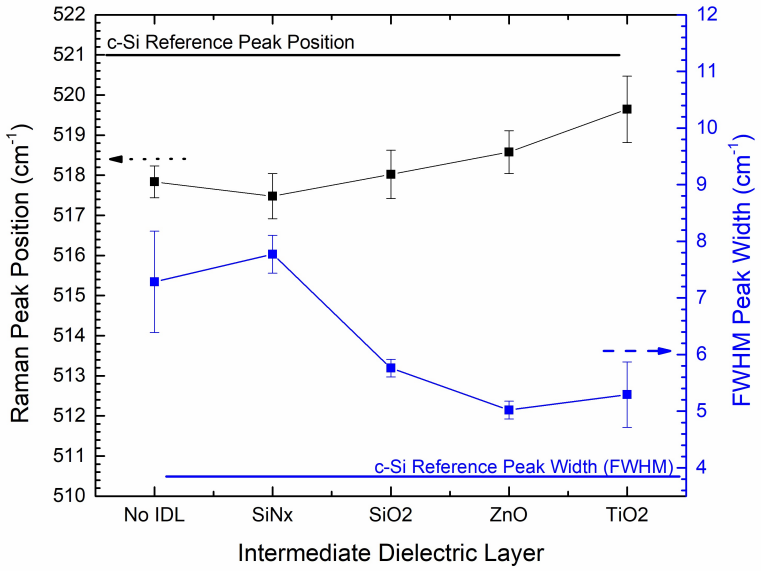

Figure 3.20: Quantitative comparison of Raman spectra

3.3.4 SEM images of laser crystallized a-Si films

Scanning Electron Microscope (SEM) analyses of the specimens, which correspond the Raman analyses mentioned previously, are done. The surface structures are shown in Figure 3.21, below. The inset images show the optical microscope images of the samples where the Raman signals are acquired.

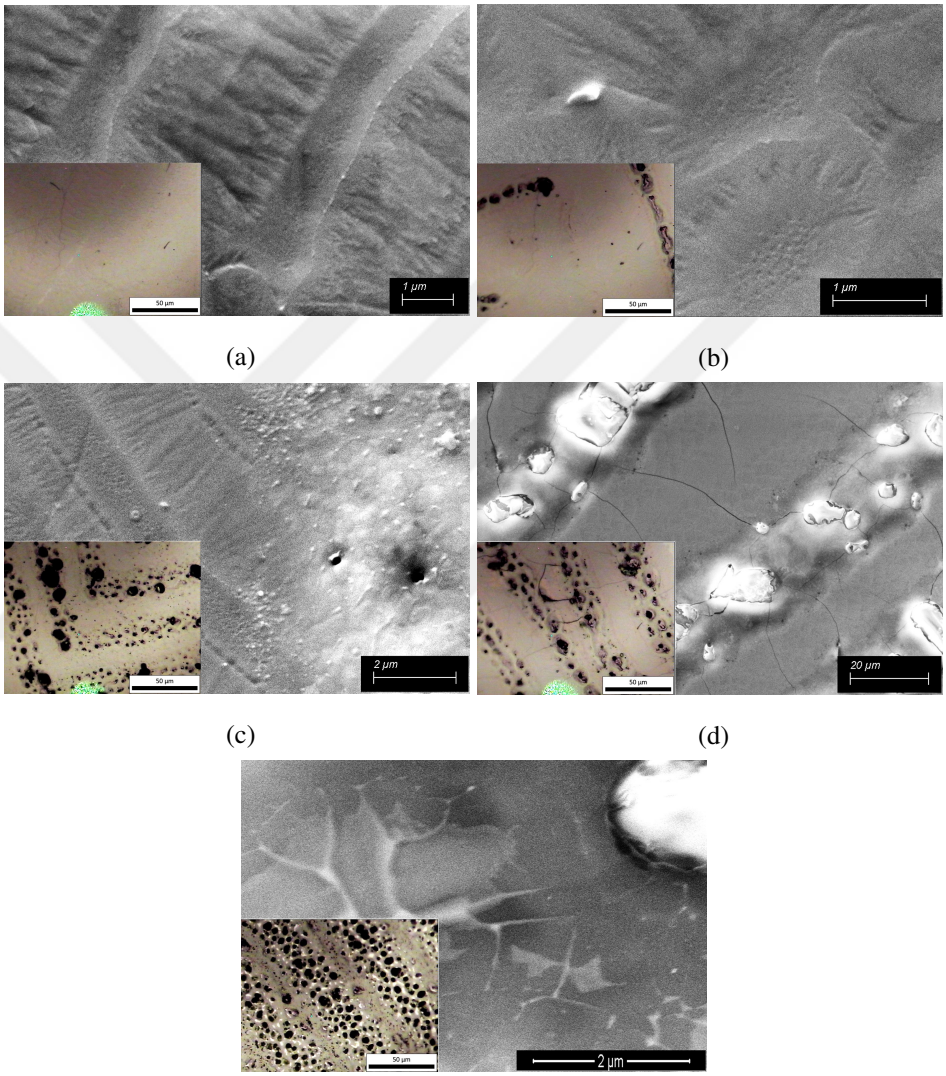

(a) (b) (c) (d) (e)

Figure 3.21: SEM images of laser crystallized samples with a) no buffer layer; b) the thickness of 30 nm SiN_x ; c) the thickness of 30 nm SiO_2 ; d) the thickness of 30 nm TiO_2 ; e) the thickness of 35 nm ZnO.

By examining the image above, it can be seen where some defect and crack formations occur.

3.3.5 EBSD analyses of laser crystallized a-Si films

EBSD images are acquired after the samples are polished and they are randomly chosen among the laser processed sample sets.

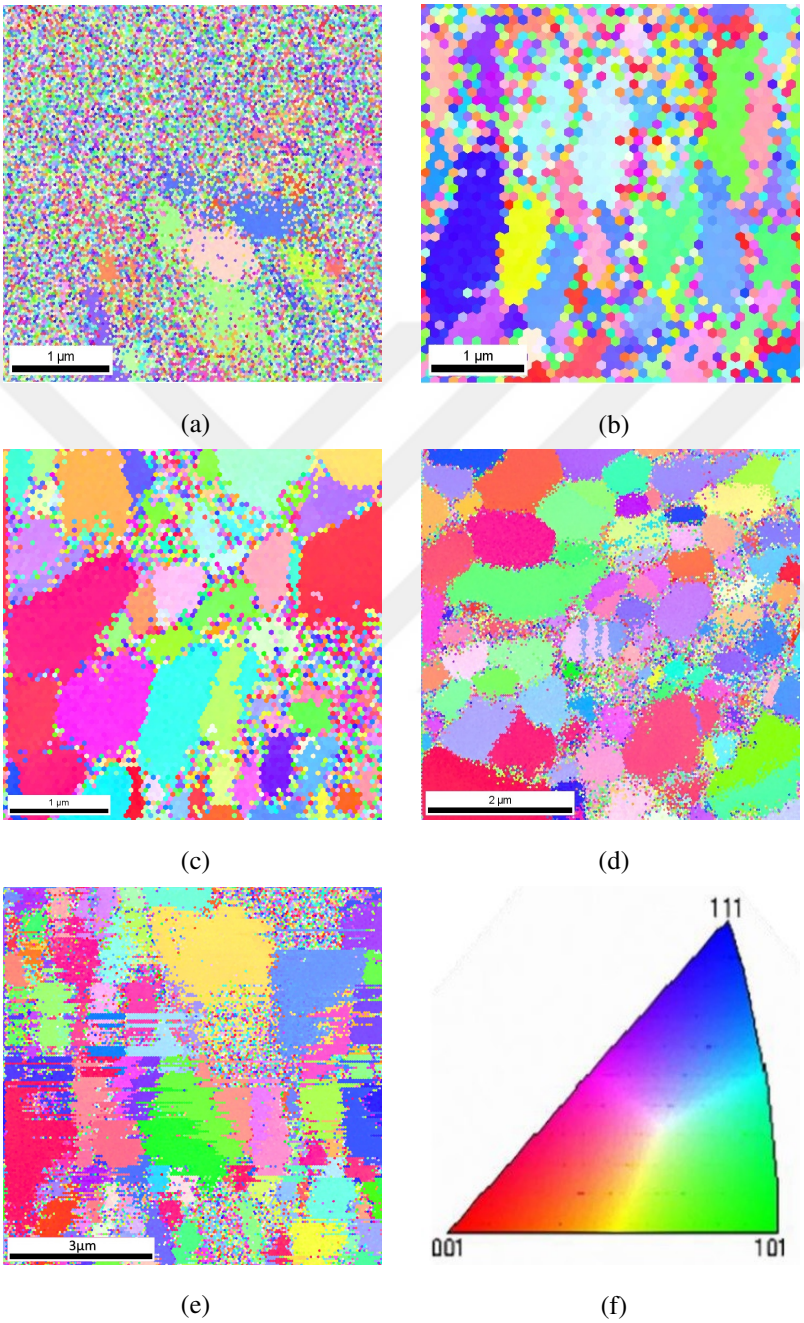

Figure 3.22: EBSD images of LC specimens with a) no buffer layer; b) the thickness of 30 nm SiN_x ; c) the thickness of 30 nm SiO_2 ; d) the thickness of 30 nm TiO_2 ; e) the thickness of 35 nm ZnO; f) color code of crystal orientations

As seen in Figure 3.22, there exists a variation in the grain sizes. The grain size can exceed 2 μm in length for the samples with TiO_2 and ZnO buffer layers. Augmentation of the grain sizes can be predicted from the redshift of the Raman peaks. An inverse correlation between the grain size and the redshift of the Raman peak is observed as in Reference [60]. The decreasing grain sizes address an increase in the tensile stress over the domains, in which this results in redshift of Transverse Optical (TO) modes in the one-phonon Raman peak [56, 57, 59, 60]. The biaxial tensile strain with an in-plane stress can be expressed as the following [57, 58];

$$\Delta\omega = -4.0\sigma \quad , \tag{3.1}$$

where $\Delta\omega$ is the redshift (in the unit of cm^{-1}) in the Raman peak position of μc-Si with respect to the reference Raman peak position of c-Si (at about 521 cm^{-1} for this work), and the tensile stress is given as σ in GPa unit. In addition, the stress over the grains can be compressive as well, i.e., σ can be negative which results in a blueshift of Raman peak position [56]. Accordingly, the tensile stress on the crystal domains takes values between 0.1 and 0.9 GPa.

In laser induced crystallization process of thin a-Si films, SiO_2, ZnO and TiO_2 buffer layers between glass substrate and a-Si exhibit better performance than SiNx buffer layer and no buffer layer in terms of crystallinity quality. This is because these layers do not facilitate crystal nucleation as dense as the latter cases. Not only are the crystal grains increased in size with SiO_2, ZnO and TiO_2 buffer layers but also the crystallinity of LC μc-Si is improved especially for the IDLs of ZnO and TiO_2 . Consequently, the tensile stress between the grains could be reduced to some extent with SiO_2, ZnO and TiO_2 layers. This work provides a quantitative comparison of the qualities of laser induced crystallization products with and without several buffer layers.

3.3.6 Secondary ion mass spectroscopy analyses of laser crystallized a-Si films

LC i-a-Si layers over the different intermediate layers are analyzed via TOF-SIMS. Analyses of the specimens are shown in Figure 3.23-3.27. On all plots of Figure 3.23-3.27, all positive ions reach to saturation levels with considerable noisy values that can been seen at the right side of the plots. The measured thicknesses of the crystallized Si layers and the buffer layers allow the scraping time to be scaled to a proximate depth of the crater. The known ingredients in the substrate, which it is made of glass, reached a noisy saturation level and did not change much till the end of the scraping process. The beginning of this saturation level can be labeled as the overall thicknesses of the films roughly. The plots on a single graph can be compared consistently; however, the graphs of the different samples are not comparable with each other. The counts of the ions and the parameters of the different sample analyses vary from sample to sample.

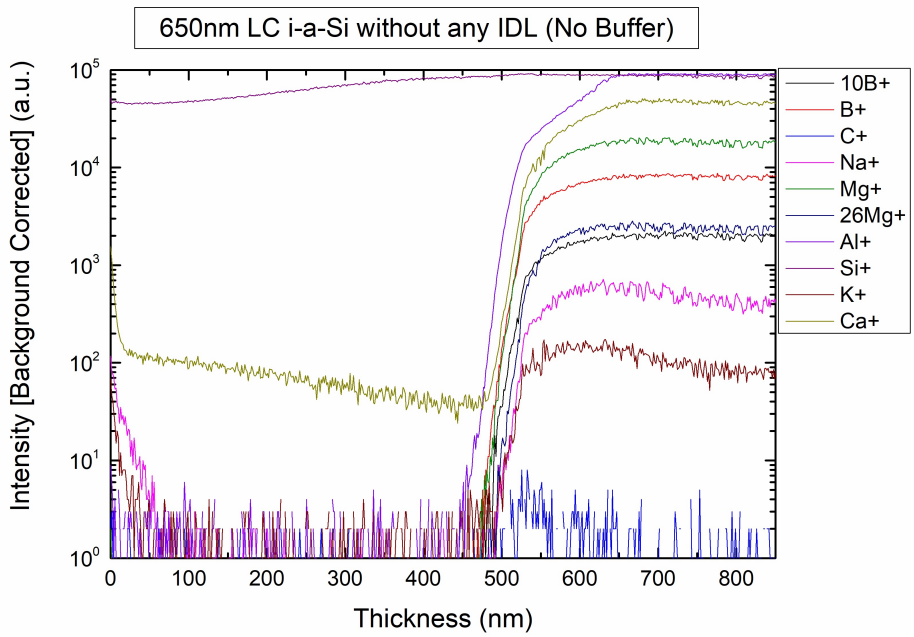

Figure 3.23: SIMS analysis of 650 nm LC Si layer without an IDL

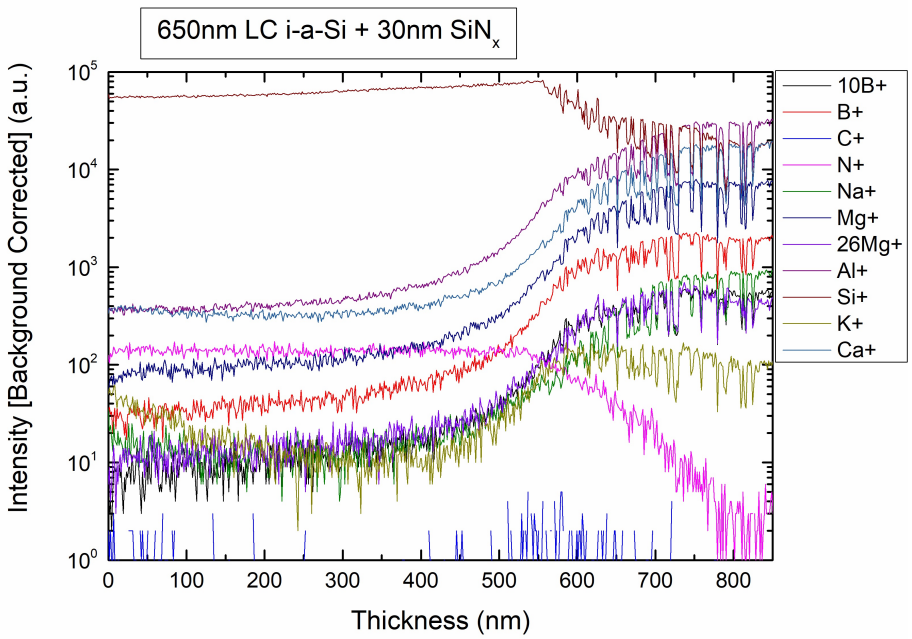

Figure 3.24: SIMS analysis of 650 nm LC Si layer with 30 nm of SiN_x

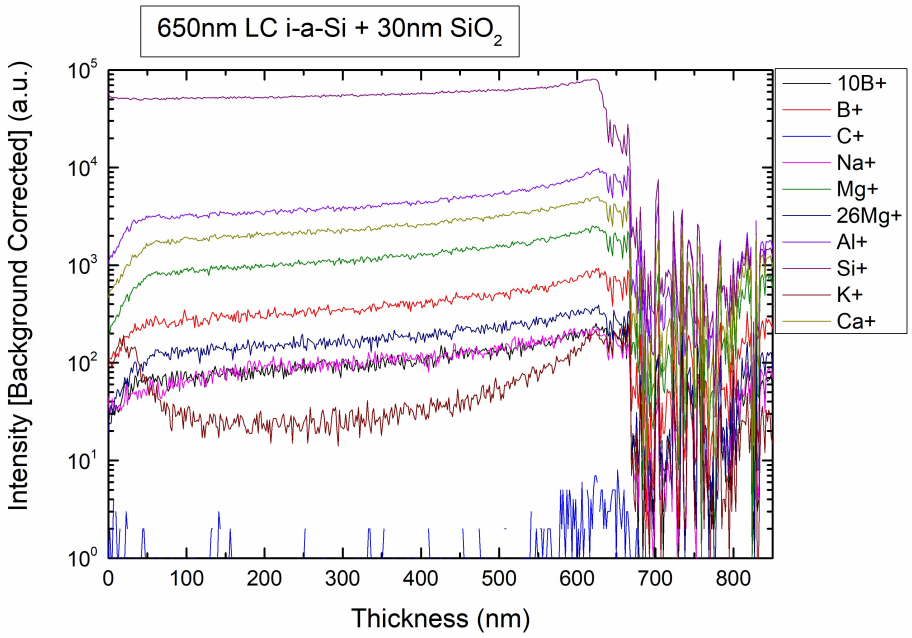

Figure 3.25: SIMS analysis of 650 nm LC Si layer with 30 nm of SiO_2

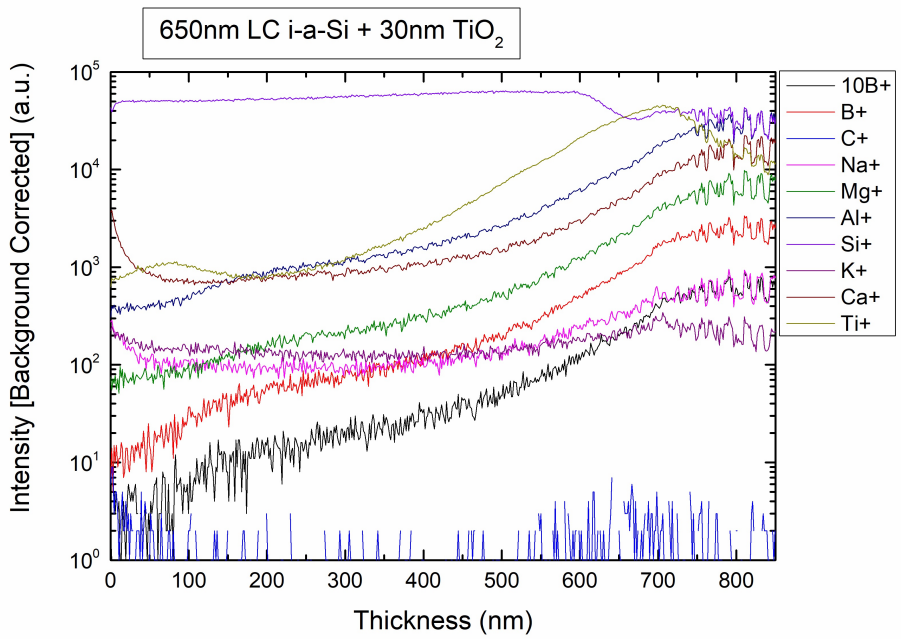

Figure 3.26: SIMS analysis of 650 nm LC Si layer with 30 nm of TiO_2

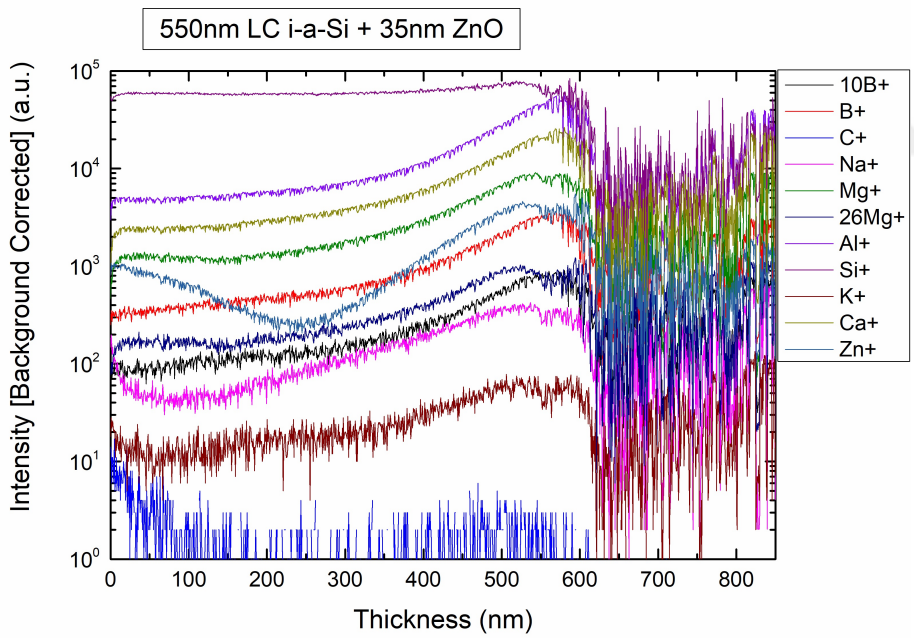

Figure 3.27: SIMS analysis of 550 nm LC Si layer with 35 nm of ZnO

The results show that the diffusion of positive ions occurs from the glass substrate and the buffer layers to the LC-Si regions in order of 10^3 with respect to the counts of Si^+ which are on the order of 10^5.

3.3.7 Transmission and reflection analyses of laser crystallized a-Si films

The 400-1100 nm range spectrum analyses of the specimens with diameters of 12 mm are investigated. The spectrum measurements are done in order to obtain the total and/or diffuse transmission and reflection spectra and to determine the absorption graphs. The samples are placed so that the incident and reflected beams would be at an angle of 8 degrees. For sake of consistency, the transmission spectra of the samples are also measured at that angle to calculate the absorption values. The spectra of total and diffused transmission-reflection are obtained by means of an integrating sphere mounted before the entrance of a monochromator. The roughness over the sample surface due to the laser process did not produce specular reflections. The use of a integrating sphere, it would be ease to compare the reflection spectra; however, the transmission spectrum still has some flaws due to that rough surface where some of the incident light gets reflected before entering the integrating sphere. The positions of the samples are denoted in Figure 3.28.

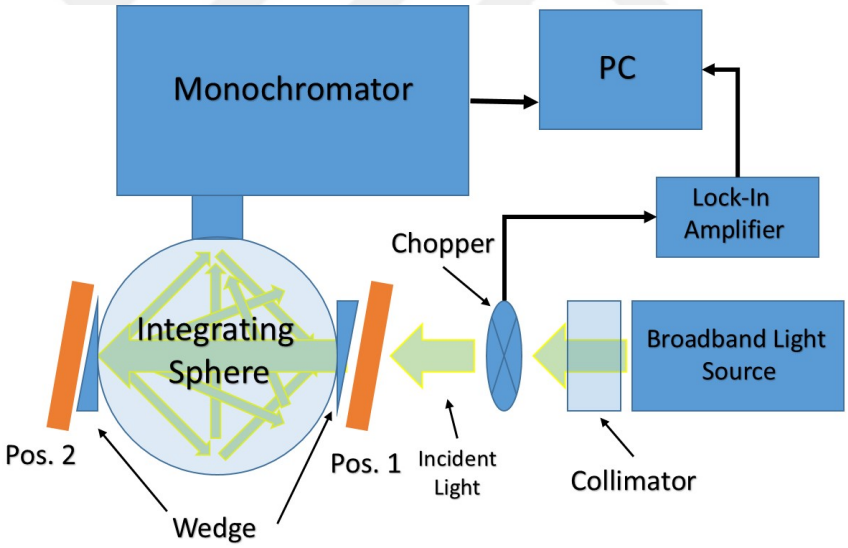

Figure 3.28: Scheme of transmission-reflection spectrum measurement

During the transmission measurements, the samples are placed in Position 1; otherwise, the position 2 is used to obtain the reflection measurements. A mechanical chopper is used with a lock-in amplifier in order to eliminate noise by modulating the incident light and the data is acquired in correlation with the modulated incident beam. While measuring the diffuse transmission and reflection spectra, main trans-

mitted or specular reflected beams are allowed to exit the integrating sphere so as to eliminate the contribution of the main beams to the detected signals. In Figures 3.29 - 3.32, the total transmission reflection and the diffuse transmission reflection measurements are shown. In all spectra graphs, the plots are labeled with respect to the buffer layer types.

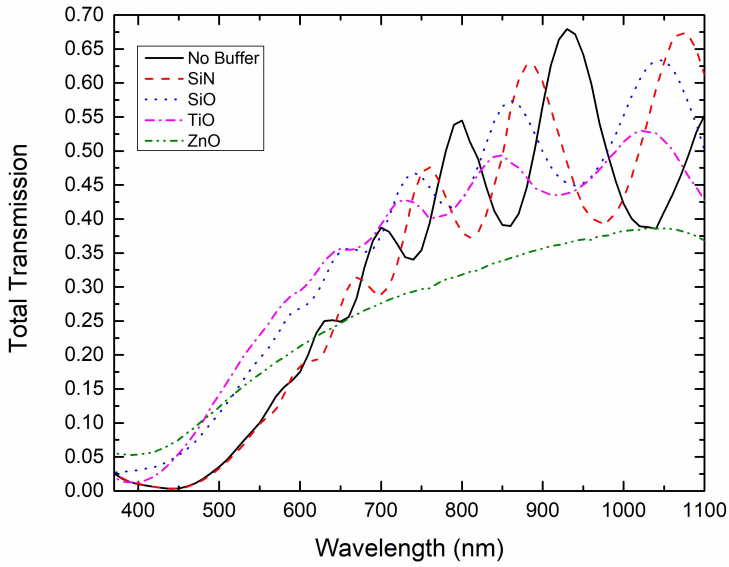

Figure 3.29: Total transmission spectra

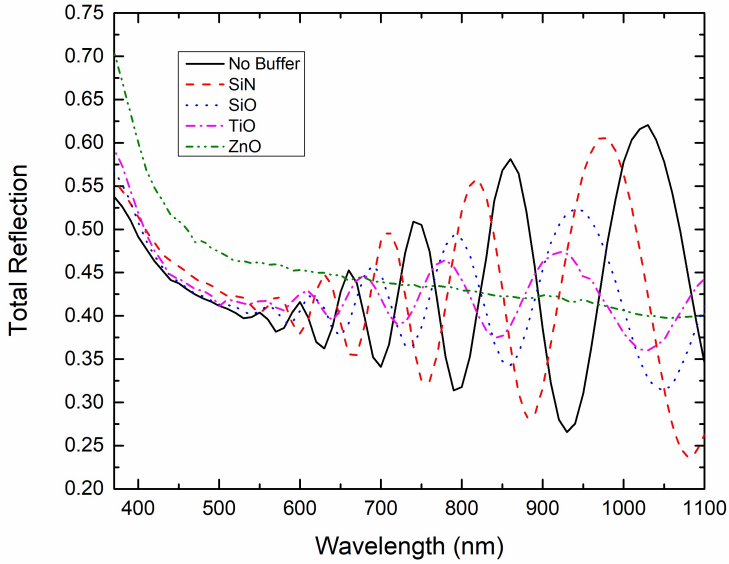

Figure 3.30: Total reflection spectra

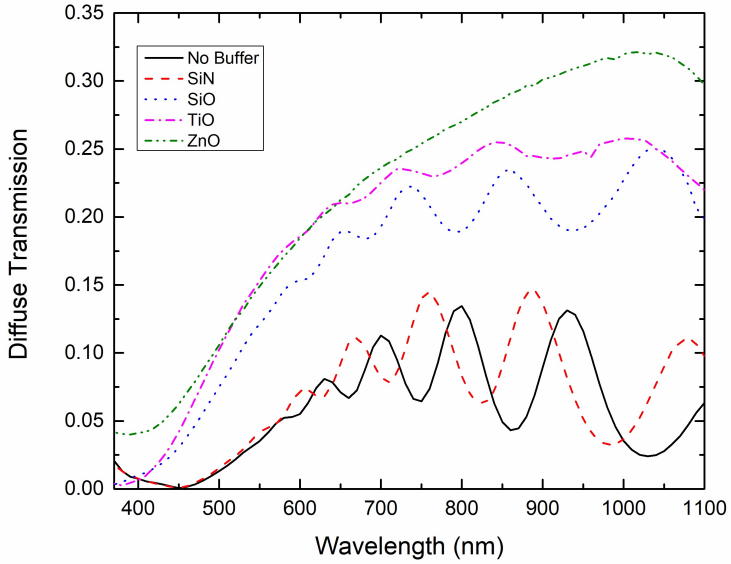

Figure 3.31: Diffuse transmission spectra

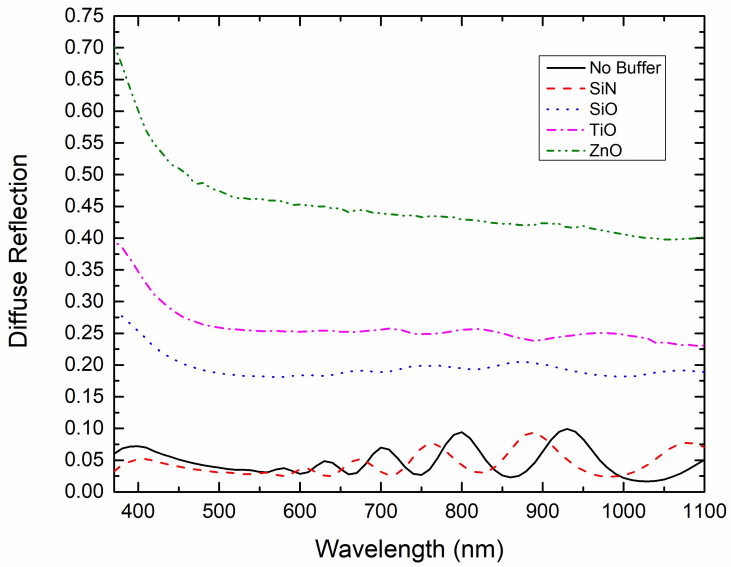

Figure 3.32: Diffuse reflection spectra

The ratios of the diffused spectra to the total spectra give percentage of haze effect which is produced by the films. The surface roughness can also be inferred from this haze by means of a proper model. However, this model is not included in this dissertation. On the contrary, the surface structures are examined by AFM in the

following sections in detail. The roughness of the film surfaces are calculated from those direct measurements. It is worth to mention that the haze effect is minimum for the samples with no IDL (No Buffer) and SiN_x.

The thicknesses of the films and the variation in the thicknesses and the refractive indices can be analyzed by examining the successive peaks at the total transmission and reflection spectra.

The absorption of the samples are calculated as A = 1-T-R, where A is the absorption, T is the total transmission and R is the total reflection. The absorption curves are shown in Figure 3.33.

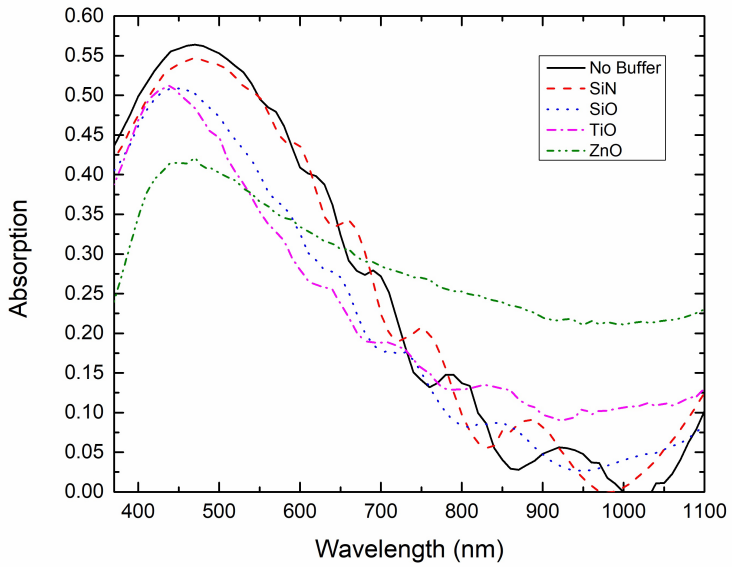

Figure 3.33: Absorption spectra

The absorption coefficients of the films can be deduced by analyzing the absorption curves easily. Fortunately, the absorption of the a-Si films are examined in Section 4.2. The absorption curves are given as a guide in order to compare with the direct measurement of the Si absorption with respect to the thicknesses of the films. The absorption of the sample, which has ZnO IDL exhibits lower than the others. This can be attributed to that the samle, with ZnO IDL, has the less film thick than the other films besides that sample also has less thick Si film over it.

CHAPTER 4

INFLUENCES OF SI FILM THICKNESS AND OVERLAP OF LASER PULSES ON LASER CRYSTALLIZATION

4.1 Improvements of line focus scan

In order to construct the line focus scanning system. 50 Watt pulsed Flast-NanoMARK 50 W laser marking system is employed. The system optics are placed with respect to the dimensions that are given in Figure 4.1.

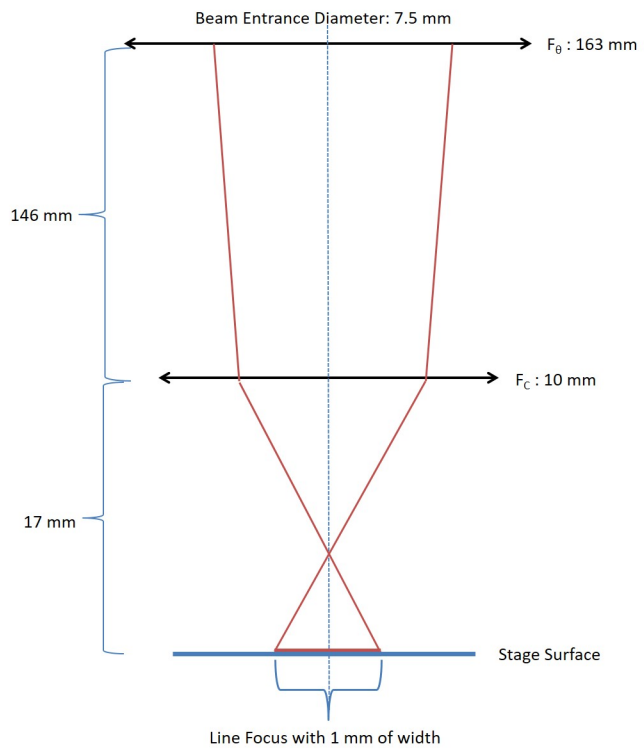

Figure 4.1: Line focus system design

If ray optics is considered, the line width of the focus on surfaces of samples will be

calculated as 1 mm of width and the cylindrical lens won't affect the focus diameter in the parallel direction of the scan direction. The specification of the cylindrical lens, which is employed in this experiment, as follows: f_0 is 10 mm and its dimensions are 10 mm x 20 mm. In order to avoid optical aberrations the curved surface of the cylindrical lens faces the incident beam emerging from f-theta lens.

The photograph image of laser scanning system is shown in Figure 4.2. The cylindrical lens is placed with an kinematic rectangular optic (KRO) mount in between the target surface and the f-theta lens. The KRO mount is held by magnetic post-holder and is placed directly on the optic table.

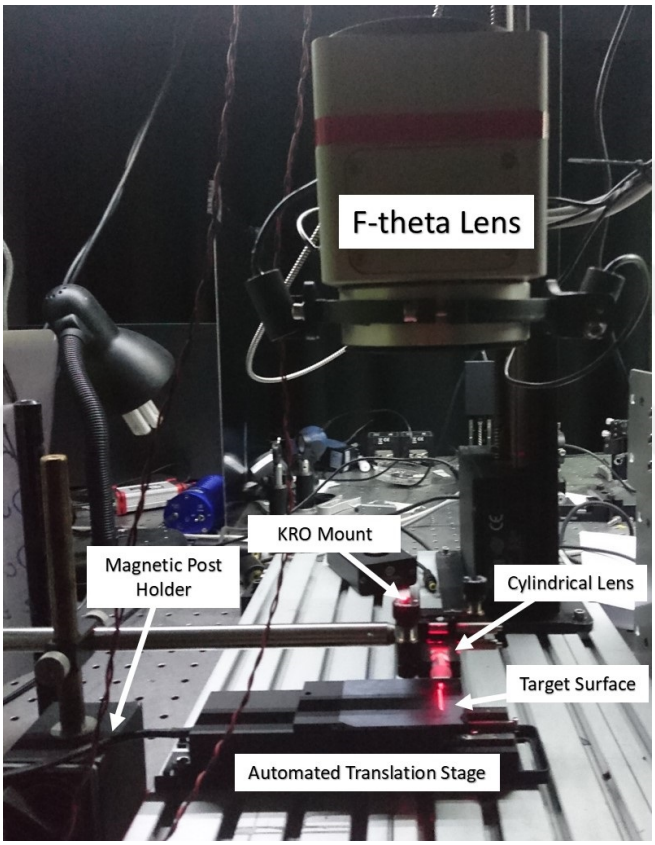

Figure 4.2: Photograph image of the line focus scanning system

In Figure 4.3, the scan direction of the line focus is virtualized by a red laser beam on the target surface. The scan direction is along the red line and the extension of the 1064 nm laser in width can reach 1 mm. The maximum length of the line focus scan can reach up to 18 mm. This limit is determined by the length of the cylindrical lens and aberrations caused by the incident angle on the cylindrical lens.

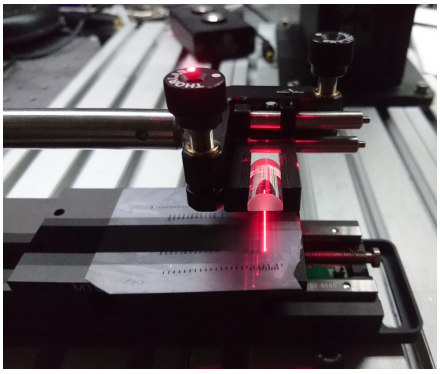

Figure 4.3: Virtualization of a line focus scan

The calculated maximum dimensions of the focus are 45 μm x 1000 μm. The focus is expected to be in elliptical shape since the incident beam upon the cylindrical lens has a Gaussian beam profile. The crystallized trace of the pulses without any overlap are seen in Figure 4.4.

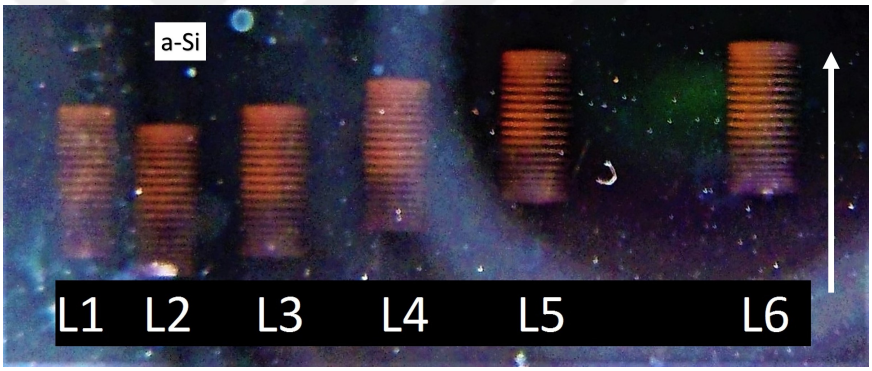

Figure 4.4: Line focus scans on a-Si films with a thickness of 1 μm

In Figure 4.4 the scan direction is shown by a white arrow and the a-Si region which is a dark area is designated as "a-Si". The a-Si film is deposited on a substrate of Schott AF32 Eco 1.1 mm glass. Scan numbers are labeled as "L #" in Figure 4.4. The laser scan parameters are given in Table 4.1. All lines are scanned with the speed of scan (v_s) of 3708 mm/s. The effective fluence per pulse is calculated over the line focus dimensions of 45 μm x 650 μm. The reason of use of these values is the measured dimensions by means of the optical microscope correspond to those.

The Raman signals of the three regions, i-a-Si, L1 and the Ref. c-Si are shown in Figure 4.5. (Note that "L1" is denoted as "L1 LC-Si", i.e., "LC-Si" is "Laser Crystallized

Table 4.1: Laser parameters of the line focus scan

L #	Av. Power (W)	Pulse Energy (μJ)	Effective Fluence (J/cm^2)
1	12.5	412	1.4
2	15.5	515	1.8
3	18.6	619	2.1
4	21.6	720	2.5
5	24.6	820	2.8
6	27.5	916	3.1

Silicon Film".)

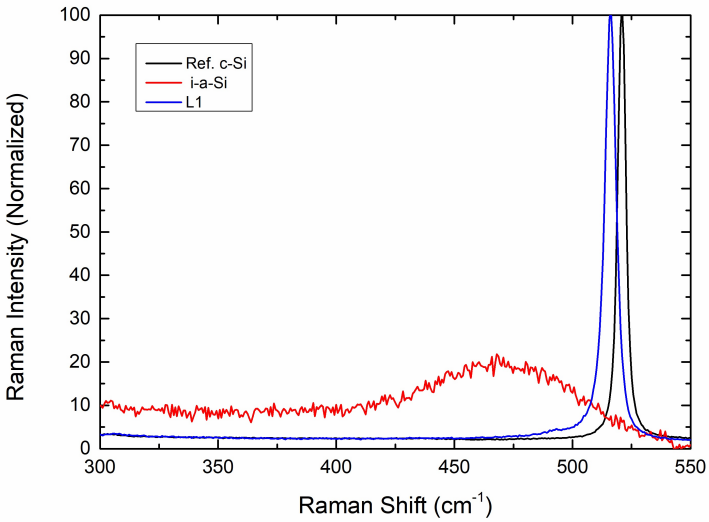

Figure 4.5: Raman spectra of i-a-Si, L1 and Ref. c-Si

The Raman signals and Raman analyses of the six lines are shown in Figure 4.6 and Figure 4.7, respectively.

The main trend in crystallization is increasing fluence makes the crystalline regions get closer values to that of the reference bulk c-Si. This correlation has already appeared in the previous sections.

The microscope images of the line focus scanned regions are also captured. The embodiment of the crystallized surfaces are shown in Figures 4.8a - 4.8f consecutively. Note that the scan direction is vertically applied with respect to the page.

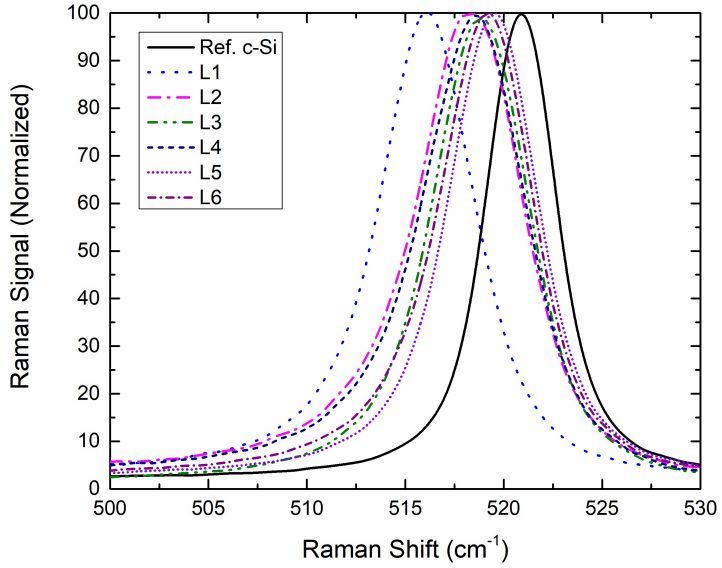

Figure 4.6: Raman spectra of the line focus Scan trails

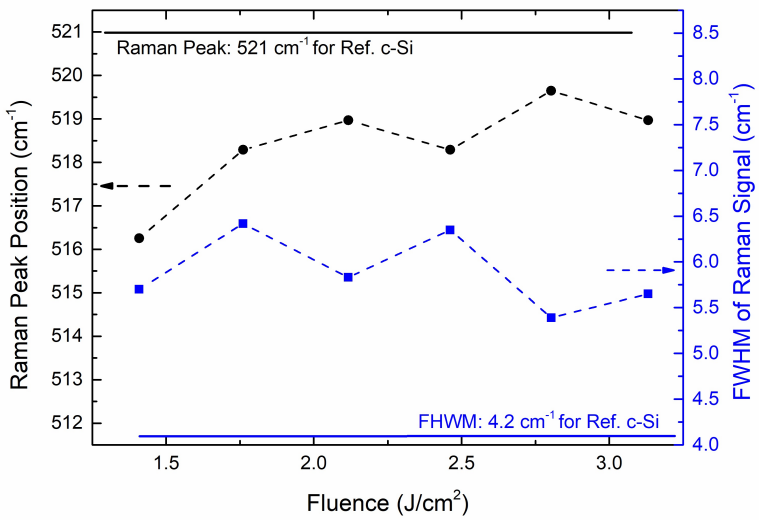

Figure 4.7: Si Raman peak analysis of the line focus scans

The automated translation stage allows to control the location of the line scan and the scanned lines can be made overlapped with each other as well. The overlap ratio of the lines are depicted in Figure 4.9. The blue regions show the single line focus pulses. Line overlap percentage is calculated by dividing LO to W, multiplied by 100, and from now on it is going to denotes as "Q_{LO}" factor.

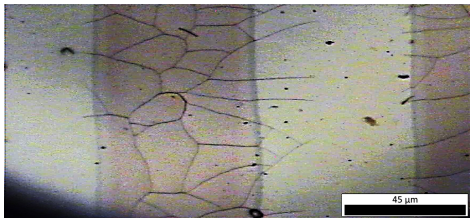

(a) Line scan: L1

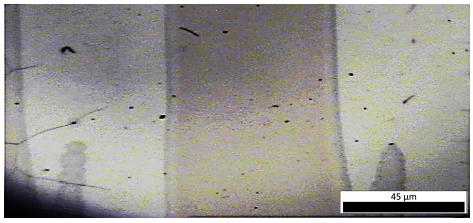

(b) Line scan: L2

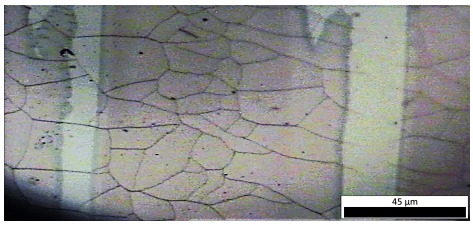

(c) Line scan: L3

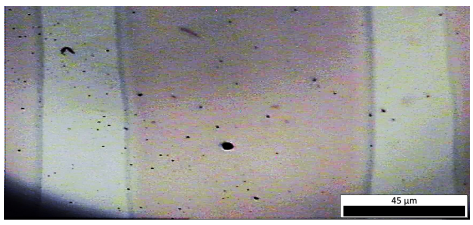

(d) Line scan: L4

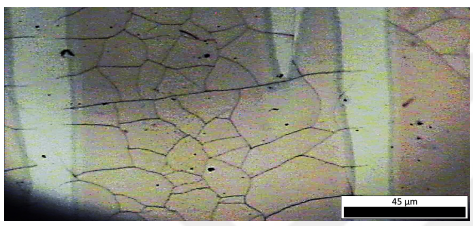

(e) Line scan: L5

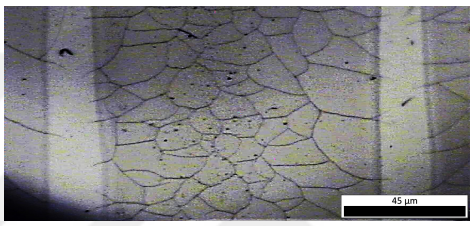

(f) Line scan: L6

Figure 4.8: Optical image of the line scans

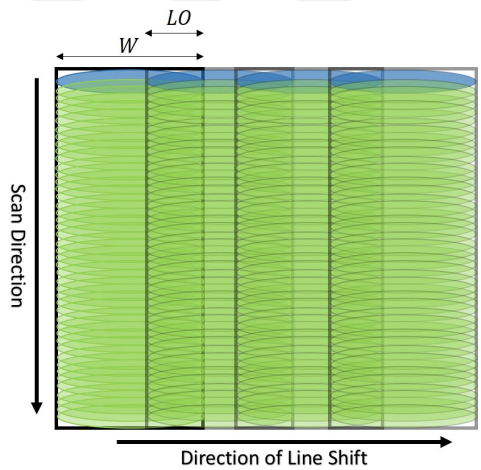

Figure 4.9: Diagram of line shifting; W: Line width and LO: Overlapped region of the lines

Before moving on the next section, the real improvement in crystallinity of laser processed regions which are developed by means of the line focus scan should be mentioned objectively. Figure 4.10 exhibits 6 lines of laser crystallized 950 nm a-Si film side by side.

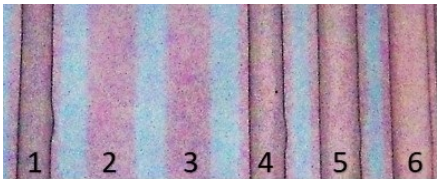

Figure 4.10: Laser crystallized lines of 950 nm a-Si Film. The numerated lines are scanned via the line focus optics.

The laser scan parameters are 99.5% of pulse overlap with the pulse dimensions of 45 μm x 800 μm with a flattened elliptical shape and the scan speed is 23 mm/s (see Table 4.2 for the fluence values).

Table 4.2: Laser average power and effective fluence values for laser crystallized lines of 950 nm a-Si Film

L #	Av. Power (W)	Effective Fluence (J/cm^2)
1	17	0.47
2	16	0.44
3	15	0.42
4	18	0.50
5	20	0.56
6	23	0.64

The microscope image of each line, besides the analysis of Raman signals given in Figure 4.11 in detail, is done (see Figures 4.12a - 4.12f).

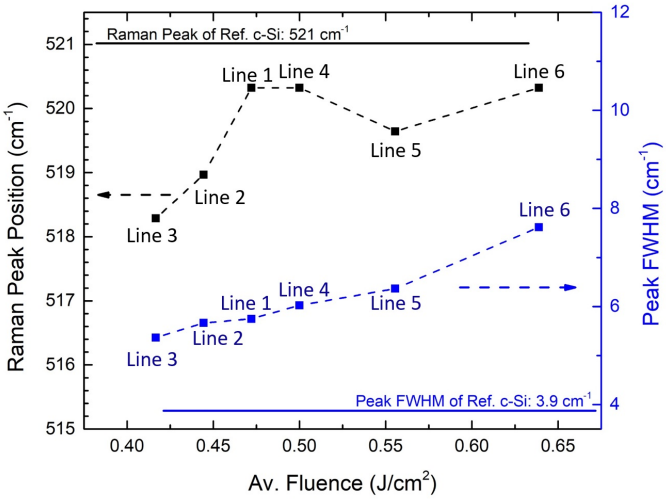

Figure 4.11: Analyses of Raman spectra

The green spot on each Figure 4.12a - 4.12f shows where the Raman signals are collected.

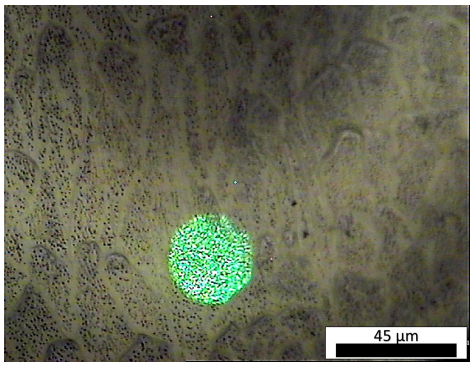

(a) Line 1

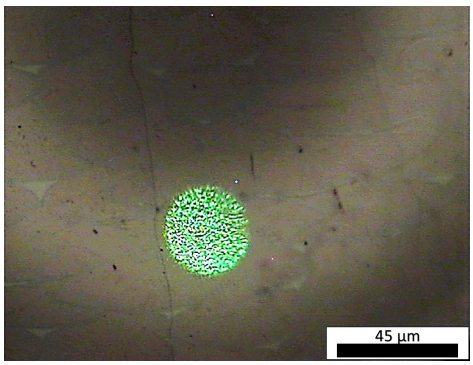

(b) Line 2

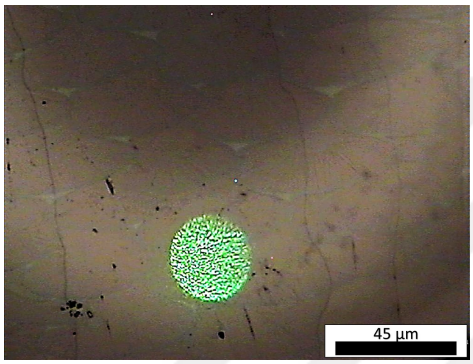

(c) Line 3

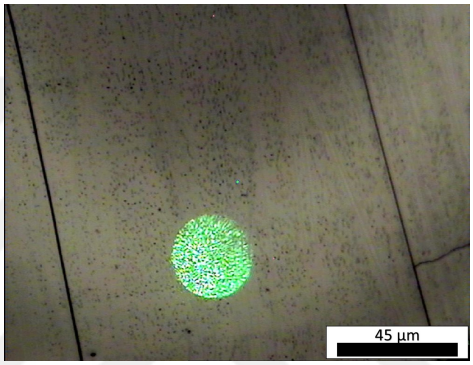

(d) Line 4

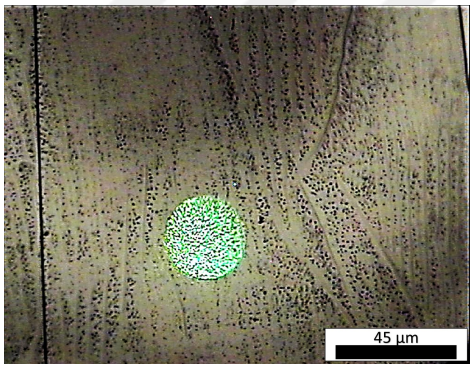

(e) Line 5

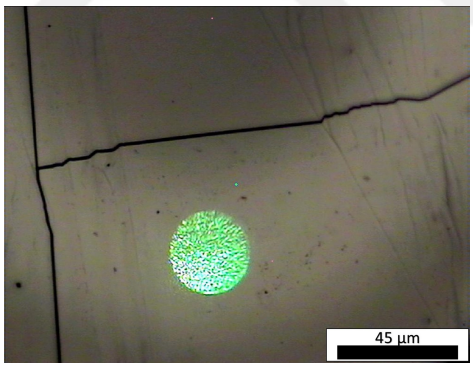

(f) Line 6

Figure 4.12: Optical microscope images of Line 1 - 6

The SEM image and EBSD image of each line is given side by side in Figure 4.13 - 4.18.

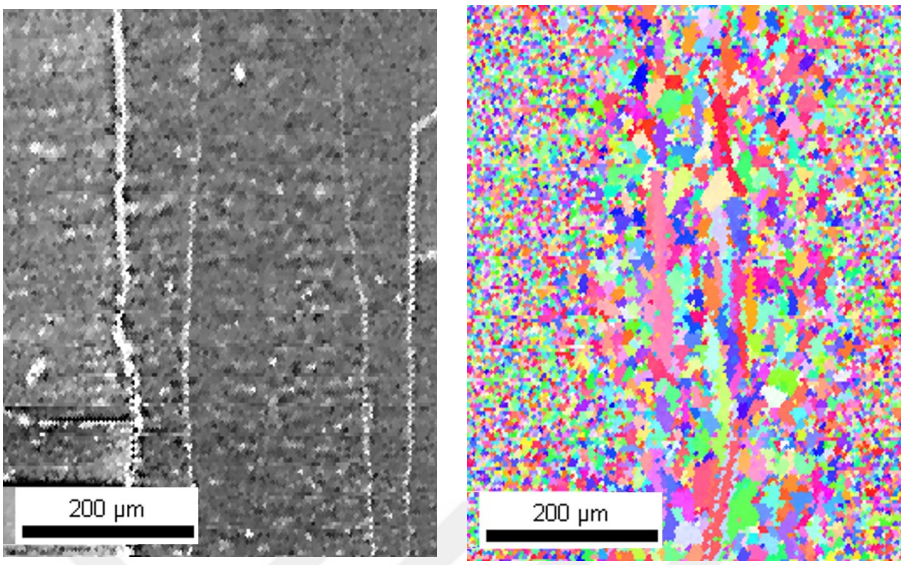

(a) (b)

Figure 4.13: a) SEM and b) EBSD images of Line 1

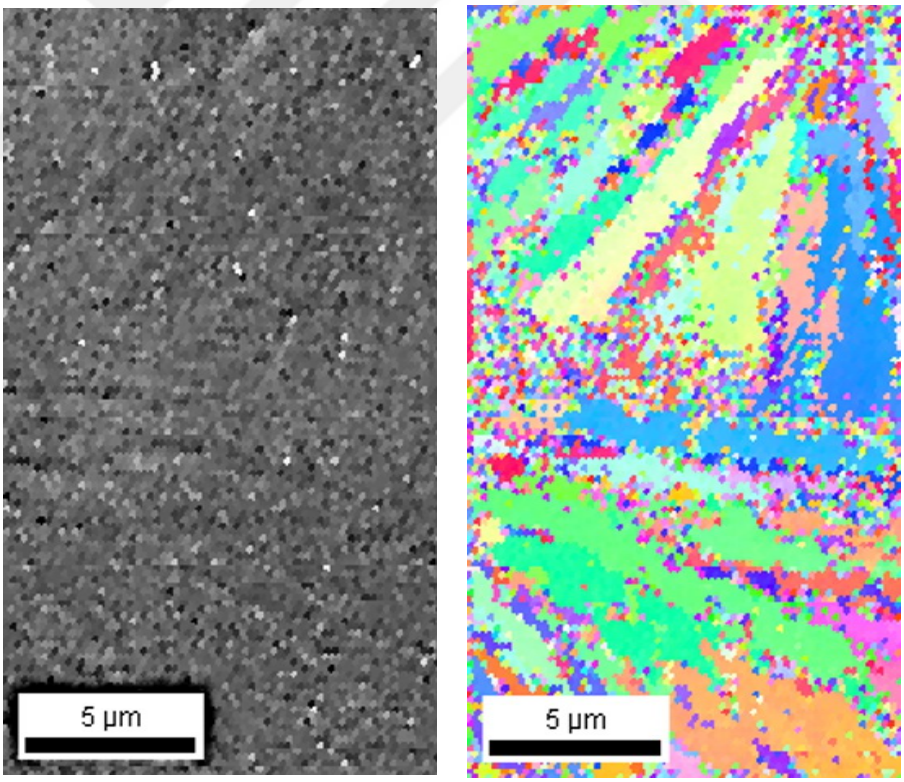

(a) (b)

Figure 4.14: a) SEM and b) EBSD images of Line 2

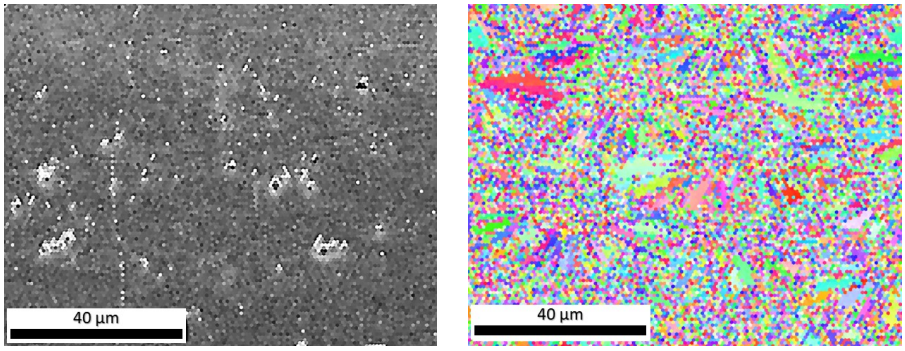

(a) (b)

Figure 4.15: a) SEM and b) EBSD images of Line 3

It is seen from the EBSD images that the grain sizes are increased up to millimeter range by means of applying more fluence with more overlapping line focus pulses (see Figure 4.18).

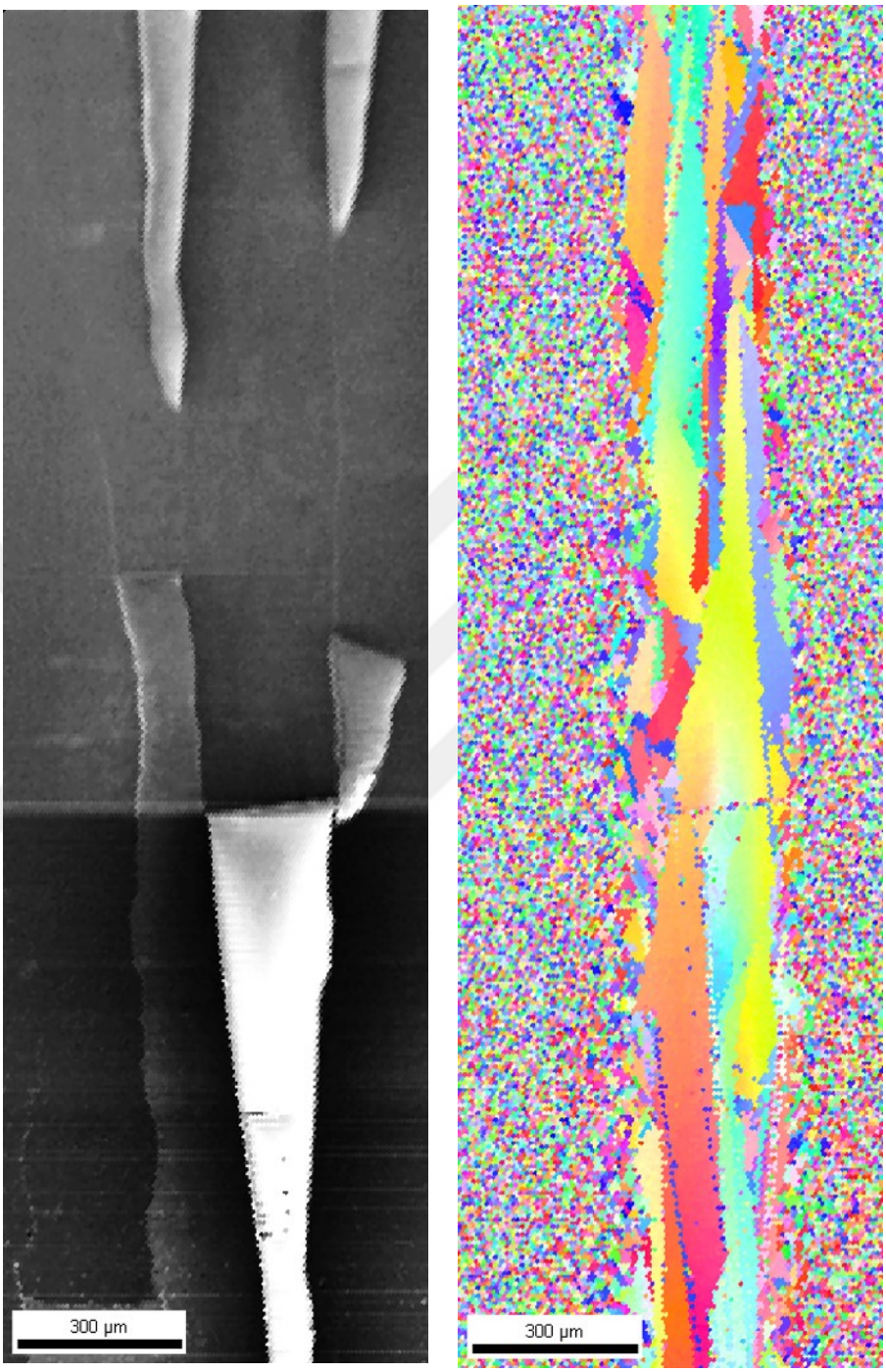

(a) (b)

Figure 4.16: a) SEM and b) EBSD images of Line 4

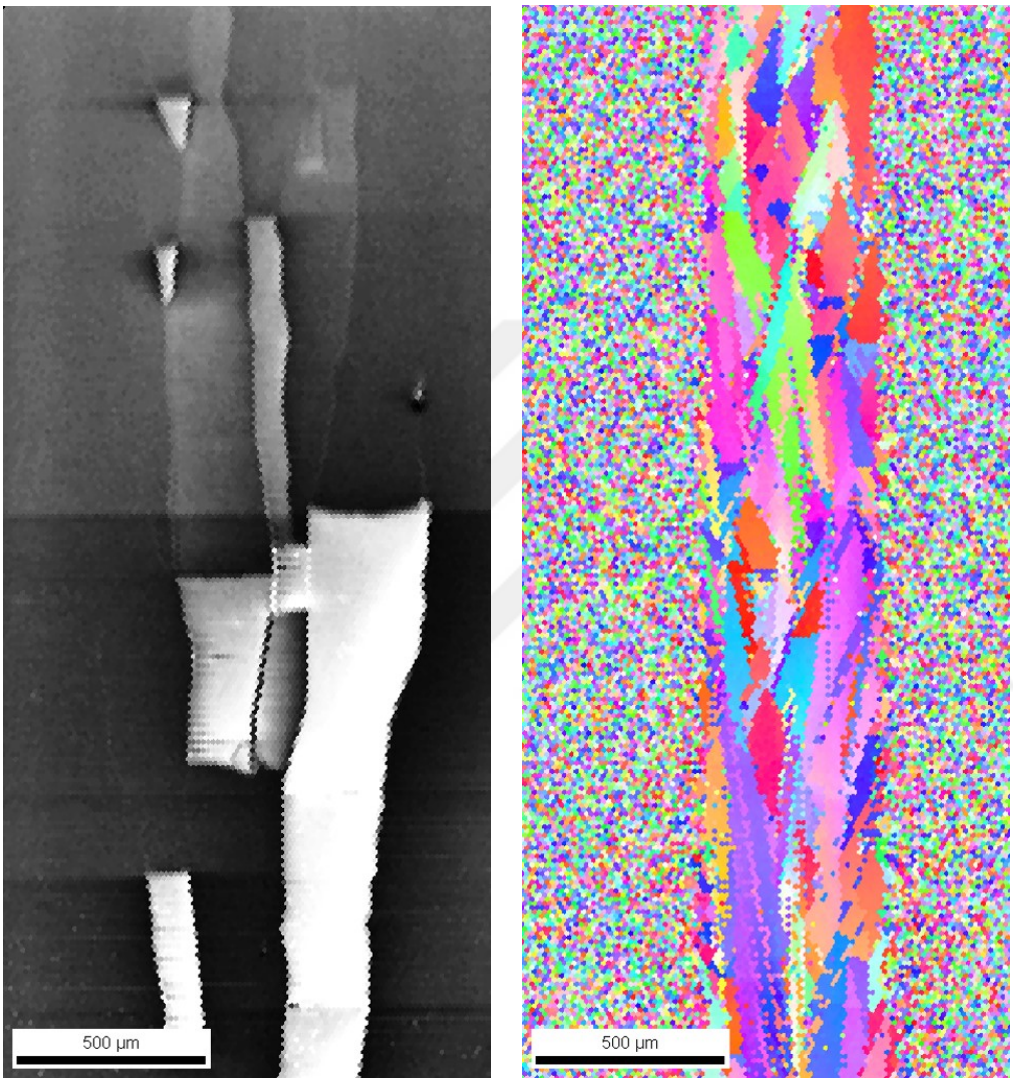

(a) (b)

Figure 4.17: a) SEM and b) EBSD images of Line 5

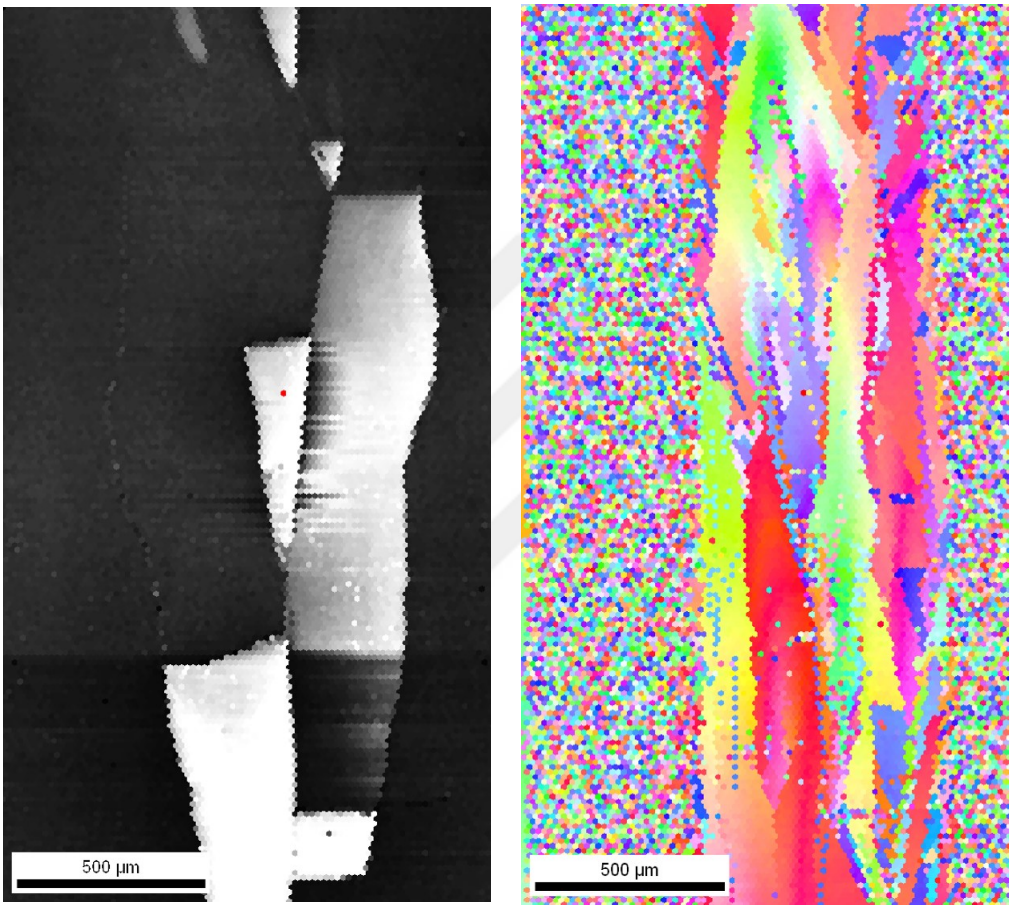

(a) (b)

Figure 4.18: a) SEM and b) EBSD images of Line 6

4.2 Effects of Si film thickness on laser crystallization and fluence correlation

To introduce the LC process on the different thickness of a-Si layers, how much energy should be calculated for a specific volume of a-Si. As to calculate the energy amount, the temperature dependent specific heat capacity of Si should be considered (see Figure 4.19).

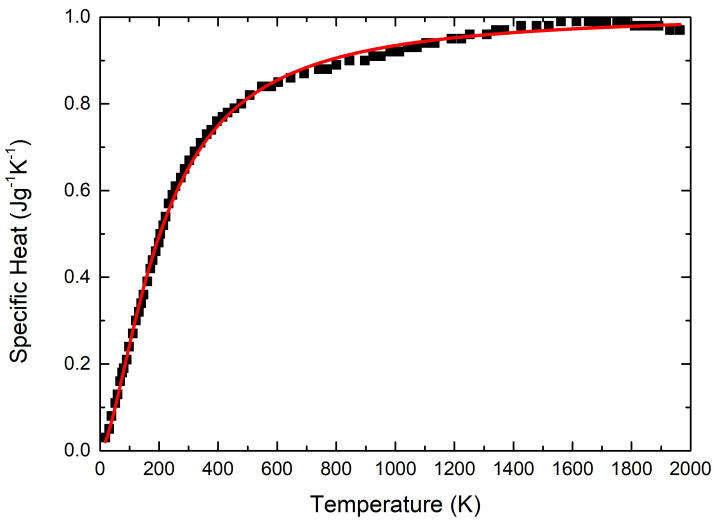

Figure 4.19: Temperature dependent specific heat capacity of Silicon [72].

In Figure 4.19, the data points of the plot is acquired from the Reference [72] and then the data points are fit to Equation 4.1. The equation is needed in order to find out how much energy is required in order to increase the temperature of the silicon up to a specific temperature with the temperature dependent specific heat, $C(T)$ where T is in Kelvin.

$$C(T) = 1.00996 \frac{T^{1.5888}}{4716.77 + T^{1.5888}} \tag{4.1}$$

Required energy in order to liquefy the silicon is calculated by integrating the specific heat of silicon (C_s) over temperature from the room temperature of 300 K to the melting temperature (T_m: 1687 K) and to the boiling temperature (T_b: 3173 K) of the

silicon separately as Equation 4.2.

$$Q = \int_{300}^{T_m, T_b} mC(T)dT \tag{4.2}$$

These energy values are calculated for the irradiated volume which had dimensions of effective fluence area times the thickness of the a-Si layer on the substrate of glass. The effective irradiated area is 45μm x 650μm with various thicknesses which are considered when calculating the irradiated mass (m). The required energies which are needed in order to increase the temperature of the irradiated volume of a-Si up to melting and boiling temperatures are converted into the fluence values for comprehensive values which are necessary for checking the coherence of the experiment with the previously done processes. The minimum and maximum required fluences are calculated in order to be in the safe zone for crystallization and not to exceed the damage threshold energy values of a-Si for that of the thicknesses.

The absorption of a-Si varies with varying thickness. In order to find out how much laser fluence are needed, the optical absorption of a-Si with different thicknesses at the wavelength of 1064nm should be revealed. The optical absorption of a-Si are measured via a photo-spectrometer and the absorption coefficient of the silicon is found. In order to calculate how much percentage of the irradiated energy is absorbed through those thicknesses calculated and the extinct energy through the silicon layer is plotted with respect to the thicknesses of a-Si. Figure 4.20 shows the extinct energy percent of the irradiated fluence though the thicknesses of a-Si.

The extinct energy percent gives how much of the effective fluence contributes to the crystallization which is absorbed by the a-Si layer. The extinct energy ratio (ξ) is calculated as

$$\xi = 100 \times (1 - te^{-6.197 \times 10^{-4}}) \tag{4.3}$$

where t is the thickness of the a-Si in nm and ξ is the percentage of the extinct energy through that thickness. The applied fluence on the surface is determined by mean of dividing the required energy for melting or boiling temperature, $Q_{m,b}$, by the extinct energy percent, ξ. By this way, the critical fluence ranges can be designated.

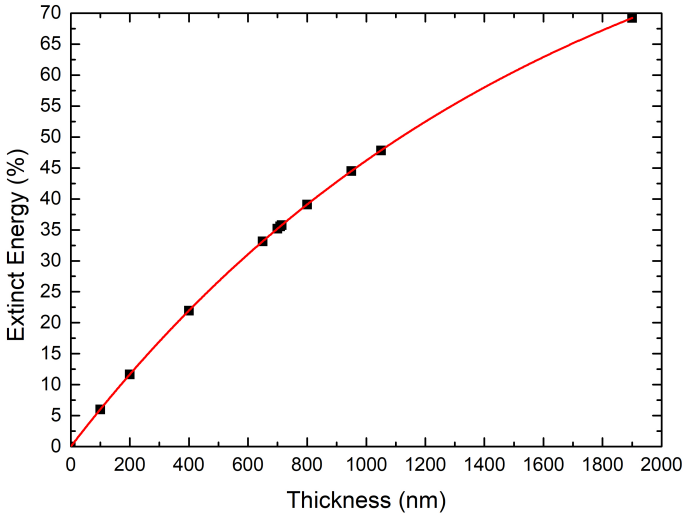

Figure 4.20: Extinct energy percent through the a-Si layer

Figure 4.21 shows that the minimum and maximum fluences required in order to melt and boil the irradiated volume of a-Si with that thicknesses and the experimental green data point are the required fluences in order to crystalline that irradiated volume of a-Si. The experimental data points for the a-Si thickness of 100 nm and 200 nm have not been required because there are some adversities of crystallization with those thicknesses which have much less energies absorbed through those thicknesses. The green fit line shows that the experimental datum are inbetween the min. and max. fluences.

The Raman spectroscopy method is used to ensure that the crystallization has occurred (see Figure 4.22). The reference bulk c-Si Raman Signal peak position and the peak FWHM are measured at the time of measurements in order to compare the results with respect to the thicknesses of laser crystallized a-Si layers.

The Raman signal analysis shows in Figure 4.22 that all the a-Si layers with different thicknesses are crystallized by the laser in the range of the minimum and maximum fluence trends.

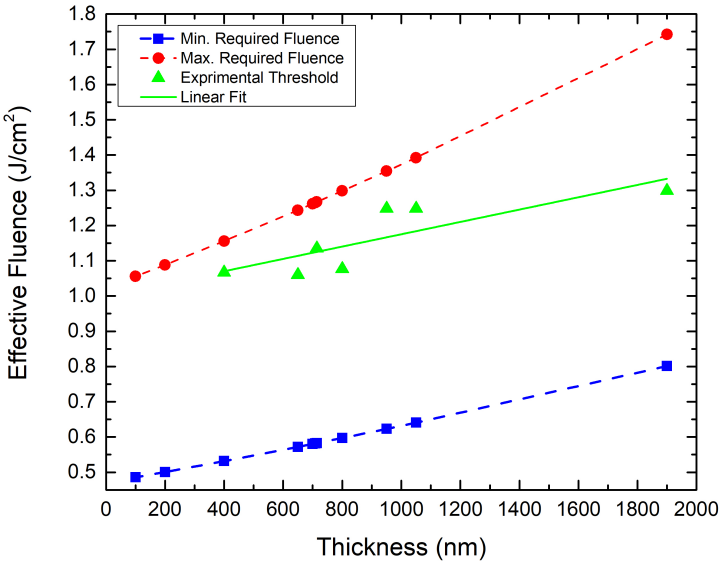

Figure 4.21: Minimum and maximum fluences needed to rise the temperature of a-Si layers for melting and boiling respectively and the experimentally determined fluence needed in order to crystalline the layers of a-Si with various thicknesses.

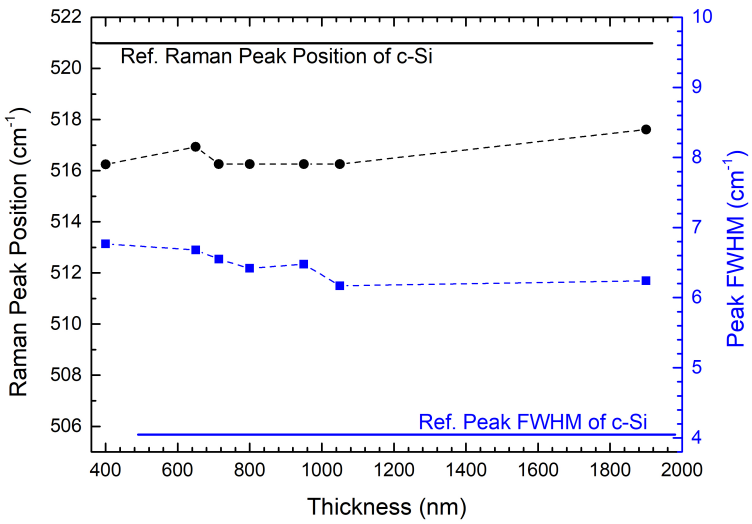

Figure 4.22: Raman signal analysis for various thicknesses of LC a-Si layer

4.3 Influence of overlapping laser pulses on laser crystallized Si surface

In this section the effects of the overlapping consecutive pulses are going to be discussed. Firstly, i-a-Si thin film of 650 nm is scanned at the damage threshold fluence over the glass substrate (see Figure 4.23).

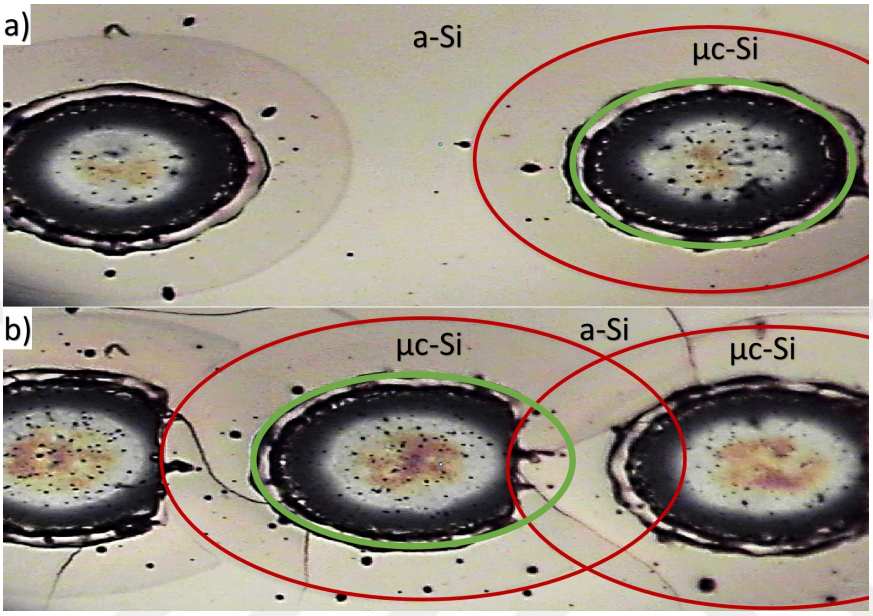

Figure 4.23: Consecutive pulses at the damage fluence of threshold a) without overlap and b) with overlap.

In Figure 4.23a, non-overlapped two pulses are shown with the regions such as, a-Si area (intact region), the crystallized region, (which is designated as μc-Si, is in between the red and green circles), and the damaged region (which is located inside the green circle). It can be perceived easily that the ablation of silicon occurs and the glass substrate appears at the center of the green circle. If the pulses are made to overlap up to some extent, the damaged region, which is inside the green circle, starts to be covered by a successively formed crystalline film which is produced by the consecutive pulse (see Figure 4.23b). The intersection of the green circle and the red circle can been seen in Figure 4.23b and the coverage of the successively crystallized area. The scan parameters of the sample a) and b), in Figure 4.23, are given on Table 4.3.

When a consecutive pulse impinges on the intact region of a-Si, a wave of liquefied

Table 4.3: Laser scan parameters of overlapping and non-overlapping pulses in Figure 4.23

Figure 4.23	Peak Fluence (J/cm^2)	v_s (mm/s)	Overlap Ratio (%)
Sample a)	14.7	3433	No Overlap
Sample b)	8.2	1962	35

silicon starts to sprawl radially and cover the damaged region, which is formed by a previous pulse. The overlap ratio of the consecutive pulses and the fluence strongly affect this phenomenon; however, this healing mechanism has to be limited. Since the amount of liquefied silicon, fluence energy and the size of the damaged area are the parameters that determine the healing percentage. The volume of displaced liquid silicon which is relevant to the thickness of the a-Si film is determined by the fluence of the laser and pulse shape.

In this section, the overlap of consecutive pulses are examined in detail. The experiments are done by performing the LC without damaging the silicon films over glass substrates. Various thicknesses of a-Si films are processed with the different overlap ratios of laser pulses.

Thicknesses of 800 nm, 950 nm and 1050 nm i-a-Si layers are deposited on glass substrates via e-beam method. The average fluence of 1.52 J/cm^2 are applied with various overlap percentages of the line focus in order to crystallize the silicon films. The scan directions is position perpendicular the long axis of the line focus. The Raman peaks of the crystallized area are measured via micro Raman spectroscopy, and the Raman signal of each crystallized region is acquired from the center of the processed areas. So as to compare the Raman measurements of the crystallized regions, a reference Raman signal is collected from a bulk crystal silicon wafer. The peak position and FWHM of the reference Raman signal are 521 cm^{-1} and 4 cm^{-1}, respectively. In Figure 4.24, the peak positions of Raman Signals, correspond to the left axis, and the FWHMs of Raman Peaks, correspond to the right axis, are shown. Legends of the plot are designated the Raman Peak positions and FWHM of the Raman signals with respect to the thicknesses of 800 nm, 950 nm and 1050 nm laser crystallized i-a-Si films. The overlap percentage of the consecutive pulses are controlled by adjusting the scan speed and all scans are done by starting from 0 (non-overlapping pulses)

overlapping to 95% pulse overlapping via increasing the overlap percentage by 10%. It can be seen that the all datum exhibit same trends - i.e., the Raman peak positions and the FWHM of the Raman peaks do not vary much between 0 and 90 percent overlap, whereas the trends changes abruptly. Especially the FWHMs of Raman peaks of all datum shows the same behavior for all thicknesses of Si layers.

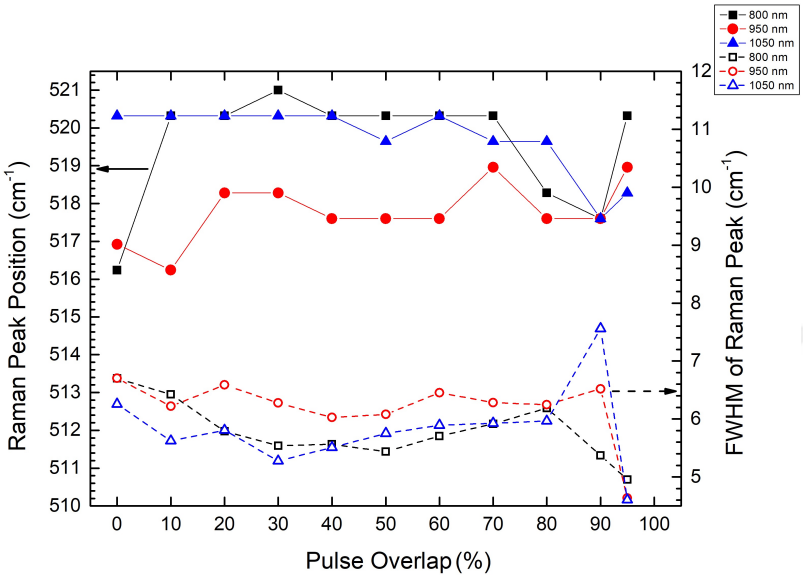

Figure 4.24: Analyses of Raman spectra of 800 nm, 950 nm and 1050 nm laser processed i-a-Si layers.

As it has been discussed before, the FWHM of the Raman peak is strongly related to the crystallinity of the surface. In order to investigate this change in FWHMs of the Raman peaks, the thicknesses of 950 nm and 1050 nm i-a-Si layers examined in detail.

Sample 1, which is deposited by e-beam method with 950 nm of i-a-Si is shown in Figure 4.25. The enumerated vertical traces are scanned with the laser parameters, which have been explained above. It is worth to mention that Figure 4.25 is captured after the AFM measurements and the polishing and cleaning processes are done.

The 3D views of the AFM scans of Sample 1, which has the i-a-Si thickness of 950 nm, are given in Figures 4.26 - 4.27, and the sequence of the 3D view of AFM measurements are given in the order of increasing **overlap ratio (Q-factor)** by the factor of 10%. The regions of the processed surface and the scan direction and line focus orientation are defined in Figure 4.26. In all 3D AFM views, the scan direction is

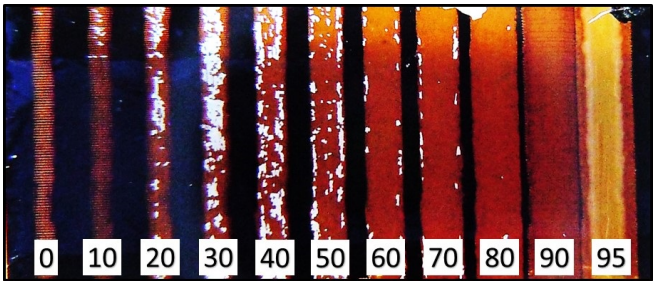

Figure 4.25: Sample 1, which has 950 nm i-a-Si film, is scanned by laser with the different overlap ratios of pulses.

along the x- axis and the long axis of the line focus is kept perpendicular to the scan direction, and along the y-axis of the 3D AFM views.

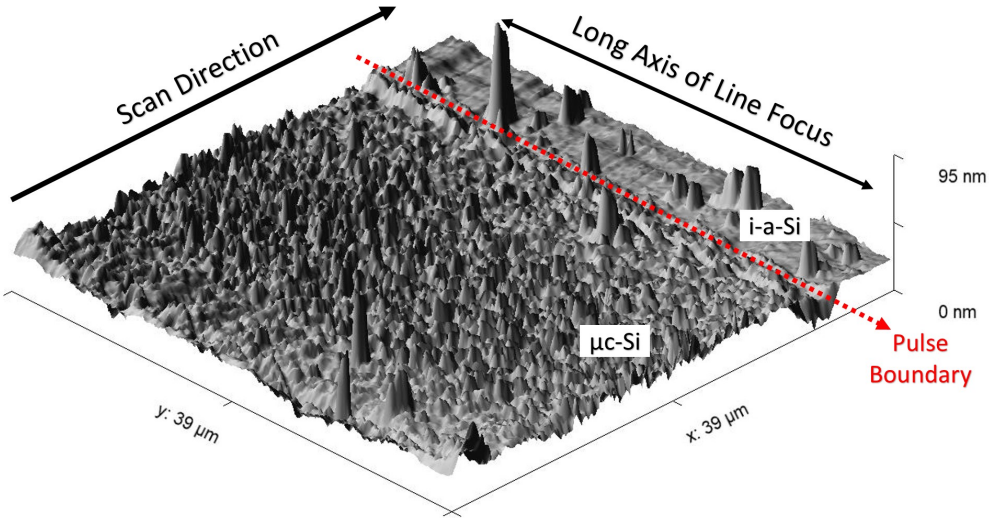

Figure 4.26: AFM image of LC processed 950 nm i-a-Si of Line 0 (Q-Factor: 0%)

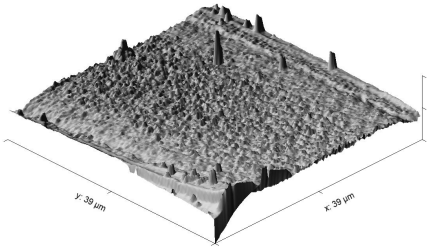

(a) Q-Factor: 10%

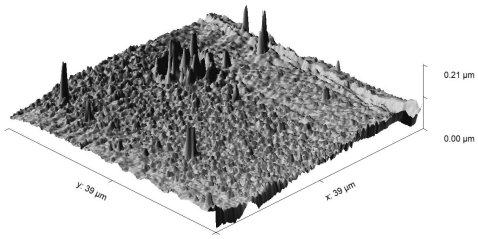

(b) Q-Factor: 20%

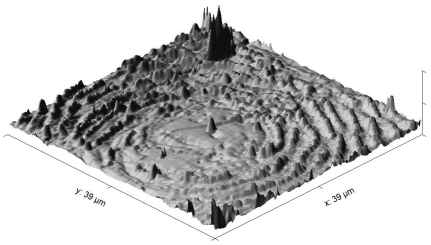

(c) Q-Factor: 30%

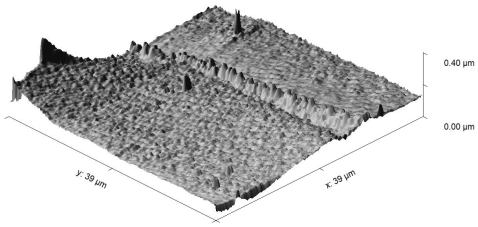

(d) Q-Factor: 40%

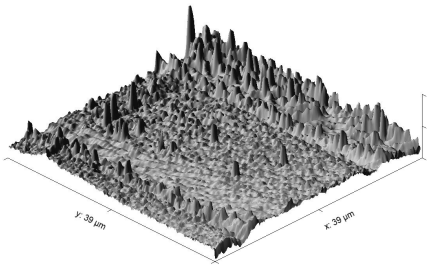

(e) Q-Factor: 50%

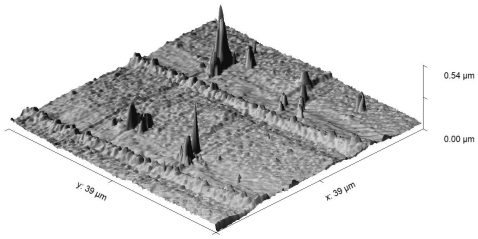

(f) Q-Factor: 60%

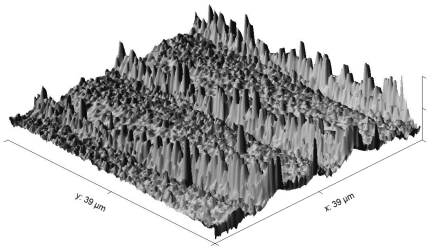

(g) Q-Factor: 70%

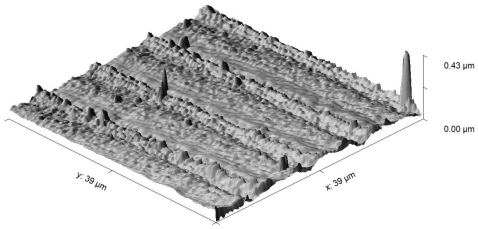

(h) Q-Factor: 80%

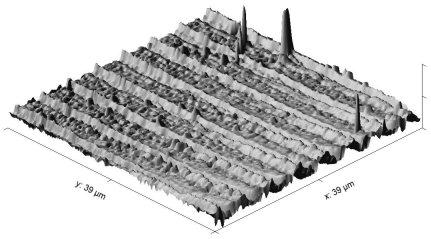

(i) Q-Factor: 90%

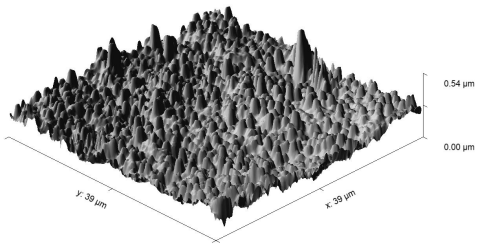

(j) Q-Factor: 95%

Figure 4.27: AFM images of LC processed 950 nm i-a-Si of Line 1-10 of Sample 1

If Figure 4.27d - 4.27i are examined carefully, it will be seen that a boundary which is in a shape of a gutter starts to form, starts transforms to consecutive ridges and hillocks with increasing Q factor. Figure 4.28 shows the boundary formation between the overlapping pulses with Q-factor of 30%. The boundary in Figure 4.28 starts to be clearer in the figures of Q-factors, higher than 30%. Up to Q-Factor of 90%, hillocks become noticeable; however, the ridges and hillocks disappear after exceeding the Q-Factor of 90%.

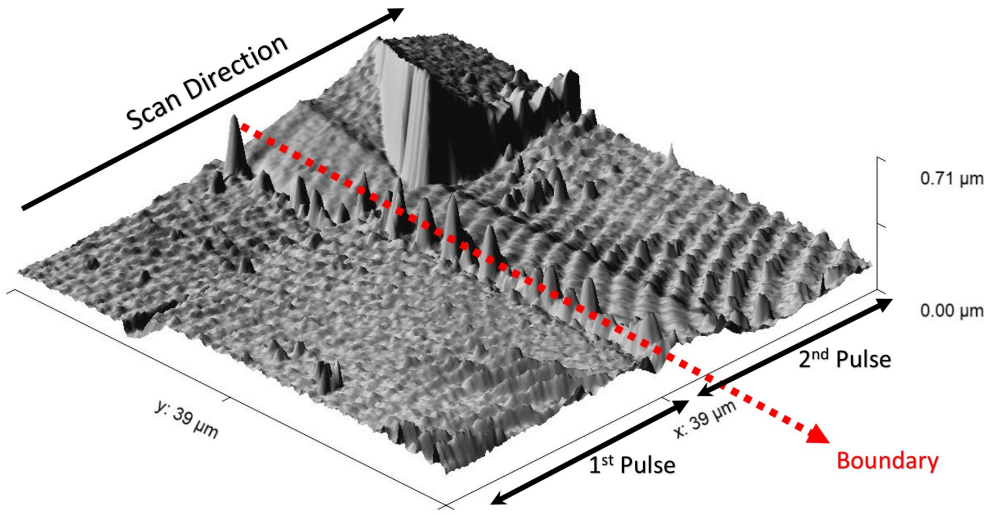

Figure 4.28: Boundary is formed by two consecutive overlapping pulses (Q-factor: 30%).

Further investigation on Q-factor is going to discuss later with comparing the LC processed 1050 nm i-a-Si layers. Especially the regime, which is after Q-factor of 95%, is going to be discussed in detail. Before move onto this discussion, the 2D roughness values of the previous measurements of LC processed 950 nm Si layers should be paid attention. The irradiated areas by laser pulses are analyzed by considering the previous AFM measurements and the 2D roughness values are calculated. The 2D RMS (root mean square) roughness parameter (S_q) is calculated for each area as follows:

$$S_q = \sqrt{\frac{1}{mn}\sum_{k=0}^{m-1}\sum_{i=0}^{n-1} z^2(x_k, y_i)} \quad , \tag{4.4}$$

where m and n are numbers of measurements done for regarding area, x_k and y_i are the coordinate of the measured height difference of z. S_q parameter is calculated regarding ISO 25178-2 for 3D reference of Geometric Product Specifications (GPS). The S_q parameters for Sample 1, with the thickness of 950 nm i-a-Si layer, is given in Figure 4.29.

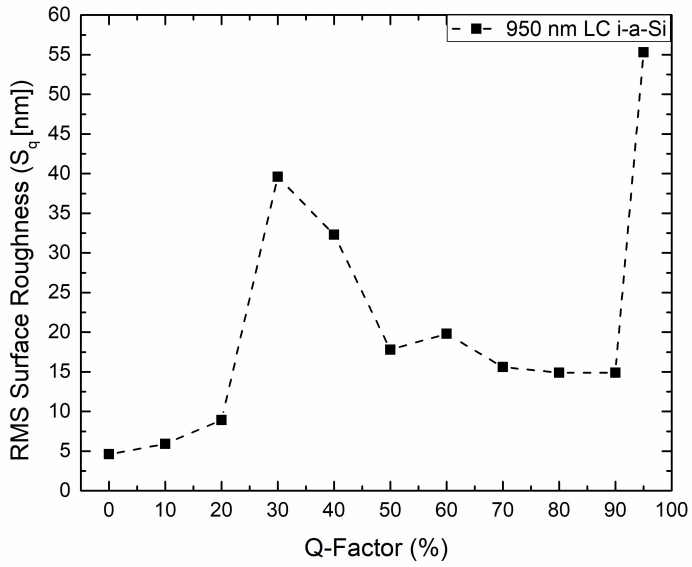

Figure 4.29: S_q parameters, with respect to Q-Factor for the LC processed i-a-Si of 950 nm.

The S_q is not correlated with the Q-factor directly. The main trend can be deduced as increasing S_q with increasing Q-factor; however, the jump which is between Q-factors of 20% and 50%, can be perceived easily.

If Figure 4.29 is compared with Figure 4.30, the dramatic change in crystallinity can be attributed to the higher Q-factors exceeding 90%. Let's move onto the next sample, which is deposited 1050 nm i-a-Si layer via e-beam method, is processed with the Q-factors between the values of 99.2% and 99.9%. Sample 2 is deposited by e-beam with 1050 nm i-a-Si film. This sample is scanned with different laser parameters which are not corresponds to the laser parameters of the previously investigated the i-a-Si film of 1050 nm thickness. The laser parameter are given as in Table 4.4.

The corresponding sample and the lines are shown in Figure 4.31. The captured photo of Sample 2 is edited by changing the contrast and lightening and also it is labeled in

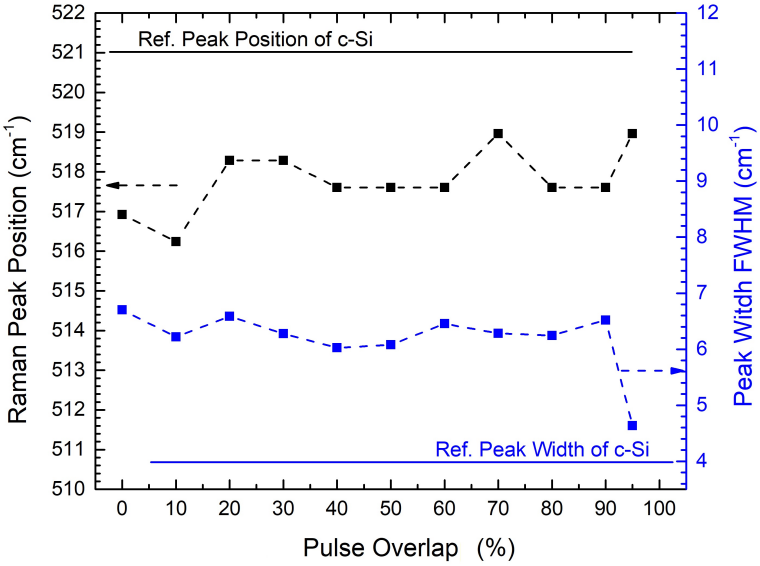

Figure 4.30: Raman analysis of Sample 1, LC i-a-Si of 950 nm.

Table 4.4: Laser scan parameters of Sample 2 in Figure 4.31

	Av. Power	Effective Focus Dimensions	Effective Fluence	Pulse Duration	Repetition Rate
Laser Parameters	12 Watt	45 μm x 1250 μm	0.21 J/cm^2	200 ns	100 kHz

Line #	Line 1	Line 2	Line 3	Line 4	Line 5	Line 6	Line 7	Line 8
v_s (mm/s)	5	10	15	20	25	30	35	5
Q-factor (%)	99.9	99.8	99.7	99.6	99.4	99.3	99.2	99.9

order to clarify the processed regions and highlight the crystallization direction along the scan direction. Figure 4.31 is captures after the HF process and cleaning.

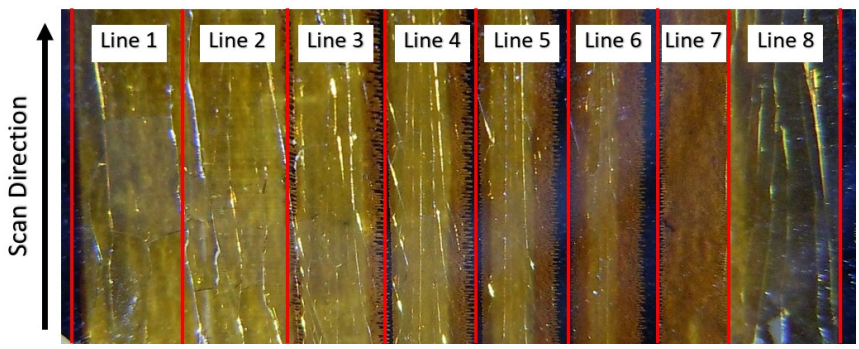

Figure 4.31: Sample 2 of LC processed 1050 nm i-a-Si

Closer microscope images with phase contrast are also acquired and are given in Figure 4.32 - 4.39.

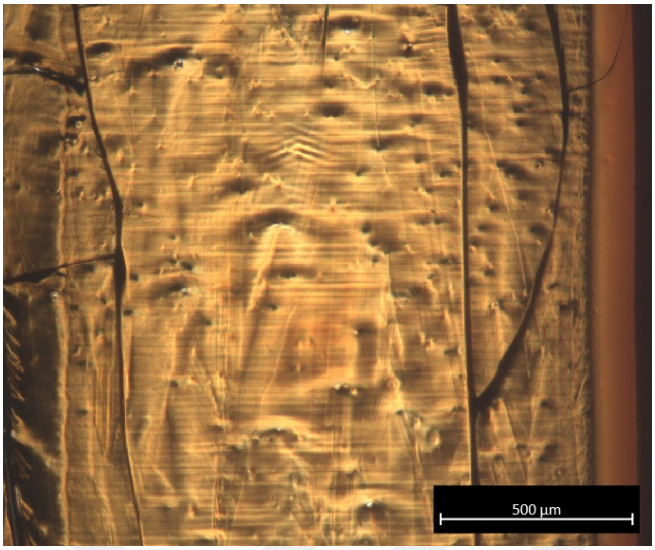

Figure 4.32: Optical microscope image of Line 1 (Q-Factor: 99.9%) with phase contrast

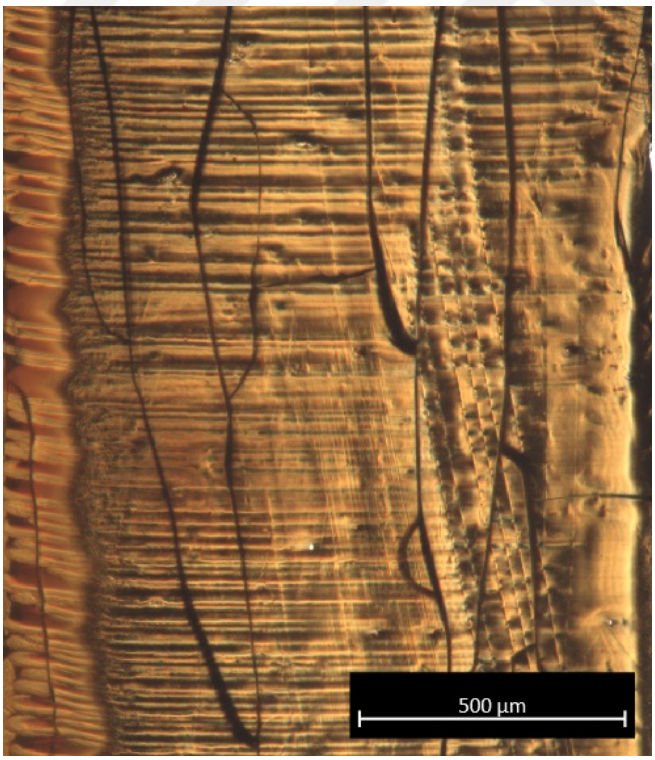

Figure 4.33: Optical microscope image of Line 2 (Q-Factor: 99.8%) with phase contrast

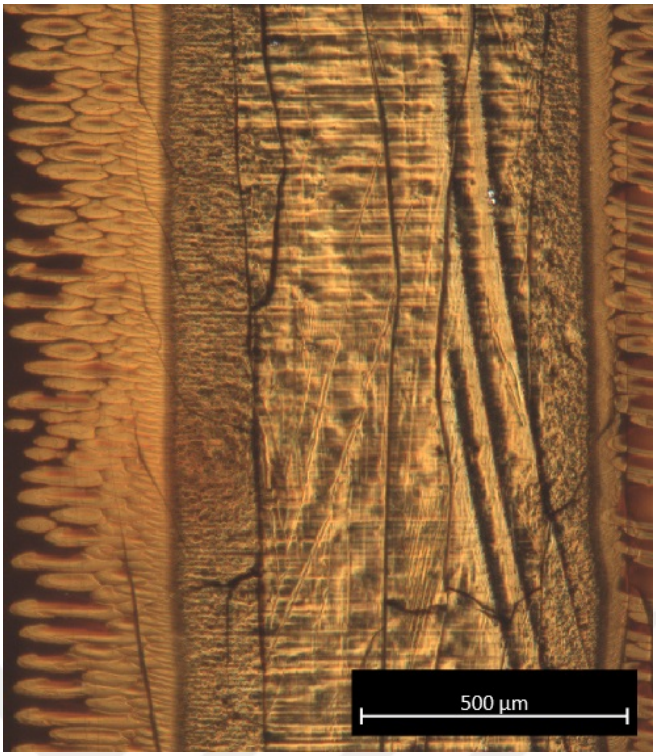

Figure 4.34: Optical microscope image of Line 3 (Q-Factor: 99.7%) with phase contrast

The dark sides at the left or right sides of Figure 4.34 - 4.39 are the unprocessed regions of 1050 nm i-a-Si layer. The scanned areas are checked by Raman spectroscopy and their crystallization is examined quantitatively in Figure 4.40 with respect to their corresponding scan speeds. Up to some extent, the stress over the crystalline domains decreases with increasing scan speed (with decreasing Q-factor) till the scan speed reaches the speed of 35 mm/s. Later on, EBSD images of the scanned areas are going to be investigated; however, it is worth to mention that the crystal grains sizes increase with decreasing scan speed. This phenomenon does not match the previously discussed mechanism which is opposite of the finding that the tensile stress is inversely related to the grain sizes. When Figure 4.40 is studied carefully, the position of Raman Peak starts to shift to the smaller wave numbers which can be attribute to the drastic change in grain sized in Line 7, scanned with 35 mm/s.

For Line 7 the grain formations are limited and localized and the crystal domains did not grow as much as the other lines. The scaly structures can be seen in Figure 4.38. Insufficient laser fluence cannot induce crystallization as it discussed before and only

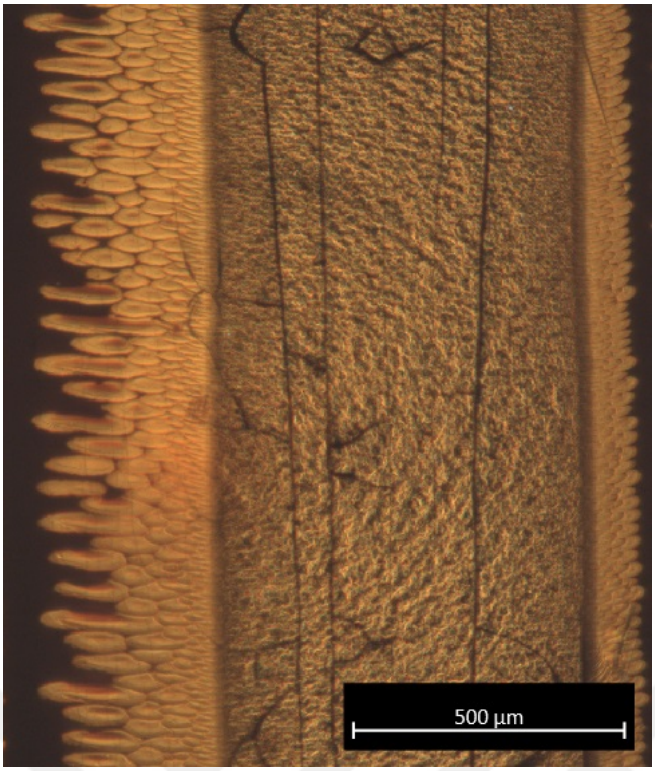

Figure 4.35: Optical microscope image of Line 4 (Q-Factor: 99.6%) with phase contrast

the gradual heat accumulation initiates the LC process. The dimensions of flakes are approximately 45 μm which corresponds to the maximum effective width of the line focus (Compare Figure 4.38 with Figure 4.48). The fluence is below the threshold level to crystallize that thickness of i-a-Si. Sample 2 is not scanned by the fluence as much as Sample 1 is, so they are not comparable samples. Sample 2 of 1050 nm i-a-Si film is not scanned with as much fluence as Sample 1 of 950 nm i-a-Si film in order not to damage the surface of it because of excessive heat accumulation induced by overlapping pulses. Therefore it is not appropriate to compare the Raman Analyses of these samples. To perceive the crystalline domain sizes over the scanned areas, let's discuss the EBSD analyses of Sample 2. After fine polishing and HF cleaning of Sample 2, the EBSD measurements are proceeded (see Figure 4.41 - 4.44).

The EBSD images of the lines of Sample 2 are shown in Figures 4.41- 4.43. The color map, which is to define the orientations of crystalline domains, is given in Figure 4.43 d). Line 1, 2, 3, 4 are analyzed by measuring lengths of the each domains individually. The measuring of Domain lengths are proceeded as it is done for the analysis of Line

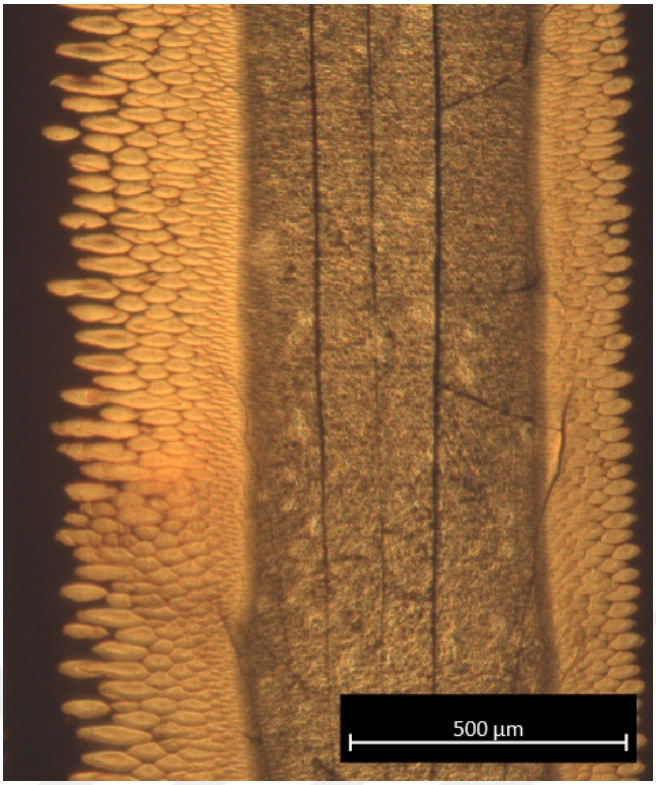

Figure 4.36: Optical microscope image of Line 5 (Q-Factor: 99.4%) with phase contrast

8 in Figure 4.44. Firstly, the color contrast of EBSD images are increased by image process, and the individual formed crystalline domains are selected as in Figure 4.44. In Figure 4.44, only four of the longest domains are selected for the sake of clarity; whereas the all crystalline domains are taken into account on the images of Line 1, 2, 3 and 4.

The EBSD image analyses of Line 5, 6 and 7 are not done, since the sizes of grains are not as long as those of Line 1, 2, 3 and 4 and shapes and numbers of the crystalline grains are not suitable to determine an analysis method in order to measure the individual length of the grains. For an example, the lengths of the grains, labeled as 1, 2, 3 and 4 in Figure 4.44, are measured as 1696 μm, 1876 μm, 1491 μm and 2028 μm respectively. The histograms of grain lengths of Line 1, 2, 3 and 4 are shown in Figure 4.45.

The average lengths of the domains are found as 1020 μm, 570 μm, 520 μm and 430 μm for Line 1, 2, 3 and 4, respectively. As it is perceived from the findings that the

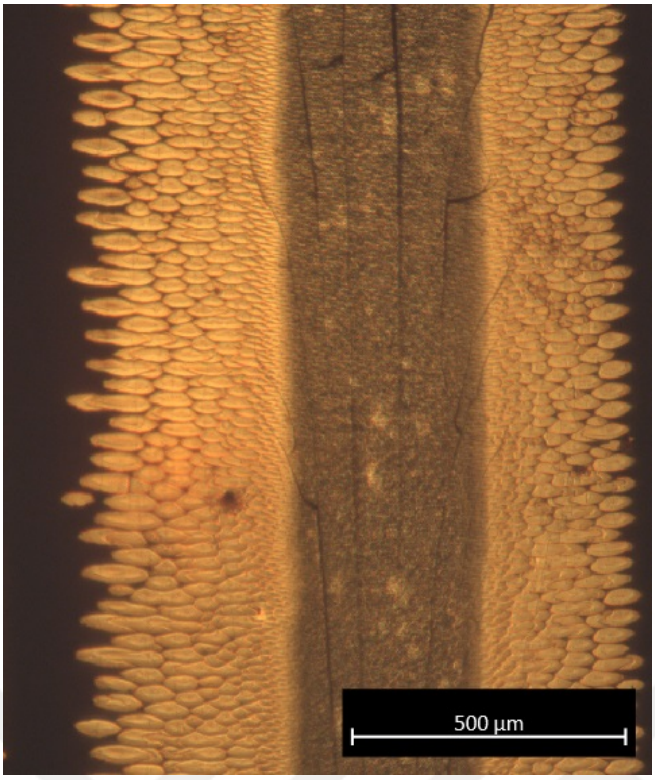

Figure 4.37: Optical microscope image of Line 6 (Q-Factor: 99.3%) with phase contrast

length of crystalline domain can be grown up to 2 mm. If the heat accumulation is increased by decreasing the scan speed as a consequence increasing the Q-factor on the surface of the Si layers, the controlled cooling can provide larger laser crystallized domains. The width of the crystallized domains are strongly related with the width of the line focus of the beam and spatial homogeneity of its fluence distribution. Unfortunately, it is not discussed in the content of this section.

The RMS surface roughness (S_q) parameters of the each line are calculated by acquiring the AFM images of the lines for the scan area of 39 μm x 39μm. Figure 4.46 shows the AFM images of Line 1 - 6. The S_q values are calculated as it is done previously and plotted with respect to their corresponding scan speeds. Figure 4.46 does not include the AFM image of Line 7. Because it does not resemble to the AFM images of the other lines. So it is discussed separately.

The roughness of the surface increases with increasing scan speed that is also correlated with the previous findings (see Figure 4.47). The drop in value of S_q (for

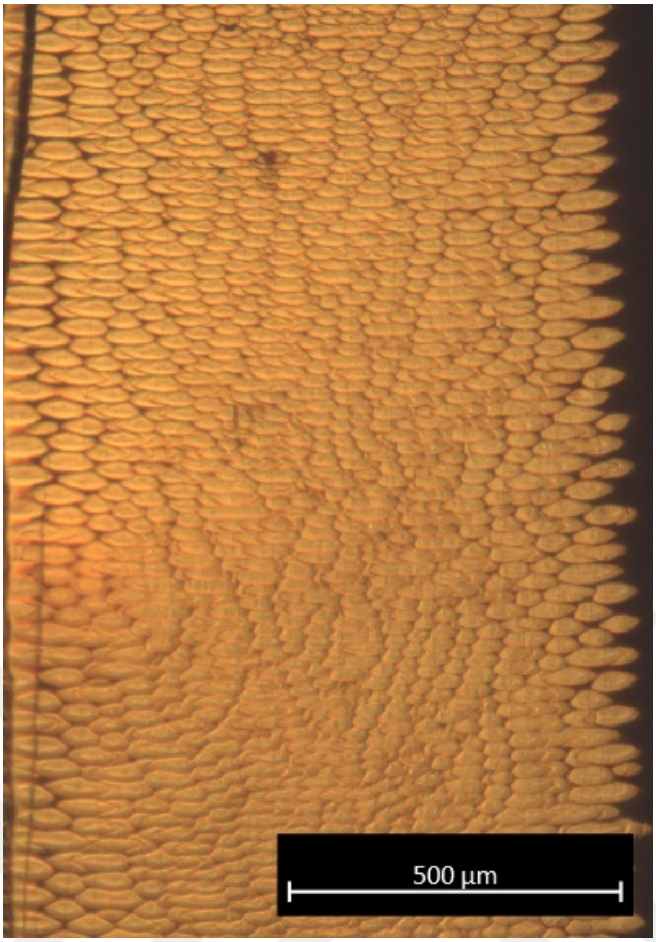

Figure 4.38: Optical microscope image of Line 7 (Q-Factor: 99.2%) with phase contrast

Line 7) can be attributed incomplete crystallization of the surface at the speed of 35 mm/s for the thickness of 1050 nm i-a-Si film. The inadequate heat accumulation have resulted in partial crystallization and non-crystallized regions made the value of S_q to decrease up to some extent. It is worth to remind that the healing/self-curing mechanism occurs at Q-factor of 99.9% for Sample 2 and for the fluences, below the crystallization thresholds, this healing regime can be initiated right after Q-factor of 99.2%. The detailed AFM image of Line 7 and its corresponding microscopy image are given in Figure 4.48.

The fluence of an individual laser pulse is not enough in order to crystallize the 1050 nm thick i-a-Si layers for Sample 2. The heat accumulation should be needed to build up enough energy melt down for that thickness of Si layer. For that reason, the comparison of Sample 1 and 2 are not reasonable. For Sample 1, the effective

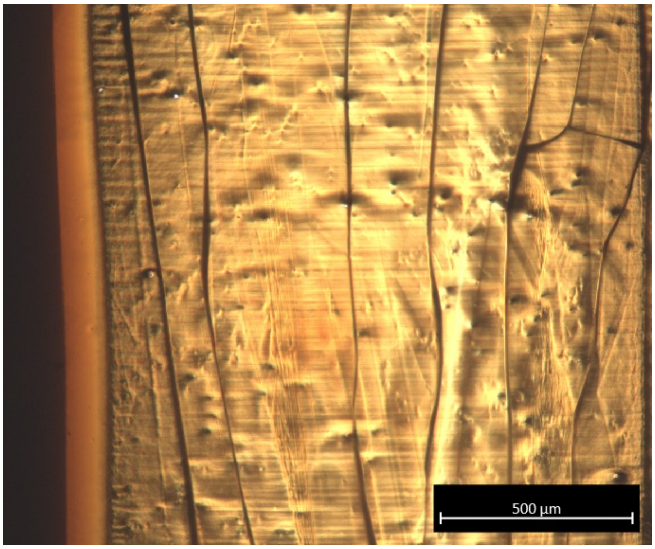

Figure 4.39: Optical microscope image of Line 8 (Q-Factor: 99.9%) with phase contrast

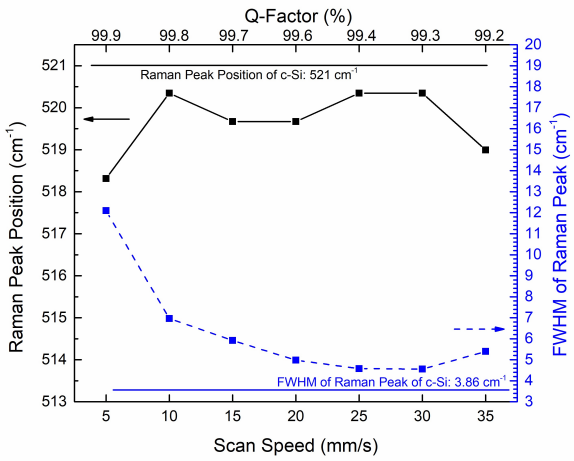

Figure 4.40: Raman analysis of Sample 2 with respect to the scan speeds, which correspond to the numbers of lines.

fluence is 1.52 J/cm^2 that it has enough fluence to liquefy the 950 nm i-a-Si layer for an individual laser pulse. If the Raman analysis of Sample 2 is considered, it will be noticed that the Raman redshift is related to the sizes of the crystalline domain, which exhibit inverse relation with the tensile stress over the surface. The tensile stress does not change much when the redshift of the Raman Peaks of Line 2 - 6 are considered. However, the Raman peak position of Line 7 shifted to red for Sample 2. This can be also deduced from the EBSD image of Line 7 by examining the

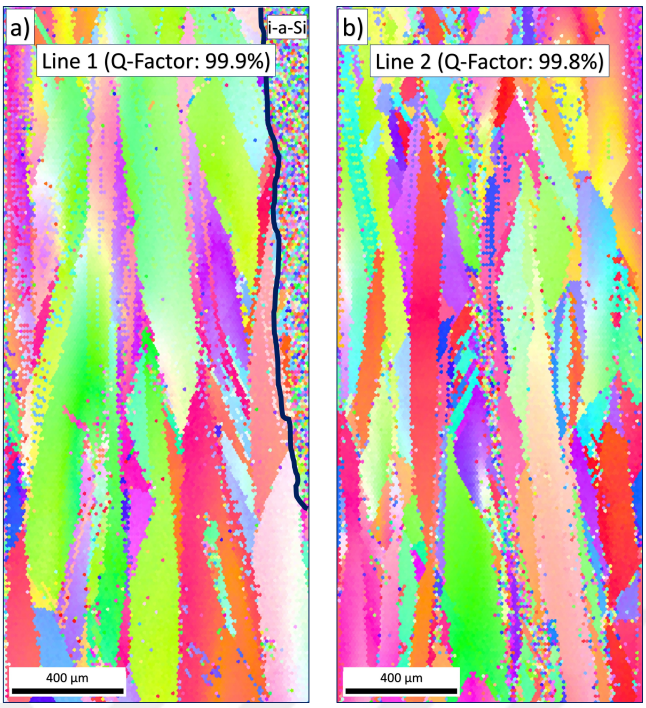

Figure 4.41: Sample 2 of LC 1050 nm i-a-Si Film: a) EBSD image of Line 1, b) EBSD image of Line 2.

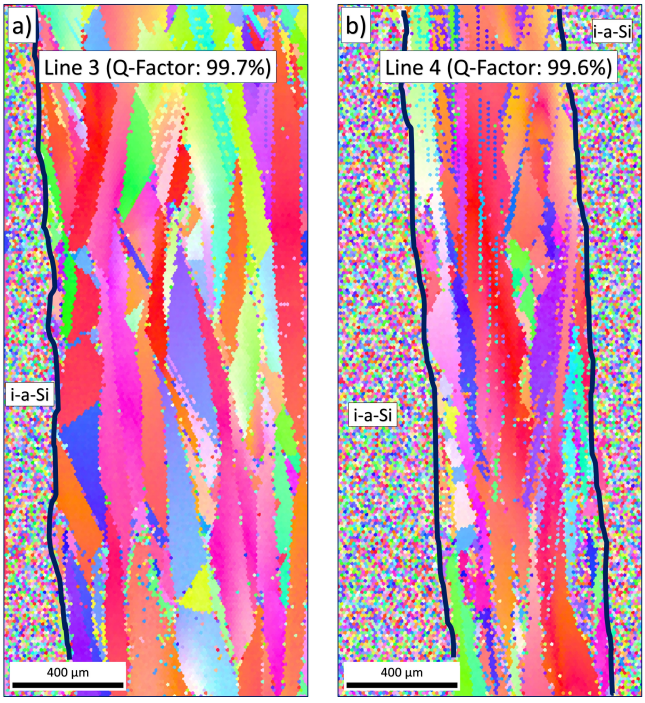

Figure 4.42: Sample 2 of LC 1050 nm i-a-Si Film: a) EBSD image of Line 3, b) EBSD image of Line 4.

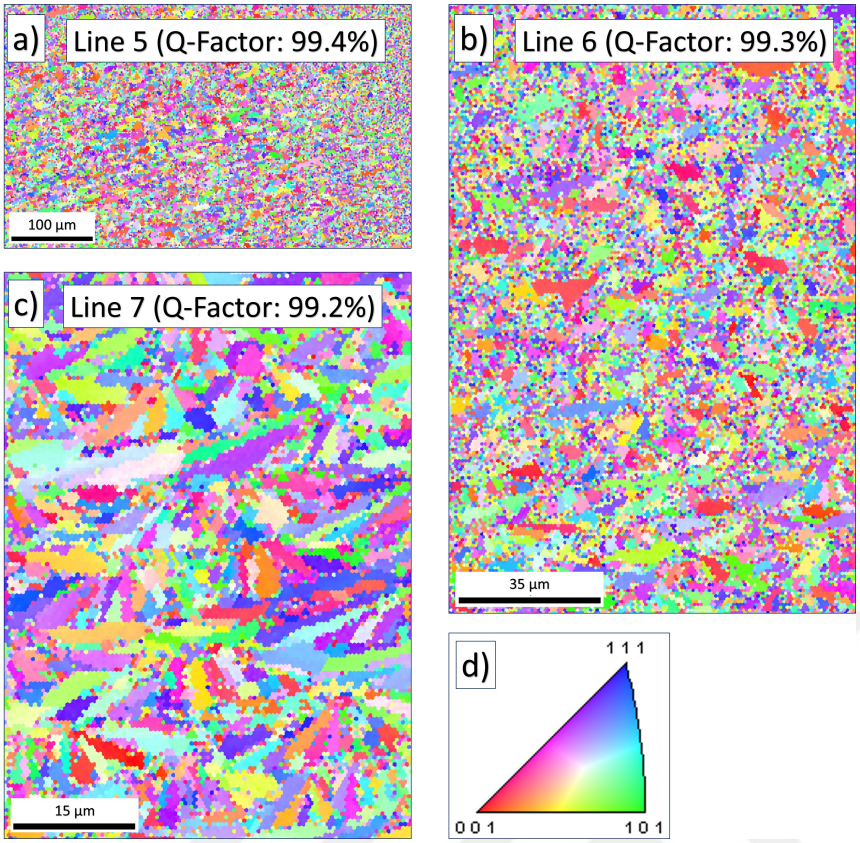

Figure 4.43: Sample 2 of LC 1050 nm i-a-Si Film: a) EBSD image of Line 5, b) EBSD image of Line 6, c) EBSD image of Line 7, and d) Color map of c-Si in order to define the orientations of crystalline domains.

sizes of the grains. Besides, the correlation is not observed for Line 1 of Sample 2. The grain lengths are larger than any lines; however, the redshift also occurs for the Raman peak of its. This can be explained by examining the EBSD image of Line 1 by paying attention to the color map of c-Si in Figure 4.43d. As it can be realized that the colors of individual domains on Line 2-6 are discretely separated with each other. The borders of the crystallized regions can be identified easily; however, there are color gradients occur for the regions on Line 1. This shows that there are twisting phenomena occurring during the formation of the domains. This can intensely induce stress right after the solidification of the layer. The EBSD analysis of Line 1 assures that there are crystallized distinct domains; however, the crystallinity did not occur as much as Line 2-6 when the FWHMs of Raman peaks are compared. If these reasons are considered in this manner, the redshift for the Raman Peak of Line 1 can be clarified. In addition to this explanation, the redshifts for the Raman Peaks of Sample

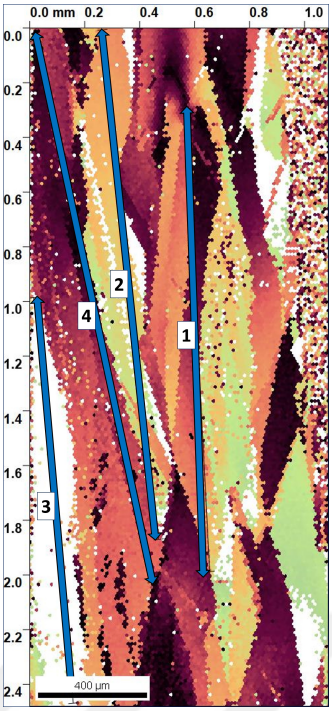

Figure 4.44: EBSD image analysis of Line 8 (Q-Factor: 99.9%), as an example of measuring the lengths of crystalline domains.

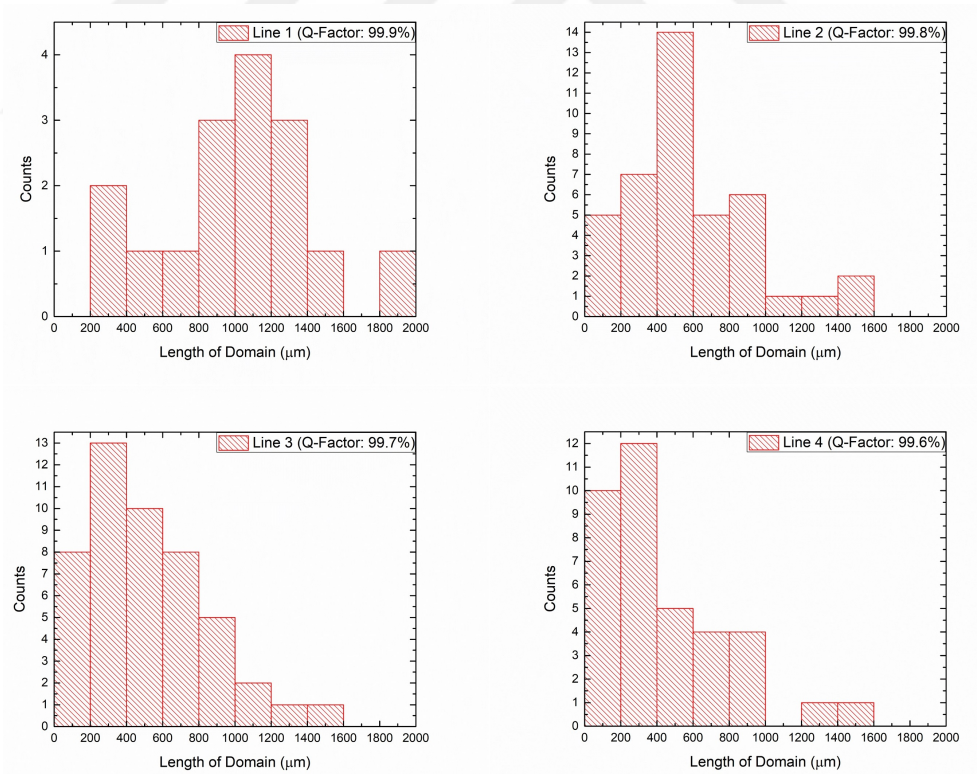

Figure 4.45: Histograms of Line 1, 2, 3, and 4: Counts vs. Length of Domain.

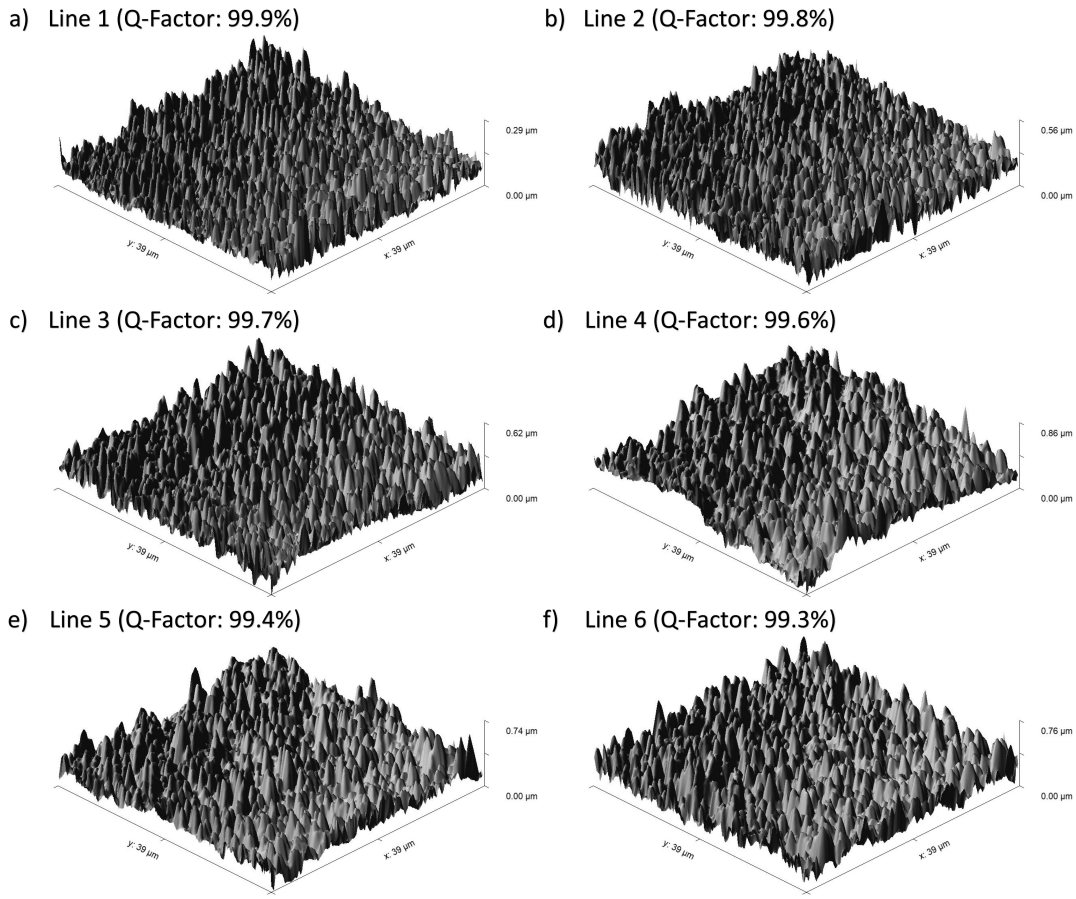

Figure 4.46: AFM images of Line 1-6

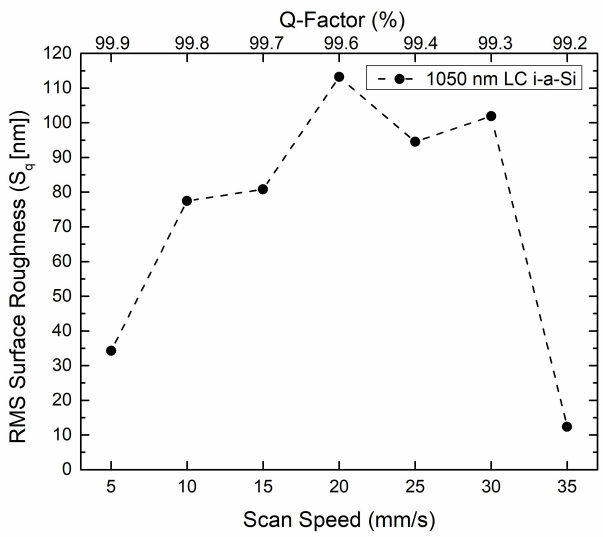

Figure 4.47: S_q values of Line 1-7 with their corresponding scan speeds.

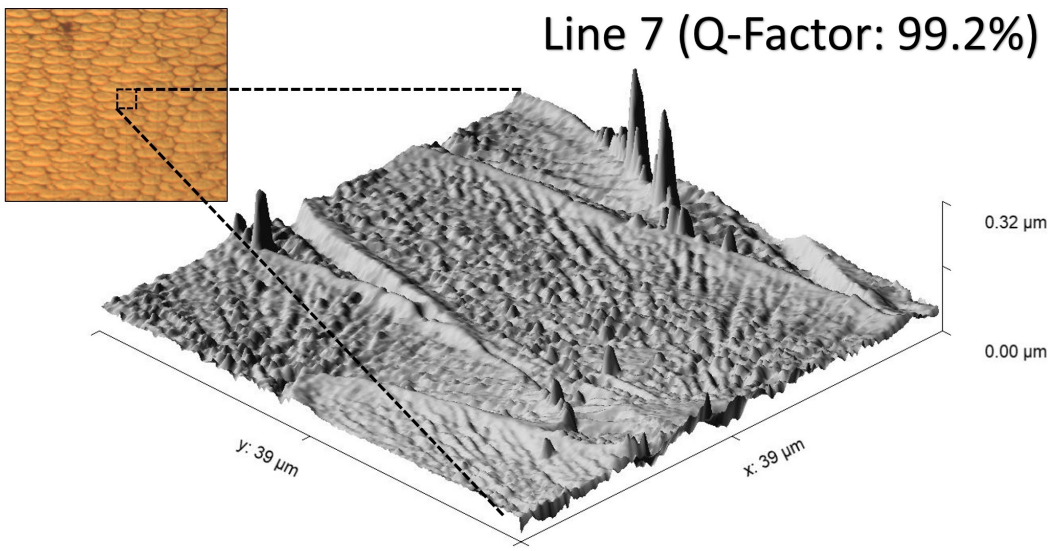

Figure 4.48: 3D view of AFM image of Line 7 with its corresponding the inset microscopy image

1 with the thickness of 950 nm Si layer decrease with increasing the Q-factor, which corresponds to decrease in scan speed and increase in overlap. This also verifies the previous explanations about the crystallinity, stress and domain size relations.

In order to determine electronic properties of the lines of LC processed 1050 nm μc-Si layers, the sheet resistance [$\Omega/\square$] of the each line is measured by Jandel Model RM3-AR, which is a 4-probe test unit. Datum of the sheet resistance are acquired form different location on the each line to calculate statistical value of the sheet resistance. Figure 4.49 shows the semi-log sheet resistance graph for Line 1 - 7 of Sample 2 with respect to their corresponding scan speeds.

Up to the end of this section, various laser scanning parameters have been discussed in the process of LC of a-Si films via the 1064 nm nanosecond pulsed laser. Optical modifications are done in order to enlarge the scan area and to improve the crystallinity and the electronic features of the a-Si films with various thicknesses. It has been revealed that the laser scanning parameters could be optimized by considering the previous discussed issues. As it is going to be discussed in Chapter 6 of device designs, the laser scanning parameters can be deduced as it is given in Table 4.5 in order to form crystalline structures at a thickness of $\sim 1\mu$m i-a-Si layer deposited by

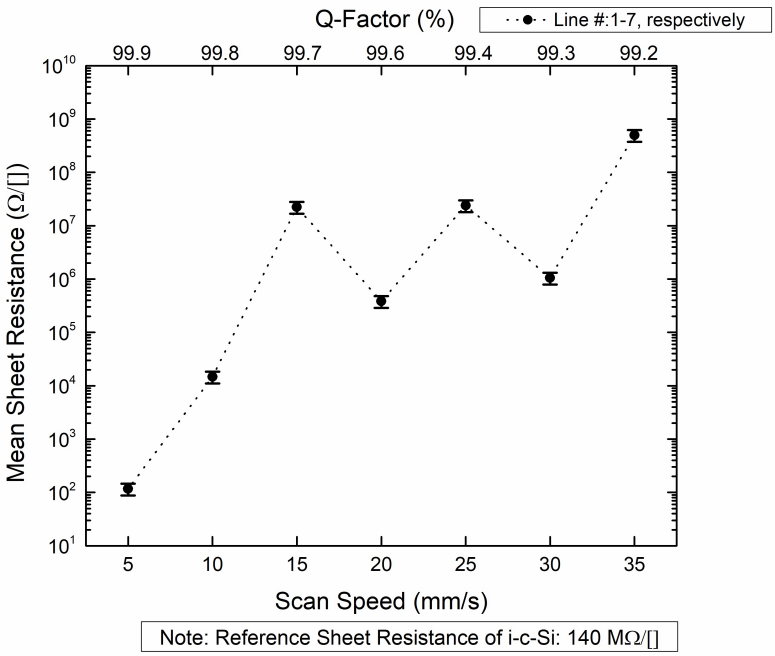

Figure 4.49: Semi-log graph of sheet resistance [$\Omega/\square$] for Line 1 - 7 of Sample 2

e-beam method.

Table 4.5: Optimized parameters of LC for $\sim 1\mu$m i-a-Si Films

Average Power	Effective Focus Dimensions	Effective Fluence	Pulse Duration	Repetition Rate	v_s (mm/s)	Q (%)
12 Watt	45 μm x 1250 μm	0.21 J/cm^2	200 ns	100 kHz	5 - 15	99.9 - 99.7

Calculated and measured fluence per pulse (No overlap: Q = 0%)	
Max. Effective Fluence	1.39 J/cm^2
Min. Effective Fluence	0.64 J/cm^2
Exp. Effective Fluence	1.18 J/cm^2

In Table 4.5, the laser scanning parameters are compared with the parameters in order to crystallizing fluence values per pulse. The effective fluence value of individual pulses with Q-factor of 99% range is smaller than the calculated and measured fluence value per pulse. This is the result of heat accumulation sustained by overlapping pulses. This also slows down the cooling and maintain the formation of larger grains over the surface. In Chapter 6, the LC procedures for device designs are mainly proceeded by considering the laser parameters, which are discussed in this section.

CHAPTER 5

DEFECT ANALYSES

During the LC process, some defects can occur under and/or above the surface of the Si layer. These defects can be caused by intrinsic agents or non-optimized laser parameters. First, let's discuss crack formation which can be easily observed by a microscope right after the LC process. In Figure 5.1, the microscope images are shown with a) Reflection mode and b) Transmission Mode. The crater is framed by a red dashed line for each image. The closer view of the crack is captured and it is shown region is enclosed by blue dash square. The reflection mode image also differs from the transmission mode by the cracks, which are deep through the glass, are appeared more than the slight cracks, which are noticeable in the transmission mode image. It can be also attributed to that the cracks reach deep down the glass substrate. The measurement of TOF-SIMS is proceeded till all layer of LC processed 950 nm i-a-Si is annihilated all the way up to the glass substrate. The crater reveals that the cracks over the surface did form through the surface of the glass substrate. In order to examine the effect of those kind of cracks the AFM measurement are done all over the cracked region.

The AFM analysis showed that the crack did not affect the laser crystallized 950 nm i-a-Si surface and the crystallized region possessed homogenous roughness and surface profile all through the cracked region (see. Figure 5.2).

The inset microscope image in Figure 5.2 shows where the AFM measurement is done. The crack can be noticed on the microscope image; however, the crack did not affect the surface profile and it did not distort the surface roughness homogeneity. Another evidence of the crack formation on the glass substrate can be perceived by examining damaged Si layers which are exposed to excessive laser irradiation during

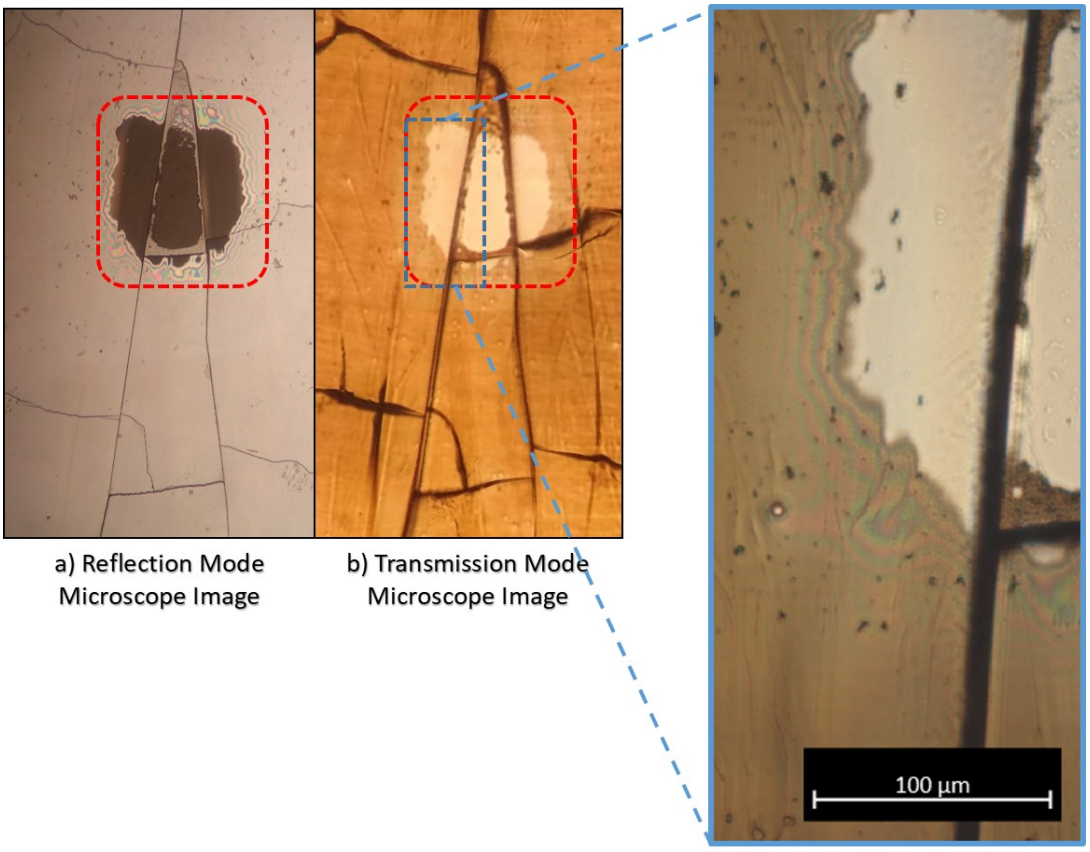

Figure 5.1: Microscope image of LC process 950 nm i-a-Si films after a crater is formed during the measurement of the TOF-SIMS

the LC process. If the Si layer is exposed to excessive laser fluence, the Si layer can be removed and the surface of the glass substrate can emerge. The formed crack by the laser can go beneath the Si layers and continue through the surface of the glass even if the Si layers are removed from the surfaces.

The cracks can be seen in Figure 5.3 and they mainly align in the direction of the laser scan. The orange colored regions are the laser crystallized area of 1050 nm i-a-Si layer deposited by the method of e-beam. The dark region at the left hand side is amorphous region of Si layer intact and the whitish regions inside the crystallized area is the removed/damaged Si layer where the glass substrate emerges during the process. The region formations can be seen in Figure 5.4 separately such as a) partially crystallized line focus scan, b) partially damaged regions via extensive fluence, c) totally crystallized line scan of the laser crystallized 800 nm i-a-Si layer and d) totally damaged/removed regions by excessive amount of laser exposure.

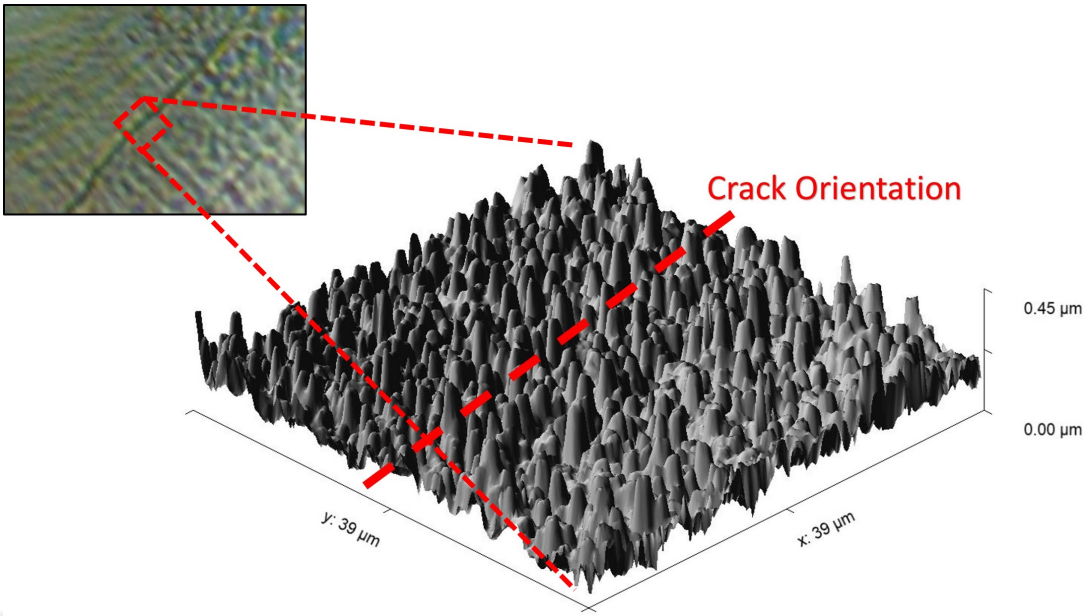

Figure 5.2: 3D view of the AFM image over the cracked region and the inset microscope image

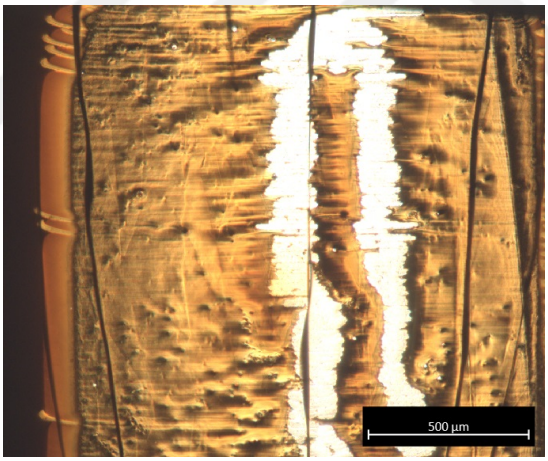

Figure 5.3: Removed/damaged Si layers over the cracked glass surface

Not only are the e beam deposited layers studied in this study, but also layers which are deposited by PECVD method are examined. The LC of PECVD deposited samples of various types of a-Si layers with different thicknesses are done. Nonetheless, the crystallization could not been performed as well as the samples, which are deposited by the e-beam method. Hydrogen content in the process of PECVD affects the crystallization of the Si layers adversely. The hydrogen starts to emerge from the Si layers during the LC process. Various trials are done with different methods in

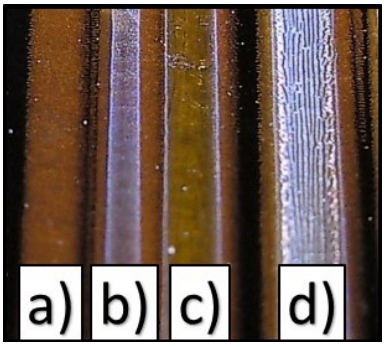

Figure 5.4: Line focus scan of 800 nm i-a-Si layer with various parameters

order to improve the crystallization of PECVD deposited Si layers. In Figure 5.5, the LC is proceeded before and after the laser annealing. The laser annealing of the separate samples takes place in this trial and the low intensity irradiation exposes at the fluence of non-liquefying energy level of that thickness of a-i-Si layers.

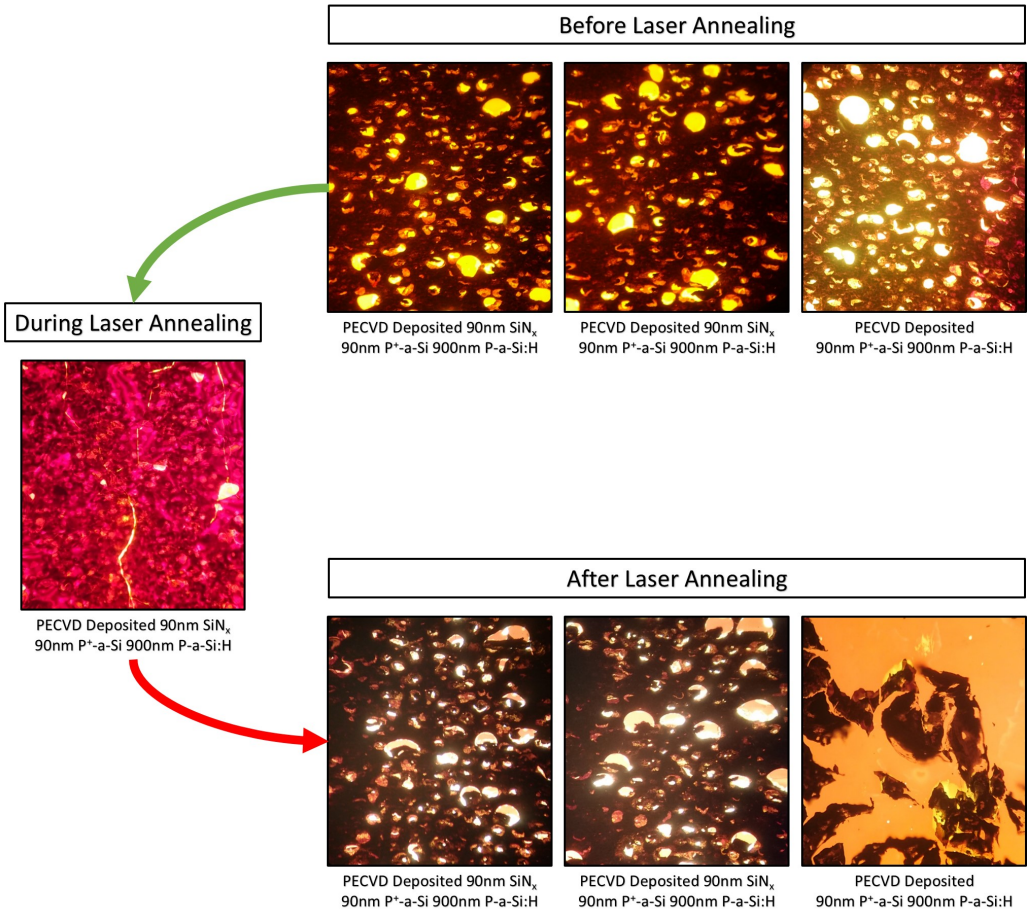

Figure 5.5: Laser crystallization of PECVD deposited samples before/during/after the laser annealing

Blistering and delamination occur as it is seen in Figure 5.5. During the laser annealing process an image of the surface is captured that unintentional crack formation occur at any low level fluences which are not capable of liquefying that thickness of Si layer. In addition to this laser annealing method, dehydrogenation is tried to be done by annealing via furnace. Even if the surfaces of the samples are undamaged after the annealing by a furnace, they get damaged during the LC process. Without exceeding the temperature of 400 °C for 10 minutes, the annealing is done by a furnace. The temperature and the duration of the annealing are determined so as not to damage the samples during the dehydrogenation process. The samples are processed by laser right after the annealing by furnace in Figure 5.6. The microscope images shows blistered surface of P doped Si layers deposited by PECVD method and the crystallization is checked by micro Raman spectroscopy and Raman signal could be solely acquired from some regions between the blisters. The furnace annealing method should be performed in a more controlled manner at the threshold the binding energies of hydrogen in the i-a-Si:H for an adequate time. However, this is not easy to maintain these conditions for that a-Si layers with that thickness.

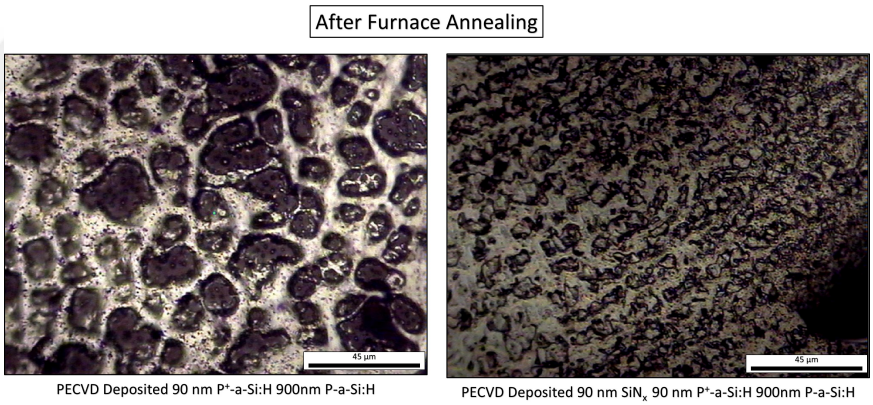

Figure 5.6: Microscope images of the sample after the annealing by furnace

The blistered surface after the LC process gets grayish color which is only made to be contrast with the a-Si layers of PECVD coated layer in Figure 5.7. On the contrary, the color of desired crystallized regions should turn to the color of orange as it have been noticed at the previous sections.

In order to test the endurance of the laser crystallized a-Si layers, the LC processed i-a-Si layers 950 nm thickness are exposed to a dilute solution of 2% HF after it is polished with the polisher of 40 nm Silica. The HF cleaning process lasts for

Figure 5.7: Color of LC processed PECVD deposited a-Si layer

8 minutes overall with the sample immersions for the periods of 20 seconds without any ultrasonic cleaning. The polishing process is almost not able to damage the layers which are scanned with the Q-factors more than 70%. For 1050 nm LC i-a-Si lines of Sample 2 (See Figure 4.31), the cleaning is done lasted for 15 minutes overall with the sample immersions for the periods of 3 minutes by the same HF concentration. And the LC processed lines endure against the etching effect of HF. As it is seen in the microscope and SEM images of these lines that the solution is not able penetrate through the LC processed regions. This is also an evidence that the cracks, which are observed at the interface between the glass substrate and the Si film, did not emerge through the Si layer and it did not affect the surface morphology of the LC i-a-Si regions. Any objective judgment cannot be made, since the polishing is done by hand.

CHAPTER 6

DEVICE DESIGNS ON LASER CRYSTALLIZED THIN SILICON FILMS

In this chapter, several types of attempted device designs are detailed and solutions to encountered problems are provided. Initially two types of homojunction device are fabricated, tested and subsequently, device plans for heterojunction devices are developed. Since improvements became available gradually while working on devices, the final designs are decided to be heterojunction devices, hence further optimizations are developed for only heterojunction devices.

6.1 Homojunction device trials

The homojucntion devices are designed in two different configurations as shown in Figure 6.1. In the first configuration Boron (B153) P dopant is brought on e-Beam deposited i-a-Si film by applying spin-on coating and subsequently a phosphorous (P508) N dopant is brought on the same 950 nm thick i-a-Si film for forming a p-n junction. Spin-on coating is applied in two steps; first 500 RPM for 5 seconds and second 3000 RPM for 20 seconds. Before performing LC, the samples are baked at 200 °C for 5 minutes. Both configurations are processed via laser in order to crystallize the a-Si layer and let dopants to diffuse into the 950 nm i-a-Si during the LC process.

After LC, the samples are examined via SEM (see Figure 6.2) and Raman spectroscopy is performed (see Figure 6.3).

In Figure 6.2, the inset images of the macroscopic views show some delamination of films after laser process. There also occur some inhomogeneous scan effects which form during the line focus scan. The line focus scan direction is formed in vertical

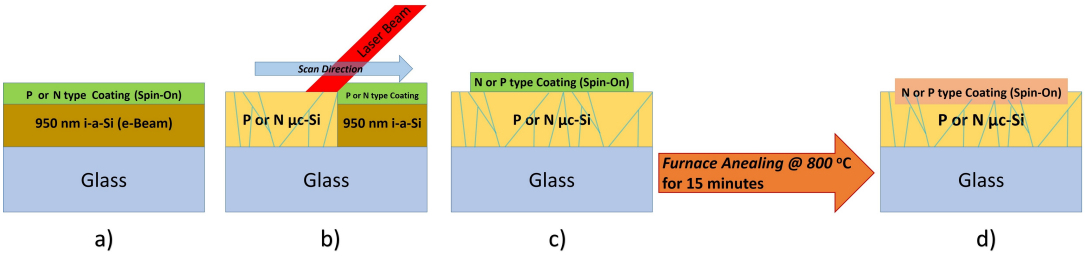

Figure 6.1: Homojunction Device Design

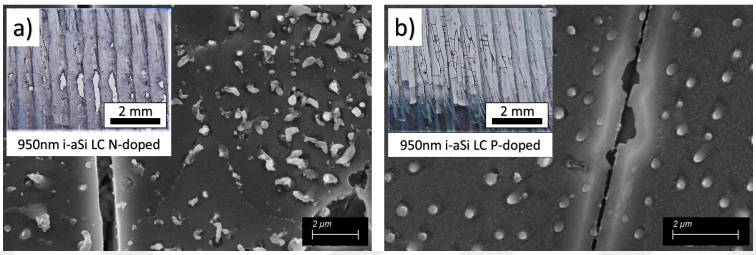

Figure 6.2: SEM images of LC processed 950 nm thick films (the inset images are actual photos)

direction with respect to the images. The consecutive line scans positioned side by side are also overlapped by 40%. This line scan overlap is designated as Q_L which is also called as line scan Q-factor. Q_L factor of 40% can be perceived as the scan central axis, which is in parallel with the scan direction of the line focus, is shifted 600 μm to a side if the line focus is to be the width of 1000 μm as an example. The samples, shown in Figure 6.2, are scanned with the parameters of v_s = 23 mm/s (Q-Factor= 99.5%), effective fluence: 0.36 J/cm^2, and Q_L=40%. The Raman signals confirm that the crystallization occurs after the spin-on coatings are performed (see Figure 6.3). However, how much dopant material is made to diffuse through the i-a-Si layer is not confirmed by SIMS. Analyses of the Raman spectra show that the laser processed specimen with P dopant (which is labeled as 950 nm i-a-Si LC P-Doped in Figure 6.3) metaphase of Si film can be seen, i.e., the transition from amorphous phase to crystal phase of Si. The Raman signal of that exhibits larger wings at the both side of the Raman peak. This is a sign that shows crystallinity occurs partially.

Then conjugate dopant materials (if the firstly coated dopant is N, then conjugate P dopant would be applied.) are spin-on coated again over the laser processed surfaces. All specimens are coated with the conjugate dopant materials via Spin-on method in

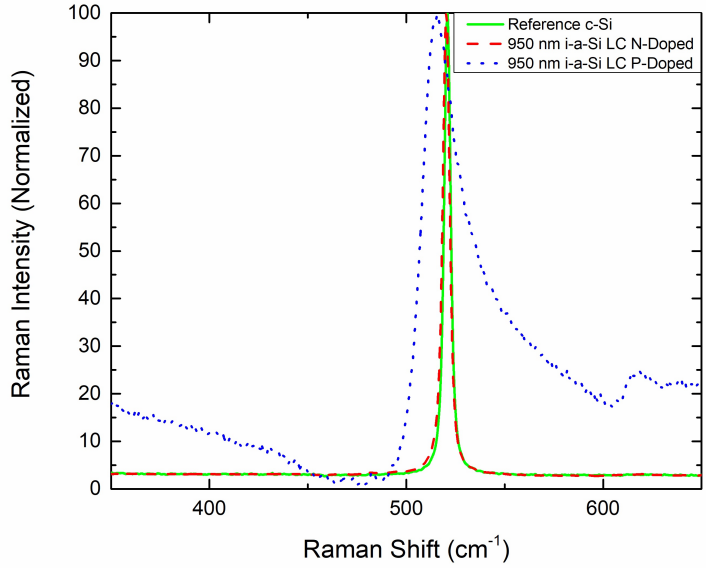

Figure 6.3: Raman spectra of the laser processed samples of 950 nm i-a-Si coated with spin-on dopants

two steps; firstly 500 RPM for 5 s and then 3000 RPM for 20 s. All samples are masked with thermal tape and baked in a furnace at 200 °C for 5 minutes again. They are annealed in order to make the dopant diffuse into the LC processed layers. After the secondly coated conjugate dopant, the device structures are annealed at 800 °C for 15 minutes.

In addition to those specimens, two more specimens are prepared with an intermediate dielectric layer (IDL) of 80 nm SiN_x and the thickness of 1250 nm i-a-Si. These extra samples are used in order to find out any effect of IDL on the homojunction devices. The only difference in laser processing parameters is Q_L factor which is 30%. Figure 6.4 shows SEM and macroscopic images of the samples just after they are treated by the laser process.

The photo response tests and Suns V_{oc} measurements are done for these homojunction device trials. The contacts are taken on the surfaces of the LC processed regions and the secondly spin-on coated regions, which include the conjugate dopants of the LC processed regions. Unfortunately, they are failed and no response is detected. The reason of this failure can be attributed to the improper doping at emitter regions. Since the SIMS measurements have not been acquired and the junction depths are not

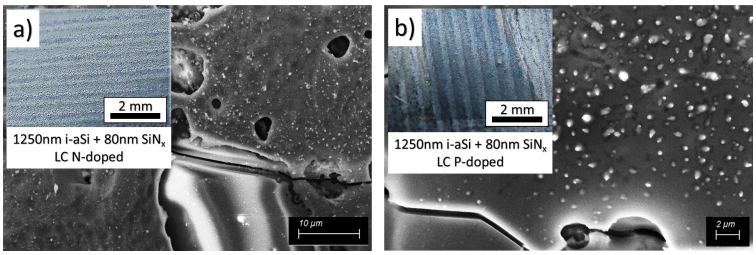

Figure 6.4: SEM images of the laser processed samples of 1250 nm i-a-Si and 80 nm SiN_x (the inset images are actual photos)

known, it would not be right to comment on this issue. Only the middle of the surface could be said to be doped by looking the Raman signals of the samples just after the LC processes.

Since these homojunction device trails did not exhibit any improvements, heterojunction device trails are processed in detail. This strategy allowed to observe photo response more easily and improvement could be done quickly.

6.2 Heterojunction device trials

Here a discussion on heterojunction device designs and their optimizations are provided. In this section, the heterojunction devices with various IDLs are examined and the effects of IDLs are compared and examined qualitatively and quantitatively.

Firstly, 6 different heterojunction device structures are designed (see Figure 6.5). The only one device structure is completely different (see Figure 6.5, I). The other 5 structures (see Figure 6.5, II-VI) have same structural designs that the thin films are deposited directly on the glass substrates. These 5 designs only differ from each other with respect to two layers which are between the glass substrate and the P doped amorphous silicon (P-a-Si) layer. These designs have 2 different layers are shown in Figure 6.5, II-VI. The process flows are also given in Figure 6.5 in detail. In the figure, the deposition techniques of the thin films are given in parenthesizes on the devise figures and the processes of LC, deposition, furnace annealing and metallization are shown and the thicknesses of the different layers are denoted separately. Before moving onto the detailed examination of the designed structures, the two of

the designed structures result in some intrinsic problems which cannot be overcome. The amorphous layers of the two structures are deposited via PECVD and they have different layers between the P^+-a-Si and the glass substrate (see Figure 6.5, V-VI). Sample V has SiN_x and Sample VI has Al:ZnO (AZO) as the intermediate dielectric layers (IDLs). During the LC process, they get damaged drastically. The LC processed layer of Sample V delaminate because of the dehydrogenation and the P-a-Si exhibits bubbly effects which have been discussed in the previous section. Sample VI exhibits sudden delamination due to the properties of AZO which cannot endure the laser irradiation and the heat accumulation on the amorphous layers, ablation of AZO begins and pops the layers, above, off. LC is not able to be constituted in the range of the laser parameters. The damaged samples V and VI can be examined in Figure 6.6.

Now let's discuss the devices, which do not show any intrinsic damage effect during the LC processes. In Figure 6.5, devices I-IV are constructed and tested. Firstly, the sheet resistances and Raman peaks' parameters of the LC processes layers are measured as they are given in Table 6.1. The Raman analyses of these devices are given in Figure 6.7.

Table 6.1: Measurements values of the device properties

LC Processed Surface	Raman Peak Position (cm^{-1})	FWHM of Raman Peak (cm^{-1})	Sheet Resistance ($\Omega/\square$)
e-Beam Deposited without SiN_x	520	5.0	44.8×10^3
e-Beam Deposited with SiN_x	520	6.3	525.3×10^3
PECVD Deposited without SiN_x	No Raman Signal	No Raman Signal	201.4
PECVD Deposited with SiN_x	No Raman Signal	No Raman Signal	$>1 \times 10^7$
PECVD Deposited with N-c-Si Wafer	No Raman Signal	No Raman Signal	6.8
Reference i-c-Si	521	3.9	$>200 \times 10^3$

The samples, which are deposited via PECVD, do not exhibit any crystallization. The surface of these specimens get grayish bubbly structures as they are explained in Chapter 5. Even if these sample are not crystallized as they are intended, they are employed in device fabrications regarding their sheet resistances. Having deposited

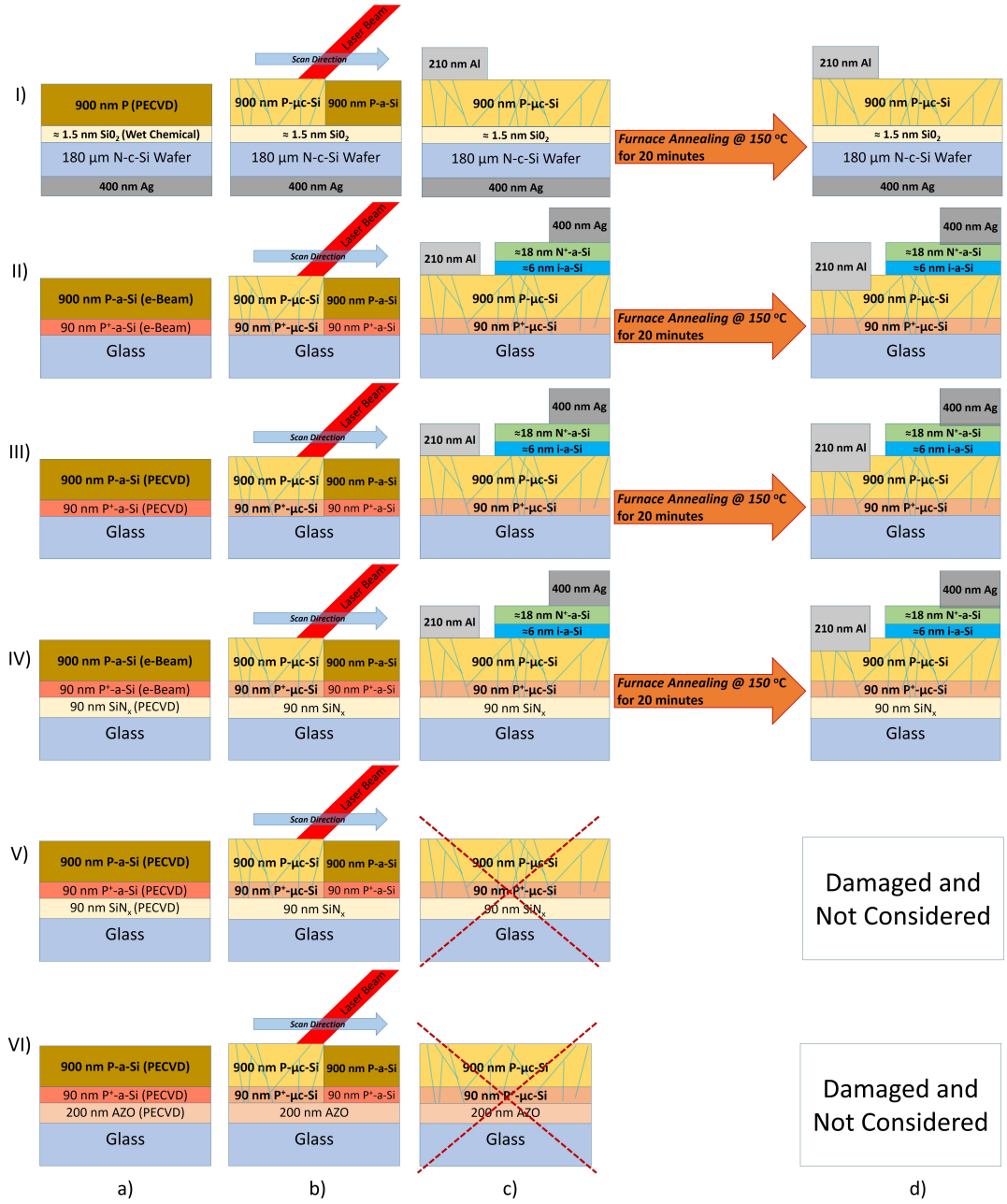

Figure 6.5: 6 different heterojunction device structures

$\sim$ 6 nm i-a-Si passivization layers and $\sim$ 18 nm N^+-a-Si layers on the LC processed layers via PECVD method respectively, the contacts are formed. Subsequently, the annealing is applied by a furnace for 20 minutes at 150 °C. This annealing procedure makes the metal contacts diffuse into the films where the contacts are formed. The real images for the four devices are given in Figure 6.8. The photo active regions are between the Ag and Al contacts for the images of Figure 6.8a-6.8c.

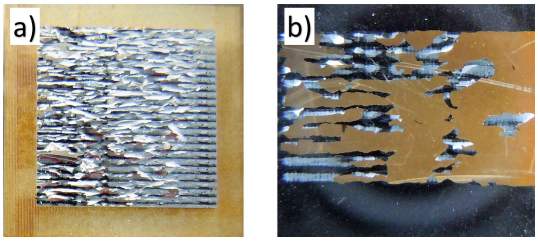

Figure 6.6: Damaged structures after LC process; a) Sample V and b) Sample VI

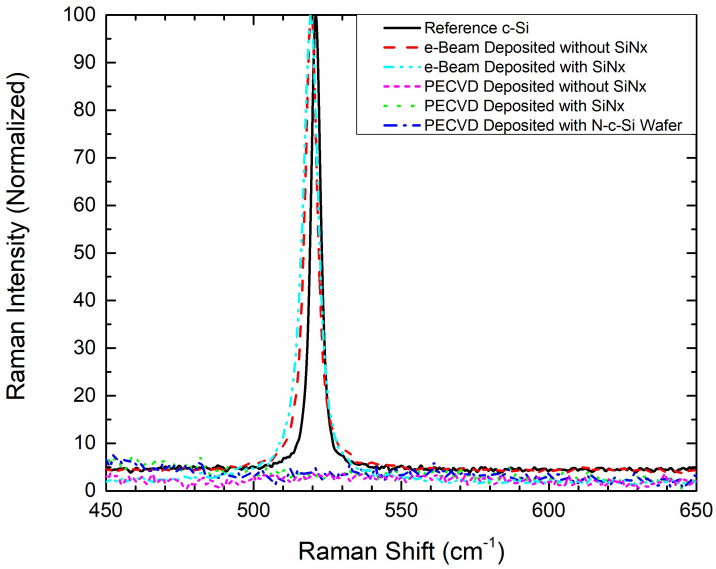

Figure 6.7: Raman spectra of the constructed devices

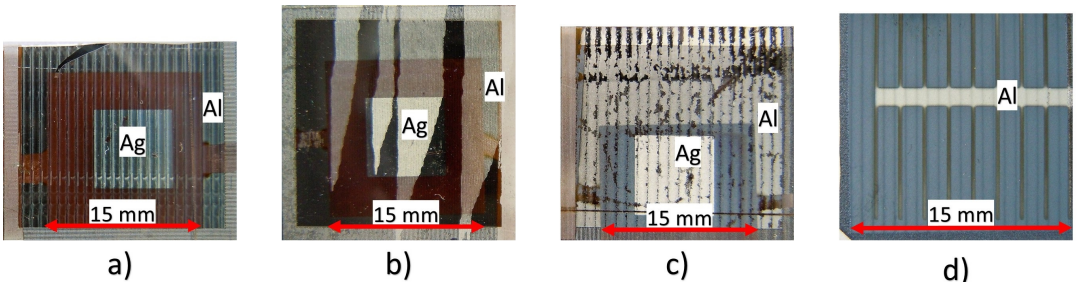

Figure 6.8: Heterojunction device images a) e-Beam deposited without SiN_x , b) e-Beam deposited with SiN_x , c) PECVD deposited without SiN_x , d) PECVD deposited with N-c-Si Wafer

The devices, e-Beam deposited without SiN_x, and PECVD deposited N-c-Si wafer, exhibits photo response (see Figure 6.8a and 6.8d, respectively.). However, no re-

sponse are able to be observed for the other two. The current-voltage (IV) curves of the samples, which are deposited by e-Beam without SiN_x and by PECVD on N-c-Si wafer, are acquired as in Figure 6.9 and Figure 6.10, respectively.

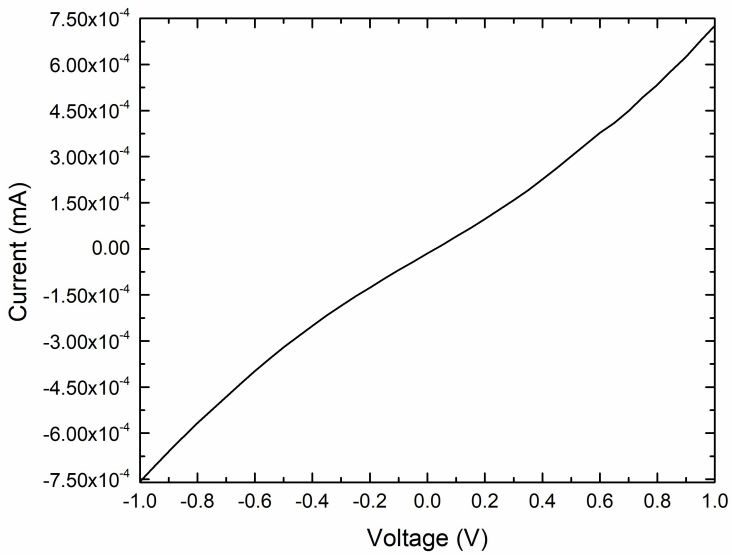

Figure 6.9: I-V curve of the sample, deposited by e-Beam method without SiN_x

The IV curve traces a slight curve that resembles to a diode properties without illuminating the sample in Figure 6.9. This diode characteristics are also observed for the sample, prepared by PECVD method on N-c-Si wafer as in Figure 6.10 clearly with/without illuminating the sample.

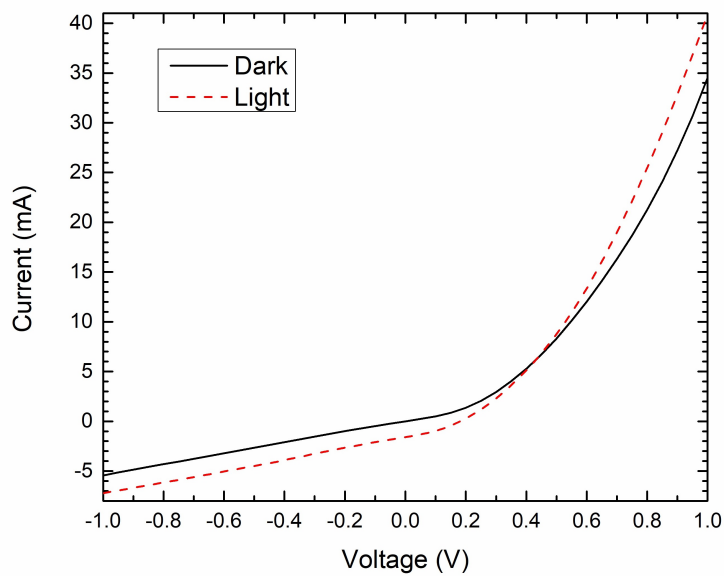

Figure 6.10: I-V curve of the sample, prepared by PECVD method on N-c-Si wafer without/with illuminating (labelled as Dark/Light) the sample

Besides, the sample, which is deposited by e-Beam method without SiN_x, is tested by a solar simulator and efficiency (η) and fill factor (FF) are measured as in Figure 6.11.

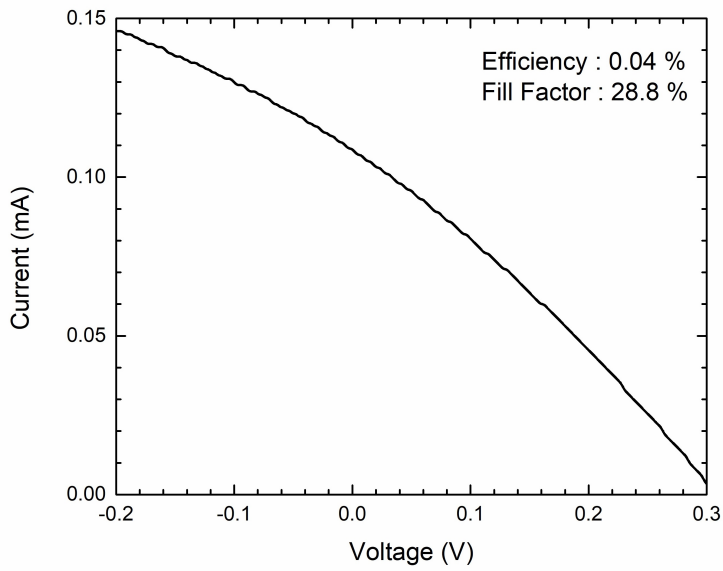

Figure 6.11: Solar simulator measurement of the sample, deposited by e-Beam method without SiN_x

The findings are not good enough to keep up with literature values of these types of devices, but they are promising. So the following device fabrication strategy is built upon the methods that shows the photo responses for the samples prepared by employing e-Beam technique.

The second fabrication plans of the heterojunction devices are as in Figure 6.12 and Figure 6.13.

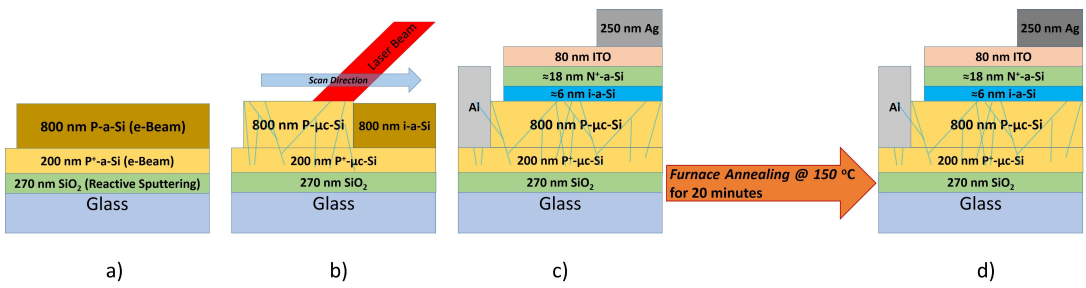

Figure 6.12: Heterojunction device design with 1 μm of P^+- P layer

As it seed in Figure 6.12 and Figure 6.13, the layer deposition techniques are specified

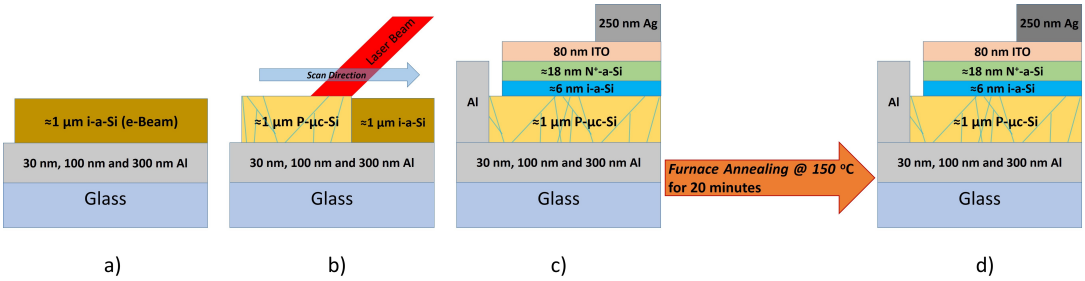

Figure 6.13: Heterojunction device design with 30 nm, 100 nm and 300 nm of Al layers

next to the labels of the layers. The LC process is took place at the figures, labeled as b. Crystallinity of all LC processed surfaces are verified by Raman spectroscopy. Three different Al thicknesses are applied for Figure 6.13. On the other hand, the device structures are identical. The Al layers are also expected to be as dopant material for the P junction after the LC process. Photo-sensitive regions (active regions) lay between the metal contacts. The constructed devices are given in Figure 6.14. The active regions have 12.6 mm^2 and 17 mm^2 for the device with 1 μm of P$^+$- P layer and the device with Al layers, respectively.

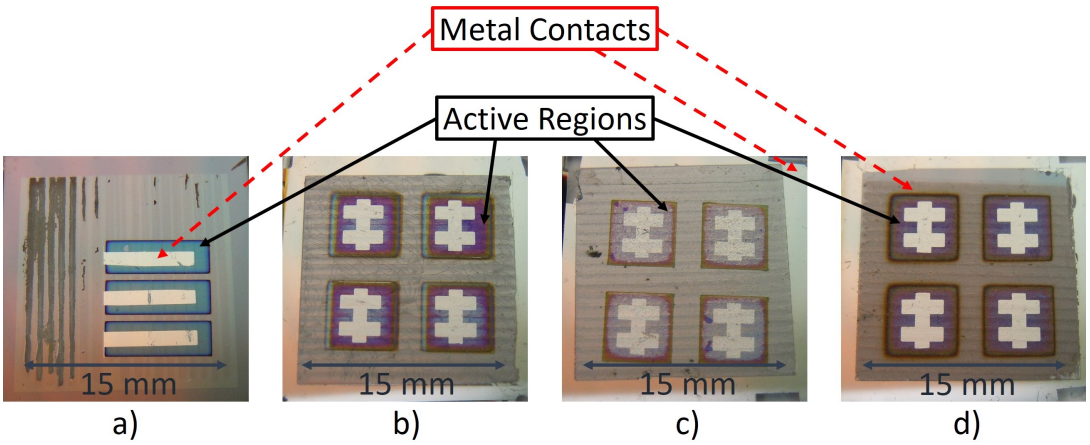

Figure 6.14: The constructed devices: a) Device with 1 μm of P$^+$- P layer; b) Device with 30 nm Al layer; c) Device with 100 nm Al layer; d) Device with 300 nm Al layer;

An Al square rim encloses outermost of the each device. The sample, with 1 μm of P$^+$- P layer, constitutes of three identical devices on itself and the samples, with Al layers, have four identical devices on themselves. The Ag contact is shiny grayish

region and it lays at the center of the each devices as shiny strips for Figure 6.14a and vertically slanted "H" for Figure 6.14c-d. Regions which are between all devices are shaded to be no contact occurrence.

The IV curves of the each type of device are acquired under light and in dark in order to explore the diode-like feature and the photo-response.

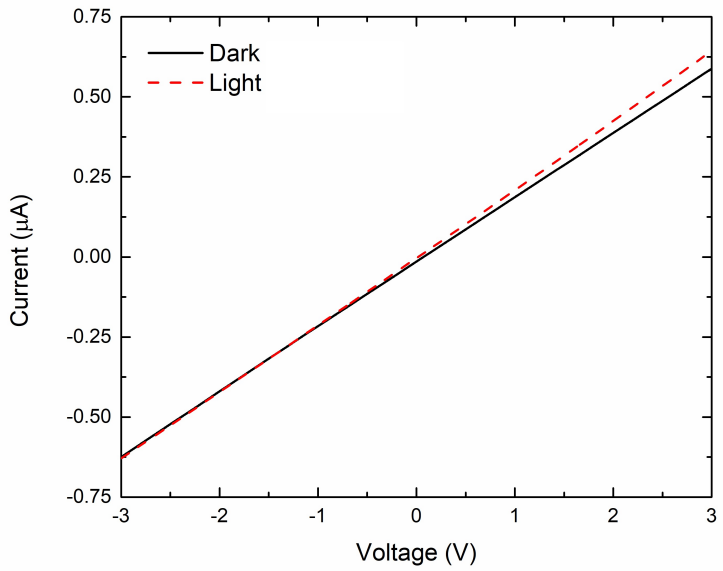

Figure 6.15: The IV curves of the device, with 1 μm of P^+- P layer

The IV curves of the sample device of 1 μm of P^+- P layer does not exhibit any diode characteristics. There is only linear relation in current and the applied voltage and that is just a device like a resistor (see Figure 6.15). There is a slight difference between the curves under light and in the dark situations. That can only be attributed to a short circuit which occurs though the junction.

On the contrary, the IV curves of the sample device of 30 nm layer shows S-shaped curves and those curves diverge from each other under light (see Figure 6.16). The red curve represents the behavior of the device under illumination of AM 1.5G. The divergence of the curve is a promising sign of a photo-sensitive device.

The IV curves of the sample device of 100 nm layer does not exhibit S-shapes as much as the sample device of 30 nm layer does. The separation between the curves, which are under the light and in the dark, are not as much as that of the sample, in

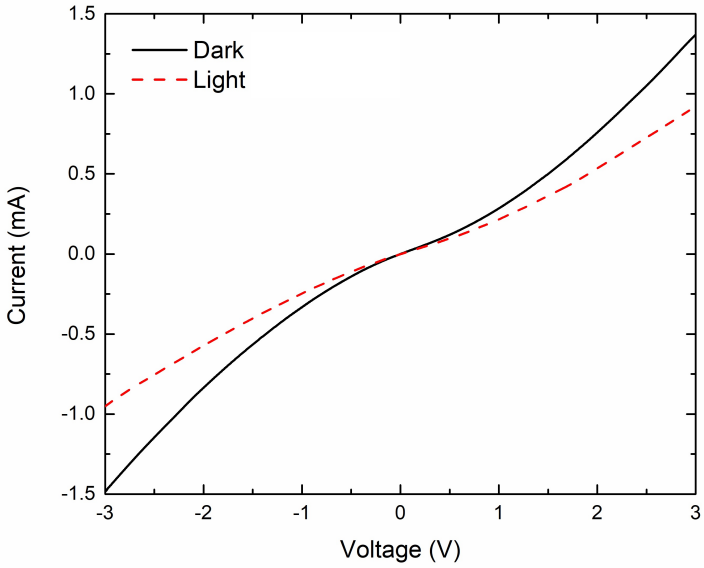

Figure 6.16: The IV curves of the device, with 30 nm Al layer

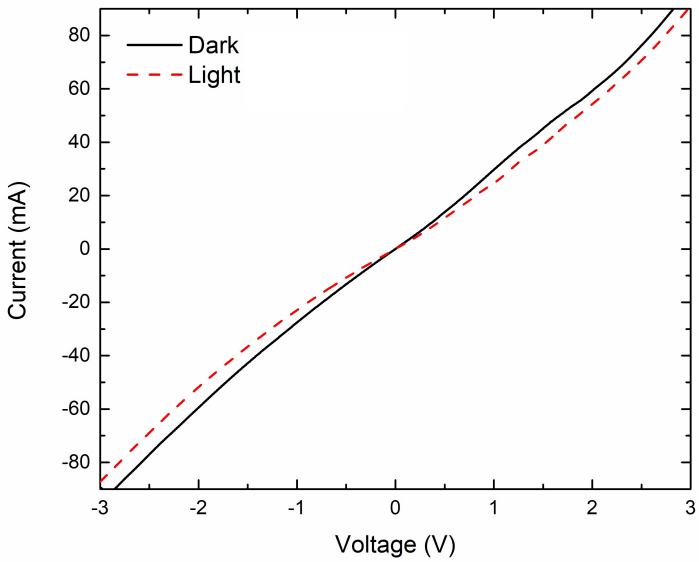

Figure 6.17: The IV curves of the device, with 100 nm Al layer

Figure 6.16. The Al content which has been emerged to the surface of the LC Si layer can cause this ohmic behavior of the device. In order to assure ourselves, it is enough to examine Figure 6.18. In case the Al content is made to be delivered to the surface more, the device becomes ohmic or a short circuit.

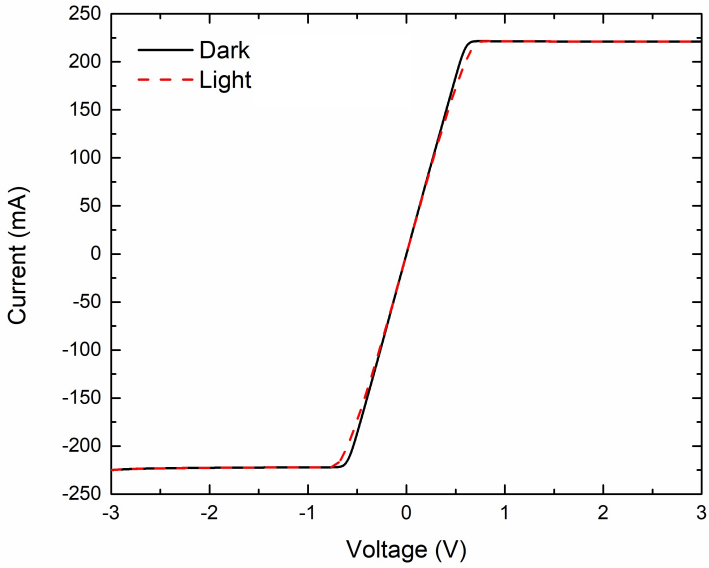

Figure 6.18: The IV curves of the device, with 300 nm Al layer

The sample device of 300 nm Al layer behaves like a resistor in the voltage range between -0.5 V and 0.5 V as it is seen in Figure 6.18. The curves, under light and in the dark, trace out the same current-voltage values. This device has no photo-response feature. Increase in Al content, at the bottom surface of the device, makes Al diffuse into the LC processes Si film and that makes a short circuit.

CHAPTER 7

CONCLUSIONS AND DISCUSSIONS

In this thesis work, laser crystallization (LC) of e-beam evaporated a-Si thin films at room temperature is investigated in detail with different laser parameters to explore how the crystallinity on the surface of the sample changes in relation to several process parameters. The deposition method is purposefully selected to be e-beam evaporation because the most common alternative method of plasma enhanced chemical vapor deposition leads to substantial hydrogenation of the film due to hydrogen content of the typical precursor gases. The hydrogen in the a-Si layer, unless let to thermally diffuse out above 500 °C for hours, causes blistering during LC, rendering films useless. In this thesis, our main motivation is to achieve demonstrating fabrication of thin, device quality crystalline Si films at a low energy budget by exploiting the process control capabilities offered by a pulsed laser. Hence, long thermal preconditioning of the films are deliberately avoided.

The crystallization is performed via an IR nanosecond pulsed laser and it is tested to verify if the required energy per area for crystallizing the film consistently matches the calculated values. These values are expected to lie between the required energy levels for liquefication and evaporation of various thicknesses of a-Si layers (see Section 4.2). The effects of the intermediate dielectric layers are investigated in order to improve the degree of crystallization which expresses itself by enlargement of the crystallite grain size (see Section 3.3). The details of the intermediate dielectric layer effects are discussed and compared to a previous work [73]. It is shown that SiO_2 and ZnO as intermediate dielectric layers exhibit a good performance in this respect.

In Chapter 3, my investigation shows that appropriate ILD use is important for increasing the crystalline grain size and relieving the tensile stress over the grains; in

which SiO_2 and ZnO perform a good performance regarding those issues. The red-shifts of the Raman peaks of LC Si film on SiO_2 and ZnO do not exceed 3 cm^{-1} with respect to bulk Si and this shift in the Raman peak position corresponds to 0.75 GPa which is maximum tensile stress between the crystalline grains. The cause of the stress reduction can be attributed to restraining of heat diffusion through the IDL layers. The thermal conductivity values of those IDLs are lower than that of SiN_x for comparison.

In Chapter 4, the study on a-Si thickness and its effects show that the crystallinity does not change significantly with varying film thickness. On one hand, any thickness of a-Si can be used, in case a suitable laser fluence is applied. On the other hand, the overlap ratios of the laser pulses have great impact on the quality of the LC process. The limitation of heat accumulation on local regions and maintained slow quenching of the l-Si maintains EC and that forms longer crystalline domains which exceed 2 mm in length. The longer grains also provide lower sheet resistance through the surface of the laser crystallized Si. The sheet resistance is decreased by a factor of 10^7 by increasing the overlap ratios of the laser pulses. If the effective fluence is kept at a value close to 0.2 J/cm^2 and the ratio of overlap is set a value close to 99.9% for a pulse duration of 200 ns at wavelength of 1064 nm, the crystal grain sizes can be enlarged. It should be kept in mind that if the laser focus is stretched in width perpendicular to the scan direction, it will also have a great contribution to augment the grain sizes far beyond several millimeters.

In Chapter 6, I show that the optimized values of the laser parameters and the optical design let me develop device grade junctions. Diode-like structures can be processed *in situ* over chips in any patterns. Moreover, the costs of fabrication can be reduced due to absence of pretreatment and absence of preheating of the thin film solar cells. The ultra-thin (below a thickness of 1 μm) Si films can be employed over great variety of substrates. The key point is to determine which laser process parameters are suitable for which types of IDLs and substrates.

In previous works, explosive crystallization was studied by experiments and simulations. Due to inadequacy of the experiments to analyze the explosive crystallization in a microscopical and time resolved manner, the simulations were performed in quasi

1D (one dimension including the thickness of the film) domains in order to study the effects of the thicknesses of Si layer and the substrates. However, quasi 2D (two dimensions including the thickness of the film) simulations have not been performed. Moreover, the overlap ratios of the laser pulses have not been investigated in these previous works, but the explosive crystallization of a single pulse and its evolution were investigated. In this thesis work, a detailed study on pulse overlap is performed and the effects of heat accumulation at the surface is examined in detail (see Section 4.3). In the light of this study, quasi 2D simulations can be performed and the evolution of the explosive crystallization can be revealed and verified in a future study. As another future prospect, the influences of the overlapping laser pulses can be studied by computer simulations and compared with the experimental outcomes of this current work. In further simulation based studies, the overlap of the laser pulses can be performed by modifying the source term in Equation (2.13) and replacing the term $I_0(t)$ with $I_0(x,t)$. The $I_0(x,t)$ in source term can be used to represent the overlapping laser pulses and as a result the heat accumulation on the film surface and controlled quenching of the l-Si layers can be studied computationally. The term $I_0(x,t)$ can contain the time and spacial dependency of the laser illumination this way.

The theory of EC gives some hints on how long a pulse duration should be chosen for LC process. Considering that a time interval of $\sim 10^{-11}$ s is necessary to thermalize intrinsic electrons and to heat up the Si, the laser pulse duration should be set longer than this time interval in order to maintain EC. As a result, it can be inferred that the nanosecond pulsed lasers are the most appropriate tools and they are also capable of great adjustment range. Since the velocity of the boundary propagation is not lower than a value of 10 m/s in EC, the scan speed should be kept at a lower value in order to maintain the slow quenching of the l-Si for LC. In this study, it is shown that all successful LC processes are performed below the EC boundary propagation velocity.

The research in Section 4.3 also contains the effect of line focus irradiation. The comparison between the spot focus and the line focus can be done easily in view of the previous 3 chapters. The line focus is found to be more adequate for accumulating heat in larger areas than that of the spot focus. As a result of this, lateral heat accumulation through the line focus lets the grains grow up to 2 mm. It should be noted that, 2 mm is not a fundamental limit but it is a practical limit of this work which reflects

the size of the employed cylindrical lens and maximum pulse energy of the laser. It can be deduced that the dimensions of the crystallites can be enhanced by elongating the line focus and thereby by increasing the lateral heat accumulation along the width of the scan direction.

An improvement can be suggested for line focus scan for the crystallinity of the Si layers. This improvement can be performed by replacing the cylindrical lens with a Powell lens which resembles an axicon lens in cylindrical analogy, i.e., it has a triangular edge rather than a cone tip. If the Powell lens is positioned like the cylindrical lens under the laser beam and the beam is made to scan throughout the apex edge of the Powell lens, the incoming gaussian beam can be turned into a homogeneous flat top beam. The beam can be widened up to a fan angle of 90°. This fan angle determines how much the beam can be refracted from one edge to another of the outgoing beam that emerges from the base of the Powell lens. The difference between a cylindrical lens and a Powell lens is shown in Figure 7.1.

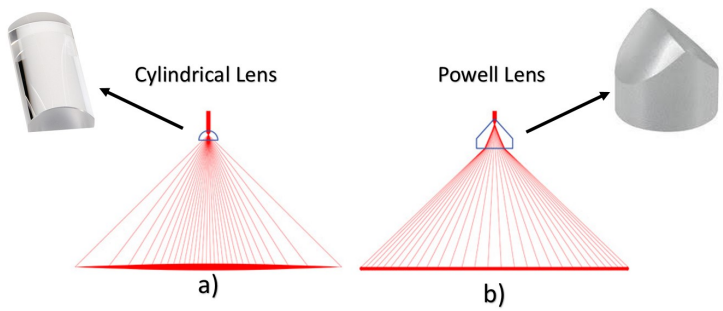

Figure 7.1: Cylindrical Lens vs. Powell Lens [74]

In Figure 7.1b, the angle between the lines connecting the edges at inside of the Powell lens, is the fan angle. A gaussian beam profile can be converted to a flat-top gaussian. This way, power homogeneity can be maintained through the illuminated area of the line focus. The defects can be reduced (see Chapter 5) and the crystallinity can be improved.

The heterojunction device designs can also be improved in order to fabricate better ultra-thin solar cell applications. The optimization and maximization of the efficiency of a solar cell is another subject which is a very deep and complex task. This task necessitates a work load that can be the subject of another thesis work. However, further improved ultra-thin c-Si solar cell designs can be done in the light of this work (see

Section 6.2). Optimization of semiconductor stacks, anti-reflection coatings and surface texturing and optimized metal contacts will result in higher values of efficiency for an ultra-thin c-Si solar cell based on LC thin Si film.

Laser crystallization process has typically been conducted at elevated temperatures of substrates and has utilized continuous wave light sources to avoid defects and attain solar cell quality $\sim 10\ \mu$m thick films. There has been a need to process the films at the room temperature. The laser crystallization process with infrared irradiation has been typically sustained with optical power in kW ranges. There has been a need for lower process power for reduced fabrication cost. In solar cells, thicknesses of deposited a-Si films have resided in the range of tens of micrometers. There has been a need for ultra-thin Si solar cells for reduced use of Si source. In this dissertation, the main motivation is to reduce the fabrication cost of c-Si films for the applications of ultra-thin solar cells by performing *in situ* laser crystallization at room temperatures. Here, the elevated substrate temperatures and kilowatts of laser powers are avoided and several improvements on crystallinity is successfully achieved via use of IR nanosecond pulsed lasers.

These achievements can further be improved by optimizing the laser scan systems in larger scales in order to produce ultra-thin c-Si solar cell and thin film transistor applications at an industrial scale in the future.

REFERENCES

[1] N. H. Nickel, *Laser Crystallization of Silicon*, vol. 75 of *Semiconductors and semimetals*. The Netherlands: Elsevier Academic Press, 1st ed., 2003.

[2] J. R. Brotherton, J. R. Ayres, and N. D. Young, "Characterization of low temperature poly-Si thin film transistors," *Solid-State Eletron.*, vol. 34, no. 7, pp. 671–679, 1991.

[3] O. Nast, T. Puzzer, L. M. Koschier, A. Spproul, and S. R. Wenham, "Aluminum-induced crystallization of amorphous silicon on glass substrates above and below the eutectic temperature," *Appl. Phys. Lett.*, vol. 73, no. 22, pp. 3214–3216, 1998.

[4] D. Song, D. Inns, A. Straub, M. L. Terry, P. Campbell, and A. G. Aberlee, "Solid phase crystallized polycrystalline thin-films on glass from evaporated silicon for photovoltaic applications," *Thin Solid Films*, vol. 513, no. 1–2, pp. 356–363, 2006.

[5] E. S. Cielaszyk, K. H. R. Kirmse, R. A. Stewart, and A. E. Wendt, "Mechanisms for polycrystalline silicon defect passivation by hydrogenation in an electron cyclotron resonance plasma," *Appl. Phys. Lett.*, vol. 67, no. 21, pp. 3099–3101, 1995.

[6] A. Slaoui, A. Chowdhury, P. Prathap, Z. Said-Bacar, A. Bahouka, and F. Mermet, "Laser processing for thin film crystallization silicon solar cells," *Proc. of SPIE*, vol. 8473, no. 384730C, pp. 1–7, 2012.

[7] M. Kahraman, O. T. Ozmen, S. H. Sedani, E. Ozkol, and R. Turan, "Effects of glass substrate coated by different-content buffer layer on the quality of poly-Si thin films," *Phys. Status Solidi*, vol. A, pp. 1–8, 2016.

[8] K. Toko, M. Nakata, A. Okada, M. Sasase, N. Usami, and T. Suemasu, "Influence of substrate on crystal orientation of large-grained Si thin films formed by metal-induced crystallization," *Int. J. Photoenergy*, vol. 2015, no. 790242, pp. 1–7, 2015.

[9] O. T. Ozmen, A. Slaoi, S. Roques, and D. Ballutaud, "Solid phase epitaxy on N-type polysilicon films formed by aluminium induced crystallization of amorphous silicon," *Thin Solid Films*, vol. 517, no. 23, pp. 6358–6363, 2009.

[10] P. Dogan, B. Gorka, L. Dcheller, I. Sieber, F. Fenske, and S. Gall, "Low-temperature epitaxy of silicon by electron beam evaporation," *Thin Solid Films*, vol. 515, no. 19, pp. 7643–7646, 2007.

[11] D. Van. Gestel, I. Gordon, H. Bender, D. Saurel, J. Vanacken, G. Beaucarne, and J. Poortmans, "Intragrain defects in polycrystalline silicon layers grown by aluminum-induced crystallization and epitaxy for thin-film solar cells," *J. Appl. Phys.*, vol. 105, no. 114507, pp. 1–11, 2009.

[12] D. Van. Gestel, P. Dogan, I. Gordon, H. Bender, K. Y. Lee, G. Beaucarne, S. Gall, and J. Poortmans, "Investigation of intragrain defects in pc-Si layers obtained by aluminum-induced crystallization: comparison of layers made by low and high temperature epitaxy," *Mat. Sci. Eng. B.*, vol. 159–160, pp. 134–137, 2009.

[13] J. Dore, R. Evans, U. Schebert, B. D. Eggleston, D. Ong, K. Kim, J. Huang, O. Kunz, M. Keevers, R. Egan, S. Varlamov, and M. A. Green, "Thin-film polycrystalline silicon solar cells formed by diode laser crystallisation," *Prog. Photovolt: Res. Appl.*, vol. 21, no. 6, pp. 1377–1383, 2013.

[14] M. Weizman, H. Rhein, J. Dore, S. Gall, C. Klimm, G. Andra, C. Schultz, F. Fink, B. Rau, and R. Schlatmann, "Efficiency and stability enhancement of laser-crystallized polycrystalline silicon thin-film solar cells by laser firing of the absorber contacts," *Sol. Energy Mater. Sol. Cells*, vol. 120, pp. 521–525, 2014.

[15] M. Weizman, H. Rhein, K. Bhatti, R. Duman, C. Schultz, M. Schule, O. Gabriel, S. Ring, S. Kirner, C. Klimm, M. Nittel, S. Gall, B. Rau, B. Stannowski, R. Schlatmann, and F. Fink, "Rear-side all-by-laser point-contact scheme for liquid-phase-crystallized silicon on glass solar cells," *Sol. Energy Mater. Sol. Cells*, vol. 137, pp. 280–286, 2015.

[16] J. Haschke, D. Amkreutz, T. Frijnits, S. Kuhnapfel, T. Hanel, and B. Rech, "Influence of barrier and doping type on the open-circuit voltage of liquid phase-crystallized silicon thin-film solar cells on glass," *IEEE J. Photovoltaics*, vol. 5, no. 4, pp. 1001–1005, 2015.

[17] J. Dore, S. Varlamov, and M. A. Green, "Intermediate layer development for laser-crystallized thin-film silicon solar cells on glass," *IEEE J. Photovoltaics*, vol. 5, no. 1, pp. 9–16, 2015.

[18] O. Gabriel, T. Frijints, S. Calnan, S. Ring, S. Kirner, A. Opitz, I. Rothert, H. Rhein, M. Zelt, K. Bhatti, J. H. Zollondz, A. Heidelberg, J. Haschke, D. Amkreutz, S. Gall, F. Friedrich, B. Stannowski, B. Rech, and R. Schlatmann, "PECVD intermediate and absorber layers applied in liquid-phase crystallized silicon solar cells on glass substrates," *IEEE J. Photovoltaics*, vol. 4, no. 6, pp. 1343–1348, 2014.

[19] P. Sonntag, J. Haschke, S. Kuhnapfel, O. Gabriel, D. Amkreutz, and B. Rech, "Properties of liquid phase crystallized interdigitated back-contact solar cells on glass," *Energy Procedia*, vol. 77, pp. 487–492, 2015.

[20] G. Andra, J. Bergmann, and F. Falk, "Laser crystallized multicrystalline silicon thin films on glass," *Thin Solid Films*, vol. 487, pp. 77–80, 2005.

[21] D. Amkreutz, W. D. Barker, S. Kuhnapfel, P. Sonntag, O. Gabriel, S. Gall, U. Bloeck, J. Schmidt, J. Haschke, and B. Rech, "Liquid-phase crystallized silicon solar cells on glass: increasing the open-circuit voltage by optimized interlayers for N- and P-type absorbers," *IEEE J. Photovoltaics*, vol. 5, no. 6, pp. 1757–1761, 2015.

[22] J. Haschke, D. Amkreutz, L. Korte, F. Ruske, and B. Rech, "Towards wafer quality crystalline silicon thin-film solar cells on glass," *Sol. Energy Mater. Sol. Cells*, vol. 128, pp. 190–197, 2014.

[23] M. L. Taheri, S. McGowan, L. Nikolova, J. E. Evans, N. Teslich, J. P. Lu, T. LaGrange, F. Rosei, B. J. Siwich, and N. D. Browning, "In situ laser crystallization of amorphous silicon: controlled nanosecond studies in the dynamic transmission electron microscope," *Appl. Phys. Lett.*, vol. 97, no. 032102, pp. 1–3, 2010.

[24] A. Chowdhury, A. Bahouka, S. Steffens, S. Schneider, J. Dore, F. Mermet, and A. Slaoui, "Laser anneling of thin film polycrystaline silicon solar cell," *EPJ Photovoltaics*, vol. 4, no. 45108, pp. p1–p5, 2013.

[25] J. Dore, D. Ong, S. V. R. Egan, and M. A. Green, "Progress in laser-crystallized thin-film polycrystalline silicon solar cells: intermediate layers, light trapping, and metallization," *IEEE J. Photovoltaics*, vol. 4, no. 1, pp. 33–39, 2014.

[26] S. Kuhnapfel, N. H. Nickel, S. Gall, M. Klaus, C. Genzel, B. Rech, and D. Amkreuts, "Preferential {100} grain orientation in 10 micrometer-thick laser crystallized multicrystalline silicon on glass," *Thin Solid Films*, vol. 576, pp. 68–74, 2015.

[27] D. Amkreutz, J. Haschke, T. Haring, F. Ruske, and B. Rech, "Conversion effiency and process stability improvement of electron beam crystallized thin film silicon solar cells on glass," *Sol. Energy Mater. Sol. Cells*, vol. 123, pp. 13–16, 2014.

[28] Y. R. Chen, C. H. Chang, and L. S. Chao, "Modeling and experiment analysis in excimer-laser crystallization of amorphous Si films on a glass substrate with different buffer layers," *J. Am. Cera. Soc.*, vol. 90, no. 3, pp. 688–692, 2007.

[29] W. C. Yeh and M. Matsumura, "Numerical calculation of excimer-laser-induced lateral-crystallization of silicon thin films," *Jpn. J. Appl. Phys.*, vol. 40, no. 2A, pp. 492–499, 2001.

[30] K. A. Jackson and B. Chalmers, "Laser dehydrogenation/crystallization of plasmaenhanced chemical vapor deposited amorphous silicon for hybrid thin film transistors," *Appl. Phys. Lett.*, vol. 64, no. 9, pp. 1132–1134, 1994.

[31] J. S. Im, H. J. Kim, and M. O. Thomson, "Phase transformation mechanisms involved in excimer laser crystallization of amorphous silicon films," *Appl. Phys. Lett.*, vol. 63, no. 14, pp. 1969–1971, 1993.

[32] N. H. Nickel, G. B. Anderson, and R. I. Johnson, "Grain-boundary defects in laser-crystallized polycrystalline silicon," *Phys. Rev. B*, vol. 56, no. 19, pp. 12065–12068, 1997.

[33] R. Z. Bachrach, K. Winer, J. B. Boyce, S. E. Ready, R. I. Johnson, and G. B. Anderson, "Low temperature crystallization of amorphous silicon using an excimer laser," *J. Electron. Mater.*, vol. 19, no. 3, pp. 241–248, 1990.

[34] M. Hatano, S. Moon, M. Lee, K. Suzuki, and C. P. Grigoropoulos, "Excimer laser-induced temperature field in melting and resolidification of silicon thin films," *J. Appl. Phys.*, vol. 87, no. 1, pp. 36–43, 2000.

[35] M. O. Thompson, G. J. Galvin, J. W. Mayer, P. S. Poate, D. C. Jacobson, A. G. Cullis, and N. G. Chew, "Melting temperature and explosive crystallization of amorphous silicon during pulsed laser irradiation," *Phys. Rev. Lett.*, vol. 52, no. 26, pp. 2360–2363, 1984.

[36] R. F. Wood and G. A. Geist, "Theoretical analysis of explosive propagating molten layers in pulsed-laser-irradiated a-Si," *Phys. Rev. Lett.*, vol. 57, no. 7, pp. 873–876, 1986.

[37] K. Murakami, O. Eryu, K. Takita, and K. Masuda, "Explosive crystallization starting from an amorphous-silicon surface region during long-pulse laser irradiation," *Phys. Rev. Lett.*, vol. 59, no. 19, pp. 2203–2206, 1987.

[38] J. W. Christian, *The Theory of Transformations in Metals and Alloys*. Oxford: Elsevier Science Ltd., 3rd ed., 1965.

[39] R. F. Wood, C. W. White, , and R. T. Young, *Pulsed Laser Processing of Semiconductors*. Semiconductors and Semimetals, Orlando: Academics Press Inc., 1984.

[40] D. M. Herlach, "Non-equilibrium solidification of undercooled metallic melts," *Mater. Sci. Eng.*, vol. R12, pp. 177–272, 1994.

[41] K. A. Jackson and B. Chalmers, "Kinetics of solidification," *Can. J. Phys.*, vol. 34, pp. 473–490, 1956.

[42] R. Černý, R. Šášik, I. Lukeš, and V. Cháb, "Excimer-laser-induced melting and solidification of monocrystalline Si: Equilibrium and nonequilibrium models," *Phys. Rev. B*, vol. 44, no. 9, pp. 4097–4102, 1991.

[43] M. D. Kluge and J. R. Ray, "Velocity versus temperature relation for solidification and melting of silicon: A molecular-dynamics study," *Phys. Rev. B*, vol. 39, no. 3, pp. 1738–1746, 1989.

[44] P. A. Stolk, A. Polman, and W. C. Sinke, "Experimental test of kinetic theory for heterogeneous freezing in silicon," *Phys. Rev. B*, vol. 47, no. 1, pp. 5–13, 1993.

[45] A. A. Grinberg, R. F. Mekhtiev, S. M. Ryvkin, V. M. Salmanov, and I. D. Yaroshetskii, "Absorption of laser radiation and damage in semiconductors," *Sov. Phys. - Solid State*, vol. 9, no. 5, pp. 1085–1090, 1967.

[46] R. F. Wood and G. E. Giles, "Macroscopic theory of pulsed-laser annealing. I. Thermal transport and melting," *Phys. Rev. B*, vol. 23, no. 6, pp. 2923–2942, 1981.

[47] M. Born and E. Wolf, *Principles of Optics*. Oxford: Pergamon Press, 6th ed., 1991.

[48] P. Baeri, S. U. Campisano, G. Foti, and E. Rimini, "A melting model for pulsing-laser annealing of implanted semiconductors," *J. Appl. Phys.*, vol. 50, no. 2, pp. 788–797, 1979.

[49] P. Baeri, M. A. Harith, G. Russo, E. Rimini, A. Guiulietti, and M. Vaselli, "Free carrier dynamics and energy transfer to the Si lattice during pico and nanosecond Nd laser pulse irradiation," *Phys. Stat. Sol. B*, vol. 130, pp. 225–233, 1985.

[50] I. Štich, R. Car, and M. Parrinello, "Bonding and disorder in liquid silicon," *Phys. Rev. Lett.*, vol. 63, no. 20, pp. 2240–2243, 1989.

[51] R. Černý, V. Vydra, P. Přikryl, I. Ulrych, J. Kočka, K. El-Kader, Z. Chvoj, and V. Cháb, "Theoretical and experimental studies of a-Si:H recrystallization by XeCl excimer laser irradiation," *Appl. Surf. Sci.*, vol. 86, pp. 359–363, 1995.

[52] R. Černý and P. Přikryl, "Nonequilibrium model of laser-induced phase change processes im amorphous silicon thin films," *Phys. Rev. B*, vol. 57, no. 1, pp. 194–202, 1998.

[53] S. R. Stiffler, M. O. Thompson, and P. S. Peercy, "Nucleation of amorphous germanium from supercooled melts," *Appl. Phys. Lett.*, vol. 56, no. 11, pp. 1025–1027, 1990.

[54] R. Černý, V. Cháb, and P. Přikryl, "A two-phase moving boundary problem with two moving interfaces in laser processing of materials," *Comput. Mater. Sci.*, vol. 8, pp. 228–242, 1997.

[55] F. L. Pedrotti and L. S. Pedrotti, *Introduction to Optics*. New Jersey: Prentice-Hall, Inc., 2nd ed., 1996.

[56] J. Jin, Z. Yuan, L. Huang, S. Chen, W. Shi, Z. Cao, and Q. Lou, "Laser crystallization of amorphous silicon films investigated by raman spectroscopy and atomic force microscopy," *Appl. Surf. Sci.*, vol. 256, no. 11, pp. 3453–3458, 2010.

[57] C. Georgi, M. Hecker, and E. Zschech, "Effects of laser-induced heating on Raman stress measurements of silicon and silicon-germanium structures," *J. Appl. Phys.*, vol. 101, no. 123104, pp. 1–6, 2007.

[58] I. De. Wolf, "Micro-Raman spectroscopy to study local mechanical stress in silicon integrated circuits," *Semicond. Sci. Technol.*, vol. 11, pp. 139–154, 1996.

[59] S. Kouteva-Arguirova, Tz. Arguirov, D. Wolfframm, and J. Reif, "Influence of local heating on micro-Raman spectroscopy of silicon," *J. Appl. Phys.*, vol. 94, no. 8, pp. 4946–4949, 2003.

[60] W. Wei, G. Xu, J. Wang, and T. Wang, "Raman spectra of intrinsic and doped hydrogenated nanocrystalline silicon films," *Vacuum*, vol. 81, pp. 656–662, 2007.

[61] P. Lengsfeld, N. H. Nickel, Ch. Genzel, and W. Fuhs, "Stress in undoped and doped laser crystallized poly-Si," *J. Appl. Phys.*, vol. 91, no. 11, pp. 9128–9135, 2002.

[62] X. Wu, J. Yu, T. Ren, and L. Liu, "Micro-Raman spectroscopy measurement of stress in silicon," *Microelectr. J.*, vol. 38, pp. 87–90, 2007.

[63] W. Wisniewski, C. A. Baptista, M. Muller, G. Volksch, and C. Russel, "Surface crystallization of cordierite from glass studied by high-temperature X-ray diffraction and electron backscatter diffraction (EBSD)," *Cryst. Growth Des.*, vol. 11, pp. 4660–4666, 2011.

[64] H. Seigneur, N.Mohajeri, R. P. Brooker, K. O. Davis, E. J. Schneller, N. G. Dhere, M. P. Rodgers, J. Wohlgemuth, N. S. Shiradkar, G. Scardera, A. C. Rudack, and W. V. Schoenfeld, "Manufacturing metrology for c-Si photovoltaic module reliability and durability, Part I: Feedstock, crystallization and wafering," *Renew. Sust. Energ. Rev.*, vol. 59, pp. 84–106, 2016.

[65] F. Law, H. Hidayat, A. Kumar, P. Widenborg, J. Luther, and B. Hoex, "On the transient amorphous silicon structures during solid phase crystallization," *J. Non-Cryst. Solids.*, vol. 363, pp. 172–177, 2013.

[66] Nanophoton, "What is raman spectroscopy?." `https://www.nanophoton.net/raman/raman-spectroscopy.html`. [Online; accessed 25-August-2018].

[67] ION-TOF GmbH, "IONTOF TOF SIMS 5." `https://www.iontof.com/tof-sims-secondary-ion-mass-spectrometry.html`. [Online; accessed 1-November-2017].

[68] Y. Okamoto, N. Hirosaki, M. Ando, F. Munakata, and Y. Akimune, "Effect of sintering additive composition on the thermal conductivity of silicon nitride," *J. Mater. Res.*, vol. 13, no. 12, pp. 3473–3477, 1998.

[69] S. Huang, X. Ruan, J. Zou, X. Fu, and H. Yang, "Thermal conductivity measurement of submicrometer-scale silicon dioxide films by an extended micro-Raman method," *Microsyst. Technol.*, vol. 15, pp. 837–842, 2009.

[70] T. Maekawa, K. Kurosaki, T. Tanaka, and S. Yamanaka, "Thermal conductivity of titanium dioxide films grown by metal-organic chemical vapor deposition," *Surface and Coating Technology*, vol. 202, pp. 3067–3071, 2008.

[71] T. Olorunyolemi, A. Birnboim, Y. Carmel, O. W. Jr., and I. Lloyd, "Thermal conductivity of zinc oxide: from green to sintered state," *J. Am. Ceram. Soc.*, vol. 85, no. 5, pp. 1249–1253, 2004.

[72] M. Levinshtein, S. Rumyantsev, and M. Shur, *Handbook Series on Semiconductor Parameters*, vol. 1. Singapore: World Scientific, 1996.

[73] K. Çınar, M. Karaman, and A. Bek, "Improvement of laser-crystallized silicon film quality via intermediate dielectric layers on a glass substrate," *ACS Omega*, vol. 3, pp. 5846–5852, 2018.

[74] Laserline Optics Canada Inc., "Powell lens buyer's guide." `http://www.laserlineoptics.com/powell_primer.html`. [Online; accessed 29-July-2018].

CURRICULUM VITAE

PERSONAL INFORMATION

Surname, Name: ÇINAR, Kamil
Nationality: Turkish (TC)
Date and Place of Birth: September 24, 1985, Turkey
Phone: +90 553 2747425
email: cinarkamil@yahoo.com.tr
Military Service: Done, 19.12.2014.

Education

- Ph.D. Physics, Middle East Technical University (METU), Ankara TURKEY, September 05, 2018.
  Overall GPA: 3.50/4.0

- M.Sc. Physics, Middle East Technical University (METU), Ankara TURKEY, February 02, 2011.
  Overall GPA: 3.50/4.0

- B.Sc. Physics, Middle East Technical University (METU), Ankara TURKEY, January 24, 2009.
  Overall GPA: 3.13/4.0

- Kabataş Anatolian High School, Istanbul TURKEY, 1999-2003.

Employment

- Researcher at Nano-Optics Laboratory, Department of Physics at METU, 2015 - Currently.
- Coordinator of Optics Laboratory, Department of Physics at METU, 02/2017 - 09/2018.
- Teaching Assistant of Optics Laboratory, Department of Physics at METU, 02/2010 - 02/2017.
- Full-time Researcher, Department of Physics at METU about the Compact Pulse Terahertz Spectroscopy, 03/2009 - 11/2009.
- Part-time Student Assistant of Freshman Laboratory, Department of Physics at METU,
  Spring 2007/2008 - Fall 2008/2009.
- Part-time Technician, Nanomagnetics Ltd. Company, 02/2007 - 07/2007.

Honors, Awards & Fellowships

- Best Poster Award in PVCON2018, *International Conference on Photovoltaic Science and Technologies, July 4-6, 2018*, Ankara TURKEY.
- TÜBITAK (The Scientific and Technology Research Council of Turkey) Scholarship, 2009
- Honor Student at Middle East Technical University for several times.
- Third prize at semifinals of *Our Inventors Competition 2008*, organized by TV Channel, Kanal D in Turkey.
- Second prize at *The Redbull Gravity Challenge 2007, Ankara* in Turkey.
- Encouragement certificate at 1st *Young Inventors Congress 1999, Ankara* in Turkey.

Projects

Ongoing Studies

- Nanosecond Pulsed Infrared Laser Induced Crystallization of Amorphous Silicon Films.

Concluded Studies

- Detecting and Modulating Continuous Wave Terahertz (THz)-GHz Radiation by Plasma Detectors and Plasma Modulators (Experimental Project, 04/2012-01/2015).
- Characterizing Room Temperature Glow Discharge Lamps for Terahertz (THz) Detection Technologies (TÜBITAK 1001 Project, 03/2014 - 01/2015).
- Characterization of Glow Discharge Detectors with Terahertz Time Domain Spectroscopy (Experimental Project, 04/2012 - 01/2015).
- Pattern Formation in a Gas Discharge-Semiconductor System (Modeling and Computational Calculations, 07/2011 - 04/2012).
- Design and Construction of a Microwave Plasma Ion Source (Experimental Project,
  M.Sc. Thesis Project, 2011).
- Microwave Induced Plasma Chamber Design for Terahertz (THz) Spectroscopy (Experimental Project, 2009).
- Microwave Induction Plasma Systems and Langmuir Double Probe Diagnostics (Experimental Project, 2009).
- Tesla Coils (Experimental Project, Undergraduate Project for Understanding High Frequency and High Voltage Techniques, 2009).
- Jacob's Ladder (Experimental Project, for Understanding High Voltage Techniques, 2008).

- Electromagnetic Levitation System (Experimental Project, Electromagnetic Theory Course Project, 2007).
- Radiator Integrated Infrared Heater System (Experimental Project, Inventors Competition Project, 2006).

Publications

- "Effects of Pulse Overlap on Laser Induced Crystallization of Amorphous Silicon Thin Films," in preparation.
- "Effects of Film Thickness on Laser Induced Crystallization of Amorphous Silicon Thin Films," in preparation.
- "Ultra-Thin Heterojunction Solar Cells Fabricated on Laser Crystallized Amorphous Silicon Films," in preparation.
- K. Çınar, M. Karaman, and A. Bek, "Influence of Intermediate Layers on Laser Crystallization of a-Si Thin Films," *ACS Omega* 3 (5), pp 5846-5852, May 2018 (DOI: 10.1021/acsomega.8b00530).
- K. Çınar, H. Altan, and A. B. Şahin, "Characterization of a Glow Discharge Detector with Terahertz Time Domain Spectroscopy," *International Conference on Infrared, Millimeter and Terahertz Waves IRMMW-THz*, 2013.
- K. Çınar, H. Altan, and A. B. Şahin, "THz transmission and detection through glow discharge detectors," *Proceedings of SPIE: Terahertz Physics, Devices, and Systems VII: Advanced Applications in Industry and Defense*, Vol. 8716, 87160J, 2013.
- K. Çınar, H. M. Bozacı, and H. Altan, "Characterization of a Glow Discharge Detector with Terahertz Time Domain Spectroscopy," *IEEE Sensor Journal*, vol. 13, no. 7, pp. 2643-2647, July 2013.
- K. Çınar, Dr. E. Recepoğlu and Dr. A. Alaçakır, "Design and Production of Microwave Induced Plasma Ion Source for Ion Beam Optics," *Balkan Physics Letters*, 20, 201023, pp. 202-207, March 2012.

- K. Çınar, G. Karaoğlan, Z. Tosun, D. Akbar, H. Altan, "Characterization of Air-Nitrogen-Argon DC Glow Discharge Plasma with THz Time Domain Spectroscopy," *Proceedings-TERA-MIR, NATO Advanced Research Workshop Terahertz and Mid Infrared Radiation: Basic Research and Practical Applications*, November 2009.

- K. Çınar, " Elektromanyetik Alan Kavramı (Electromagnetic Field Concept)," *TÜBİTAK Bilim ve Teknik* (The leading popular science journal in Turkey), pages 80-81, July 2006.

Conference Presentations & Schools

- "Laser Crystallization of Si Thin Film via Pulsed IP Laser for Ultra-Thin Crystalline Solar Cells," *Poster at PVCON2018, International Conference on Photovoltaic Science and Technologies, July 4-6, 2018* , Ankara TURKEY.

- "Pulsed IR Laser Crystallized Amorphous Silicon Thin Films for Photovoltaics," *Poster at DAAD, Powering Energy Transition: The Role of Renewable Energy and Energy Efficiency,* 7th- 8th *September 2017*, Ankara TURKEY.

- "Laser Crystallization of Amorphous Silicon Thin Films," *Talk at GUNAM Workshop,* 25th *March 2017*, Ankara TURKEY.

- "Silicon Processing with 1550nm Femtosecond Pulsed Laser," *Poster at GUNAM Workshop,* 25th *March 2017*, Ankara TURKEY.

- "Quality Enhancement of Laser Crystallized Amorphous Silicon Thin Films," *Poster at GUNAM Workshop,* 25th *March 2017*, Ankara TURKEY.

- " Enhancement of Crystal Quality of Laser Crystallized Amorphous Silicon Thin Films (Lazerle Kristallendirilmiş Amorf Silisyum İnce Filmlerin Kristal Kalitelerinin Artırılması," *Poster at* 22th *Condensed Matter Physics Ankara Colloquium (22. Yoğun Madde Fiziği Ankara Toplantısı),* 16th *December 2016*, Ankara TURKEY.

- "Characterization of a Glow Discharge Detector with Terahertz Time Domain Spectroscopy," *Talk at The* 38th *International Conference on Infrared, Millimeter and Terahertz Waves IRMMW-THz 2013*, Mainz GERMANY.

- "Characterization of Short DC Discharge Plasmas with Terahertz Time Domain Spectroscopy," *Poster at* 14th *National Optics, Electro - Optics and Photonics Workshop 2012*, Istanbul TURKEY.

- 5th ITER International Summer School, MHD and Energetic Particles 2011, Aix en Provence FRANCE.

- "Design and Production of Microwave Induced Plasma Ion Source for Ion Beam Optics," *Talk at* 4th *National Congress on Particle Accelerators and Applications 2010*, Bodrum TURKEY.

Technical Knowledge & Scientific Softwares

- Laser Equipments and Optical Tools, Pulsed Laser Marking Systems, Raman Spectroscopy Systems, Scanning Electron Microscope (SEM) Operator, Arduino Applications, Microwave and RF Systems, Frequency Analyzer Systems, Vacuum Systems, Impedance Analyzer Systems.

- SolidWorks, Arduino Coding, Origin, Labview, COMSOL Multiphysics, Mathlab, Octave, Office Applications, Operating Systems: Unix/Linux, MS Windows.

Language Knowledge

- English (Advanced), Turkish (Native Speaker), German (Beginner)

Personal Interests & Social Activities

- Ultrafast Laser Applications

- Designing and Building Pulsed Lasers and Laser Diode Drivers

- Plasma Technologies
- Terahertz-Submillimeter-Millimeter Wave Science and Technology
- Economy & Investment
- An active member of The Physics Society of METU, 2003 - 2008.